New Feeding Networks and Planar Antenna Designs for Leaky-wave Systems and Communication Applications

Victoria Gómez-Guillamón Buendía

Submitted for the degree of Doctor of Philosophy

School of Engineering & Physical Sciences

Heriot-Watt University

Edinburgh, United Kingdom

April 2019

Abstract

The fast development in modern communication systems such as radars, medical imaging, sensors or satellites demands efficient and compact antenna designs that can satisfy the high data throughput and beam scanning requirements. This is commonly achieved by different means including electromechanical or mechanical steering, which sometimes are not the best option as additional cost, size or losses may be introduced. However, low-cost and compact structures can be obtained by using planar leaky-wave antennas, whose inherent high directivity and electrical beam steering capabilities have been realised to be a solution for the issues encountered by these systems.

Nevertheless, there are several limitations that these antennas still need to overcome. One clear example is the lack of efficient and simple feeding networks for certain types of leaky-wave antennas that can reduce their performance and compactness. In turn, there are modern indoor applications, such as WiFi or radio frequency identification (RFID), where selective distributed communications are required but current leaky-wave antennas cannot efficiently provide or their use implies cost and weight constraints.

In this thesis, planar configurations are presented to provide efficient and low profile solutions for leaky-wave antennas using concepts such as partial reflective surfaces or simple technologies as parallel-plate waveguides. It is also demonstrated that novel systems for two-dimensional (2D) or wideband beam scanning can also be obtained by the use of simple feeders including vertical electric dipoles. In addition, a broad-beam alternative to a non-selective and expensive beam scanning performance inside airplanes for RFID systems is introduced easing weight restrictions. These configurations represent an advancement for the state-of-the-art and are interesting alternatives to their non-planar counterparts. To support these designs, theoretical analysis, full-wave simulations and measurements are provided.

Dedication

A mis Montañas, compañeras de vida y noches en vela.

To my Mountains, my partners in life and companions through my sleepless nights.

Acknowledgements

Infinite thanks to my supervisor Dr. Symon K. Podilchak for always believing in me and supporting me during this adventure. His knowledge, patience and positive attitude always was refreshing. I would also like to specially thank Dr. José Luis Gómez Tornero for his trust and help that brought me here and Prof. George Goussetis for his support and help during the work presented in this thesis.

Fortunately, I also had the pleasure to work with some of the best leaky-wave antenna experts from La Sapienza University of Roma, Italy. Dr. Paolo Bacarelli and Dr. Paolo Burghinoli from who I acquired invaluable knowledge that helped me develop this thesis, and Dr. Davide Comite who worked with me for hours until we got things successfully working. He also helped me anytime I needed it while also increased my "polite" Italian word database, and more importantly, made me feel at home in a foreign country. Hopefully, our future paths will keep us connected for more leaky-wave adventures.

I need to express countless gratitude to the guys from the electrical workshop, Gordon, Barry and Gary, that made real all my tricky designs with patience and a big smile. Special consideration goes to Andy, who saved many antennas from disaster and always tried his best to do the impossible (except going for real to Ghana). In addition, many of these structures were extremely complicated to manufacture given the small tolerances, therefore I deeply thank Nick Howland from Printech Ltd that always helped as much as he could, providing the best results. Without those prototypes this thesis could not have been finished.

However, this would have never been possible without the support and help from all my dear colleagues who made this process easier and became my second family, Rahil Joshi, Alexios Coustoris, Salvador Mercader, Adrián Ayastuy, Rafael Adorna, Cristian Alistarh, María Jesús Cañavate, Pascual Hilario, Miguel Poveda and Khaled

Research Thesis Submission

Please note this form should be bound into the submitted thesis.

Name:	Victoria Gómez-Guillamón Buendía		
School:	EPS/ISSS		
Version: *(i.e. First, Resubmission, Final)*	Final	Degree Sought:	PhD Electrical Engineering

Declaration

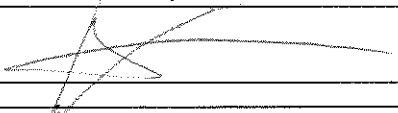In accordance with the appropriate regulations I hereby submit my thesis and I declare that:

1. The thesis embodies the results of my own work and has been composed by myself
2. Where appropriate, I have made acknowledgement of the work of others
3. The thesis is the correct version for submission and is the same version as any electronic versions submitted*.
4. My thesis for the award referred to, deposited in the Heriot-Watt University Library, should be made available for loan or photocopying and be available via the Institutional Repository, subject to such conditions as the Librarian may require
5. I understand that as a student of the University I am required to abide by the Regulations of the University and to conform to its discipline.
6. I confirm that the thesis has been verified against plagiarism via an approved plagiarism detection application e.g. Turnitin.
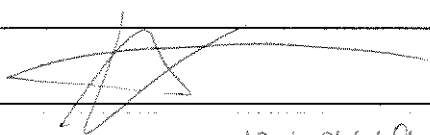
ONLY for submissions including published works

Please note you are only required to complete the Inclusion of Published Works Form (page 2) if your thesis contains published works)

7. Where the thesis contains published outputs under Regulation 6 (9.1.2) or Regulation 43 (9) these are accompanied by a critical review which accurately describes my contribution to the research and, for multi-author outputs, a signed declaration indicating the contribution of each author (complete)
8. Inclusion of published outputs under Regulation 6 (9.1.2) or Regulation 43 (9) shall not constitute plagiarism.

*   *Please note that it is the responsibility of the candidate to ensure that the correct version of the thesis is submitted.*

Signature of Candidate:		Date:	11/09/2019

Submission

Submitted By *(name in capitals)*:	VICTORIA GOMEZ-GUILLAMON BUENDIA
Signature of Individual Submitting:	
Date Submitted:	13/09/19

For Completion in the Student Service Centre (SSC)
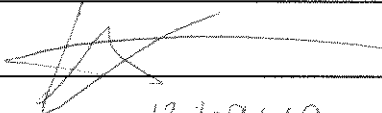
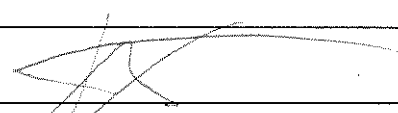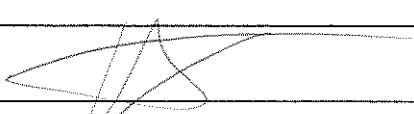| Limited Access	Requested	Yes	No	Approved	Yes	No
E-thesis Submitted *(mandatory for final theses)*						
Received in the SSC by *(name in capitals)*:				Date:		

Inclusion of Published Works

Please note you are only required to complete the Inclusion of Published Works Form if your thesis contains published works under Regulation 6 (9.1.2)

Declaration

This thesis contains one or more multi-author published works. In accordance with Regulation 6 (9.1.2) I hereby declare that the contributions of each author to these publications is as follows:

Citation details	V. Gomez-Guillamon Buendia and S. K. Podilchak and G. Goussetis and D. Masotti and A. Costanzo and P. Nicole, \A Smart Cable, "Offering Selective and Distributed Antenna Radiation Using RF Switches and Non-Conventional Hybrid Couplers," IEEE Transactions on Antennas and Propagation, vol. 66, no. 11, pp. 6346-6351, Nov 2018.
Author 1	Design work (theory and simulations), manufacturing and measurements, post-processing, writing the article.
Author 2	Assitance and guidance through the whole work
Signature:	
Date:	13/09/19

Citation details	V. Gomez-Guillamon Buendia and S. K. Podilchak and D. Comite and P. Baccarelli and P. Burghignoli and J. L. Gomez Tornero and G. Goussetis, "Compact Leaky SIW Feeder Offering TEM Parallel PlateWaveguide Launching," IEEE Access, vol. 66, no. 11, pp. 6346-6351, Feb 2019.
Author 1	Design work (theory and simulations), manufacturing and measurements, post-processing, writing the article.
Author 2	Assitance and guidance through the whole work
Signature:	
Date:	13/09/19

Citation details	D. Comite and V. Gomez-Guillamon Buendia and S. K. Podilchak and D. D. Ruscio and P. Baccarelli and P. Burghignoli and A. Galli, \Planar Antenna Design for Omnidirectional Conical Radiation Through Cylindrical Leaky Waves," IEEE Antennas and Wireless Propagation Letters, vol. 17, no. 10, pp. 1837-1841, Oct 2018.
Author 1	Theoretical and simulation analysis, writing the article
Author 2	Manufacturing and measurements, post-processing, assistance writing the article.
Signature:	
Date:	13/09/19

Contents

List of Figures

xiii

List of Tables

Glossary

1D   One-dimensional

2D   Two-dimensional

AWG   American wire gauge

CP   Circular polarization

LP   Linear polarization

MoM   Method of moments

PCB   Printed circuit board

PEC   Perfect electric conductor

RF   Radio frequency

RFID   Radio frequency identification

SIIG   Substrate integrated image guide

SIW   Substrate integrated waveguide

SMA   SubMiniature version A

TE   Transverse electric

TEM   Transverse electromagnetic

TM   Transverse magnetic

TNC   Threaded Neill Concelman

UHF   Ultra high frequency

VHF   Very high frequency

List of Symbols

ω Angular frequency

α Attenuation constant or leakage rate

$\wp$ Cauchy's principal value

γ Complex propagation constant

μ_0 Permeability in free-space

μ_r Permeability in the dielectric

ε_0 Permittivity in free-space

ε_r Permittivity in the dielectric

β Phase constant

c Speed of light

λ_g Guided wavelength

λ_0 Wavelength in free-space

k_0 Wavenumber in free-space

List of publications

Journal papers

1. M. Kuznetcov and **V. Gómez-Guillamón Buendía** and Z. Shafiq and L. Matekovits and D. E. Anagnostou and S. K. Podilchak, "Printed Leaky-Wave Antenna with Aperture Control using Width-Modulated Microstrip Lines and TM Surface-Wave Feeding by SIW Technology," *IEEE Antennas and Wireless Propagation Letters.*

2. **V. Gómez-Guillamón Buendía** and S. K. Podilchak and D. Comite and P. Baccarelli and P. Burghignoli and J. L. Gómez Tornero and G. Goussetis, "Compact Leaky SIW Feeder Offering TEM Parallel Plate Waveguide Launching," *IEEE Access*, vol. 66, no. 11, pp. 6346-6351, Feb 2019.

3. **V. Gómez-Guillamón Buendía** and S. K. Podilchak and G. Goussetis and D. Masotti and A. Costanzo and P. Nicole, "A Smart Cable Offering Selective and Distributed Antenna Radiation Using RF Switches and Non-Conventional Hybrid Couplers," *IEEE Transactions on Antennas and Propagation*, vol. 66, no. 11, pp. 6346-6351, Nov 2018.

4. D. Comite and **V. Gómez-Guillamón Buendía** and S. K. Podilchak and D. D. Ruscio and P. Baccarelli and P. Burghignoli and A. Galli, "Planar Antenna Design for Omnidirectional Conical Radiation Through Cylindrical Leaky Waves," *IEEE Antennas and Wireless Propagation Letters*, vol. 17, no. 10, pp. 1837-1841, Oct 2018.

5. D. Comite and W. Fuscaldo and S. K. Podilchak and **V. Gómez-Guillamón Buendía** and P. D. Hilario Re and P. Baccarelli and P. Burghignoli and A. Galli, "Microwave Generation of X-waves by Means of a Planar Leaky-Wave Antenna," *Applied Physics Letters*, vol. 113, no. 14, pp. 144102, Oct 2018.

6. D. Comite and W. Fuscaldo and S. K. Podilchak and P. D. Hilario Re and **V. Gómez-Guillamón Buendía** and P. Burghignoli and P. Baccarelli and A. Galli, "Radially Periodic Leaky-Wave Antenna for Bessel Beam Generation Over a Wide-Frequency Range," *IEEE Transactions on Antennas and Propagation*, vol. 66, no. 6, pp. 2828-2843, June 2018.

Journal papers to be submitted

1. **V. Gómez-Guillamón Buendía** and S. Podilchak "Wideband Planar Transition from Parallel-Plate Waveguide to Substrate Integrate Image Guide for Microwave Frequencies," *IEEE Microwave Theory and Techniques.*

Conferences

1. Z. Shafiq and M. Kuznetcov and **V. Gómez-Guillamón Buendía** and D. Anagnostou and S. K. Podilchak, "A Planar Horn Antenna for TM Surface Wave Launching Using Substrate Integrated Waveguide Technology," *2019 13th European Conference on Antennas and Propagation (EuCAP)*, pp. 1-3, Krakow, Poland, April 2019.

2. D. Comite and **V. Gómez-Guillamón Buendía** and W. Fuscaldo and Z. Shafiq and S. K. Podilchak and P. Burghignoli and P. Baccarelli and A. Galli, "Design of a Dual-Mode Operation 2D Periodic Planar Leaky-Wave Antenna," *2019 13th European Conference on Antennas and Propagation (EuCAP)*, pp. 1-4, Krakow, Poland, April 2019.

3. D. Comite and **V. Gómez-Guillamón Buendía** and P. Burghignoli and P. Baccarelli and S. K. Podilchak and A. Galli, "Array-Fed Fabry-Perot Cavity Antenna for Two-Dimensional Beam Steering," *2018 IEEE International Symposium on Antennas and Propagation USNC/URSI National Radio Science Meeting*, pp. 1873-1874, Boston, USA, July 2018.

4. **V. Gómez-Guillamón Buendía** and S. K. Podilchak, "Simple Surface-wave Launching by Parallel-plate and Microstrip Feeding for Leaky-wave Antennas and Other Planar Guided-wave Applications," *12th European Conference on Antennas and Propagation (EuCAP 2018)*, pp. 1-4, London, UK, April 2018.

5. **V. Gómez-Guillamón Buendía** and S. K. Podilchak and G. Goussetis and J. L. Gómez Tornero, "A TM_0 Surface-wave Launcher by Microstrip and Substrate Integrated Waveguide Technology," *2017 11th European Conference on Antennas and Propagation (EUCAP)*, pp. 3859-3862, Paris, France, March 2017.

6. **V. Gómez-Guillamón Buendía** and S. Kenny and S. K. Podilchak and G. Goussetis and A. Costanzo and P. Nicole, "Smart Cable for Radio Frequency Identification in Aeronautical Applications," *2016 10th European Conference on Antennas and Propagation (EuCAP)*, pp. 1-3, Davos, Switzerland, April 2016.

Chapter 1

Introduction

1.1 Motivation

Many modern communication systems benefit from the use of steerable radiated beams for tracking, selective transmission or detection purposes. One illustrative example is an airborne radar [1,2], which scans a region with a high directive beam for target detection. This beam scanning can be done mechanically, electrically or both, if the beam needs to be steered in the elevation and azimuth planes. While mechanical scanning can be a simpler implementation, as it normally consists of an external motor that moves the antenna along the azimuth or elevation planes, it can also be slower, bulkier and with a higher maintenance cost [1]. Therefore, given the trend to compact and low-cost systems needed for new devices and technologies, electrical steering has been preferred. This is also due to its fast and flexible scanning despite of its relative complexity and limitations when moving towards end-fire, where a gradual loss of directivity is observed because of the smaller effective area of the antenna aperture [2].

There are several means to obtain electrical beam scanning. These options can include switching between a set of feeders, varying the phase of the different elements in an array, or using leaky-wave antennas [1,2]. The latter has inherent beam steering capabilities with a variation in frequency. This is because their phase constant, that is frequency dependent and defines the beam pointing angle [3]. This feature presents a clear advantage with respect to other electrical scanning options as there are no external devices involved in the antenna operation, e.g., phase shifters or switches,

which can increase design complexity, size and cost [3]. Thus, planar leaky-wave antennas can be an interesting alternative to bulky or complicated beam steering devices given their low-cost and low-profile while keeping efficient and directive scanning.

However, planar leaky-wave antennas are not a panacea and sometimes require complex feeding networks that can arise some challenges in terms of implementation or integrability. See for example [4–7], where leaky-waves antennas placed on parallel-plate waveguides, i.e., two conductors in parallel separated by air or dielectric material, are fed by bulky coupling waveguides, intricate coupling windows made of metallised vias inside the substrate or large integrated parabolic reflectors.

In addition, there are indoor or underground communication scenarios where selective distributed radio frequency (RF) systems are required and leaky-wave or distributed antenna systems are traditionally used. However, they do not offer any adaptive and simple switching mechanism to selectively distribute RF power within the coverage area. Furthermore, in the case of leaky-wave antennas, these may no longer be suitable for modern applications as WiFi or radio frequency identification (RFID), due to the large increment of losses with higher frequencies [8] or the extra weight provided in critical cases such as inside airplanes [9].

Given these limitations, the objective of this research is to provide efficient and compact structures that present an advancement on the current state-of-the-art that can mitigate the drawbacks of using this type of electrical beam steering systems. Several feeding networks will be proposed based on the excitation of surface-waves, leaky-waves or using simple vertical electric dipoles. Moreover, in the case of the vertical electric dipoles, interesting features including two-dimensional (2D) scanning or wideband performance could be achieved. On the other hand, it will also be studied a planar broad-beam distributed antenna with selective distributed transmission that could replace the beam scanning from a non-planar leaky-wave antenna inside airplanes for RFID or WiFi applications, reducing cost, losses and weight constraints.

1.2 Methodology of Research

To accomplish these objectives, a literature review is carried out to assess the challenges that leaky-wave antennas are facing nowadays. The focus is established on technologies that are more sensitive to these limitations given their physical characteristics. These technologies include dielectric image guides, i.e., dielectric slabs with an extended ground plane, parallel-plate waveguides, leaky slotted coaxial cables and Fabry-Perot cavities, which consist of a cavity formed between a partially reflective surface and a perfect electric conductor wall.

Once the issues to overcome are clear, the design process is started and can be summarised in the following steps:

- Theoretical analysis. These analysis are performed to confirm feasibility and provide the starting point necessary to optimally design the different systems. Transverse resonance networks, mode propagation, dispersive analysis, Bloch analysis, radiated field calculations and impedance matching are among the theoretical approaches explored. The tools employed for such studies are Matlab [10] and Mathematica [11].

- Full-wave simulations. Electromagnetic solver CST [12] has been utilised. This software has been chosen as it is based on different algorithms to compute Maxwell's equations providing an approximation of the expected performance for the designed structure. In particular, the simulations carried out in this thesis have been performed using the frequency domain solver, based on the finite element method. This method divides the structure in small triangles to find simple equations to then assemble them into a larger system of equations that models the whole structure. Results obtained from these simulations are used to validate theoretical concepts and optimise the design parameters. Parametric simulations have been used to optimise the designs, while field monitors have been set to acquire 2D field propagation and far-field radiation.

- Manufacturing and measurements. The different configurations presented in this thesis have been manufactured using printed circuit boards (PCBs) etched in-house by the Electrical and Mechanical Workshop at Heriot-Watt University. When not possible, industrial manufacturers have been selected. Measurements have been carried out in the Microwave Lab at Heriot-Watt Uni-

versity utilising the equipment available, which comprises: calibrated anechoic chamber, NSI near-field system, Diamond far-field acquisitioner software and 2-ports and 4-ports vector network analysers.

- Post-processing. Measured results are then compared to theory and simulations to corroborate the concept. The tool used has been Matlab [10].

In turn, part of this research has been carried out in collaboration with researchers from La Sapienza University of Rome, under a Erasmus+ frame. In particular, the work related to 2D leaky-wave antennas were performed by a joint effort between both research teams to provide competitive alternatives to improve the state-of-the-art for advanced radar systems, medical imaging or wireless communication and power transfer applications. Same methodology has been followed as for the rest of the thesis.

1.3 Document Overview

This thesis presents configurations that can mitigate feeding and selective distributed transmission issues that leaky-wave systems encounter nowadays. The focus is on feeding networks and selective distributed indoor communications. Three feeders based on surface-wave, leaky-wave and vertical electric dipole concepts are introduced. Moreover, it also proposes an alternative consisting of broad-beam distributed antennas to allow for selective transmission and ease weight constraints on airplanes where leaky-wave antennas fail to be an efficient and low-profile solution at microwave frequencies. These configurations are explained in individual chapters, with a total of seven chapters including the Introduction. The thesis is organised as follows.

Chapter 2 presents the literature review for leaky-wave systems and their different drawbacks, covering also the available solutions on the literature with their benefits and disadvantages. This will include feeding networks for dielectric image guides, parallel-plate waveguides and 2D leaky-wave antennas, together with leaky feeder systems inside tunnels and airplanes. Background theory on leaky-waves and surface-waves as well as leaky feeder systems will then be explained in order to set the fundamentals for the concepts presented in the following chapters of the thesis.

Chapter 3 deals with the challenges of exciting leaky-wave antennas on dielectric image guides, which lack of low-cost and fully integrated feeders. A feeding network based on a surface-wave launcher consisting of simple microstrip and parallel-plate waveguide technologies will be proposed. Theoretical analysis focused on the conventional guided-wave theory needed for surface-wave excitation by the truncation of a parallel-plate waveguide on a grounded dielectric slab will be presented. Following the explained conditions and by the addition of a sub-wavelength array of square patches as a matching section, an efficient and fully planar surface-wave launcher will be designed. As proof of concept, this launcher will be simulated to excite a leaky-wave antenna on a rectangular grounded dielectric slab. Subsequently, it will then be applied to dielectric image guides and substrate integrated image guides (SIIG), which consist of air holes drilled on the sides of the guide confining the propagating fields, to improve the actual state-of-the-art. Challenges faced during the manufacturing process of the SIIG structure, the actions taken and measured results will be provided.

Chapter 4 introduces the application of leaky-wave concepts to create a feeding network capable of creating uniform phase and amplitude wavefronts, which is a limitation encountered when feeding array antennas placed on top of parallel-plate waveguides. Therefore, a novel launcher will be presented to excite the fundamental parallel-plate waveguide mode by means of a leaky T-junction implemented on substrate integrated waveguide (SIW) technology. This technology consists of a dielectric substrate with conductor layers at top and bottom with two separated rows of metallised vias along the direction of wave propagation to emulate the side walls of a metallic waveguide. A transverse resonance equation and a Bloch analysis will be developed to accurately analyse the mode propagation and set the parameters needed for the launcher. Full-wave simulation results will be shown to assess and confirm the expected performance. Manufacturing and measurements will be reported and comparison to the expected results will be discussed. Moreover, it will also be explained that by the addition of the matching network used in the previous chapter, this structure could be implemented as a surface-wave launcher itself, as well as an end-fire antenna as additional applications.

Chapter 5 explores the use of vertical electric dipoles in individual and array configurations to excite 2D periodic leaky-wave antennas, focusing on a bull's-eye prototype

and a Fabry-Perot cavity to improve the bandwidth. This chapter is a result of a collaboration between research teams at Heriot-Watt University and La Sapienza University. The dispersive analysis and impedance matching techniques for antenna design will be reported. Simulations, practical experiments and manufacturing process developed by the author will be reported in detail throughout the chapter. Different features that are possible in the near-field as well as the far-field for the bull's-eye antenna with this feeding setup will be discussed. Moreover, 2D beam scanning capabilities studied for the Fabry-Perot cavity will be explained. This chapter will end with a comparison between the two proposed antennas and their applications.

In Chapter 6 the focus is on the design of an alternative antenna configuration that could substitute leaky coaxial cables employed for RFID or WiFi applications inside airplanes, where weight constraints are in place and selective distribution of RF power within the coverage area is needed to achieve higher transmission power levels. It will be shown how by the use of broad-beam distributed antennas the same coverage as beam scanning transmission by leaky feeders could be achieved. Moreover, by the addition of a control unit, these antennas could be turned "ON" and "OFF" as required to achieve higher transmission levels avoiding unnecessary radiation. Theoretical approaches for impedance matching and power distribution will be discussed. Detailed explanations on the design process will be given, while simulations and measurements will be shown to support the concepts. Moreover, a link budget analysis will be performed for two test case scenarios were the worst situations in terms of power propagation will be examined and a comparison with a commercial leaky coaxial cable will be reported.

Finally, in Chapter 7 the conclusions of the work presented in this thesis will be summarised including a list of contributions, as well as the possible future work that arises from it, such as new directional routing circuits, transmission line bends and transition sections exploiting surface-waves, as well as other new planar leaky-wave antennas driven using cylindrical leaky-wave concepts or conventional theory among others.

Chapter 2

Leaky-wave Systems

2.1 Introduction

Leaky-wave antennas use discontinuities, e.g., slots or metallic strips, to perturb a travelling-wave along a guiding structure as a radiating mechanism [3]. These antennas date back from 1940 when a waveguide with a continuous slot in one of the side walls was patented [13]. Radiation was achieved by means of leaked energy from the travelling-wave inside the waveguide into free-space by a continuous slot. This one-dimensional (1D) configuration falls into the uniform leaky-wave antenna classification [3] as the perturbation element introduced does not change its geometry along the structure. Nevertheless, there is no control on the amount of leaked energy, which consequently produces broad-beam patterns [13]. Therefore, a modified version was proposed a decade later in [14], where the long slot was substituted by holes closely spaced along the waveguide side wall. Given the proximity of the holes, this structure is considered quasi-uniform as the radiating mode is the fundamental mode, which is still a fast-wave, i.e., its phase velocity is greater than the speed of light. Thanks to this configuration, 1D leaky-wave antennas with directive narrow-beams were finally possible to achieve in practice [3, 14]. Diagrams of the structures described are depicted in Fig. 2.1.

Following the development of these structures with discontinuities, a periodic printed leaky-wave antenna was proposed in [18]. This structure was based on a coplanar transmission line periodically modulated using triangular, sinusoidal and trapezoidal shapes. The main difference with quasi-uniform structures is that periodic leaky-

wave antennas are based on the radiation of a modulated travelling slow-wave, i.e., its phase velocity is less than the speed of light, supported in the guiding structure [3]. This slow-wave can be decomposed into an infinite number of spatial harmonics or Floquet's modes [19–21] of which, typically, only the fast $n = -1$ harmonic will be excited by the design, being the main contributor to the radiation.

At the same time as their 1D counterpart, two-dimensional (2D) leaky-wave antennas, which are planar by nature, were also proposed in [22]. Highly directive pencil beams with gain values between 15.00 and 20.00 dBi were achieved by means of a planar cavity with a partially reflective screen or surface on top of the antenna aperture. This partially reflective surface can consist either of a stack of substrates [16, 23] or a periodic array of slots or metallic gratings [17, 24–26] (see Fig. 2.1). The main feature of these 2D systems is that these antennas can produce a pencil beam at broadside or an omnidirectional conical beam depending on the design and type of feeding [3] as it will be explained in Section 2.3.2.
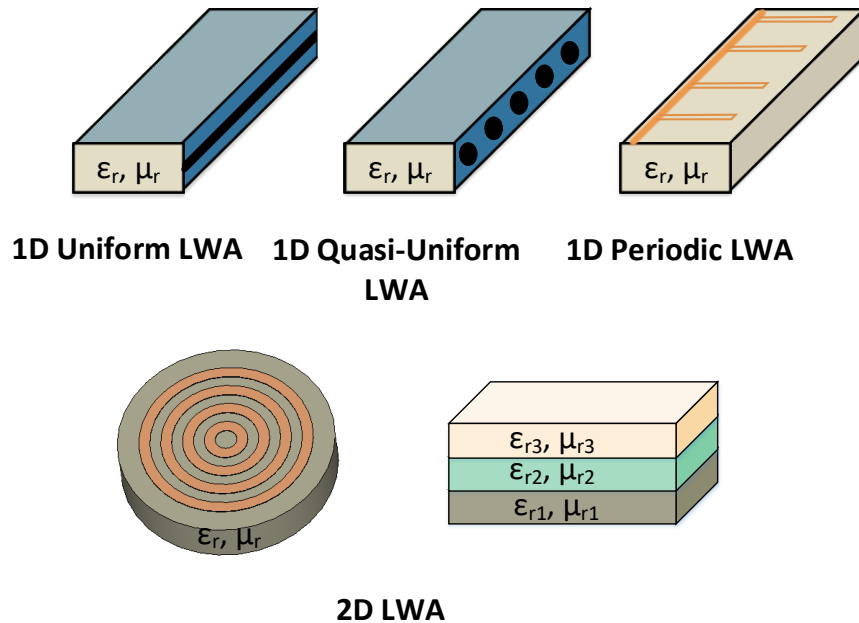
Figure 2.1: Diagrams of the examples of the different types of leaky-wave antennas. On top, 1D leaky-wave antennas are depicted; starting from the waveguide with a continuous slot on the sidewall [13] on top left, followed by the quasi-uniform leaky-wave antenna with close-spaced holes [14] and the periodic leaky-wave antenna, which in this example, is based on a microstrip line loaded periodically with stubs [15]. On the bottom, two-dimensional (2D) leaky-wave antennas examples consisting of partially reflective surface cavities are illustrated; on the bottom left, periodic metallic gratings and on the right, a stack of substrates [16, 17].

In parallel to these advancements, during the 70s leaky-waves antennas were demonstrated to be very useful for beam scanning and radio frequency (RF) communications in scenarios where power transmission was challenging to be provided by other types of antennas, e.g., corridors, mines or subways [27]. Several studies involving experimental testing with leaky feeder antennas, that are slotted coaxial cables, were developed inside these underground conditions to assess the feasibility of these systems [28]. It was then stated that these leaky-wave antennas were the best solution for communications in the very high frequency (VHF) and lower ultra high frequency (UHF) bands given the cable limitations at higher frequencies in terms of losses while also considering the spatial constraints which additionally influenced the radiation, e.g., tunnel dimensions that could prevent the propagation [27–29]. These systems have been commonly implemented over the years taking advantage of their beam scanning features in different environments and for higher frequencies than initially planned, such as inside high speed trains [30–32], RF communications inside airplanes and building corridors [33–35] or as buried sensors for intruder detection [36–38].

2.2 State-of-the-art Review

Modern communications systems such as radar, tracking, wireless power transfer or sensors are moving towards higher frequency ranges, requiring the use of planar antennas with low-profile and high efficiency beam scanning features. 1D and 2D planar leaky-wave antennas can be a good candidate to satisfy these needs. The use of 2D periodic structures for instance allows to achieve conical beam scanning, which is a planar and high directive option [3, 39]. The propagation of radial leaky-waves produces an omnidirectional conical beam that can be steered in frequency and achieve high gain values ($> 20.00\,\text{dB}$). Several examples can be found in the literature that are commonly implemented by single or multilayer structures with a partially reflective surface on top [40–46]. For example in [42], the use of horizontal magnetic dipoles as feeders to excite the fundamental transverse magnetic (TM_0) surface-wave mode instead of the typical transverse electric (TE_1) is studied for bandwidth enhancement. In this work, it is demonstrated that by using these launchers, broadside and uniform conical beam radiation can be achieved keeping a planar profile. In [44], this idea is implemented on a "bull's-eye" antenna made of

concentric annular strip gratings on top of a grounded dielectric slab that achieves conical radiation due to horizontal magnetic dipoles etched on the ground plane. When using the surface-wave launchers, the excited slow-wave is perturbed by the annular rings to allow its fast spatial harmonic $n = -1$ to be radiated increasing the bandwidth to a 35.00%. Alternatively, in [47], a Fabry-Perot cavity fed by horizontal electric dipoles etched on the ground plane is implemented on a multifunctional radar for vehicle detection, achieving 20.00 dBi of gain at 60.00 GHz.

1D leaky-wave antennas have also been implemented in a variety of technologies for microwave and millimetre waves. For instance, many communication systems are based on dielectric image guides as they provide low losses at higher frequencies. In [48] for instance, distributed dielectric image guide leaky-wave antennas are installed on a collaborative robot for industrial processes. These antennas are acting as sensors at 160.00 GHz to detect humans within their vicinity in order to protect workers from injuries due to accidental collisions with the robot. The first leaky-wave antenna using dielectric image guides involved the use of a corrugated structure [49], being the top of the dielectric image guide modified with grooves (see Fig. 2.2), showing high performance and setting the base for future high frequency leaky-wave antennas. On the other hand, the use of periodic strip gratings instead of altered dielectric slabs is common due to the simple manufacturing provided by microstrip technology, as reported in [50,51]. However, this grating is only desirable for lower frequency ranges of the millimetre-wave band given the high conductor losses experienced at these frequencies.

In turn, there is a variety of different features and improvements that can be achieved using this technology, either involving metallic gratings or by modifying the guiding structure. For example in [52], a leaky-wave antenna was implemented in a nonradiative dielectric image guide with a printed strip circuit on top to efficiently and originally taper the aperture illumination allowing also sidelobe reduction. Just by modifying the printed strip shape and its position, the leakage constant α can be modulated to increase antenna efficiency as required. In addition, gain performance can be highly improved by just adding another dielectric layer with a staircase shape as in [53], where the gain bandwidth is improved by four times.

On the other hand, dielectric image guides are not the only 1D option available due to the introduction of substrate integrated waveguide (SIW) technology (see
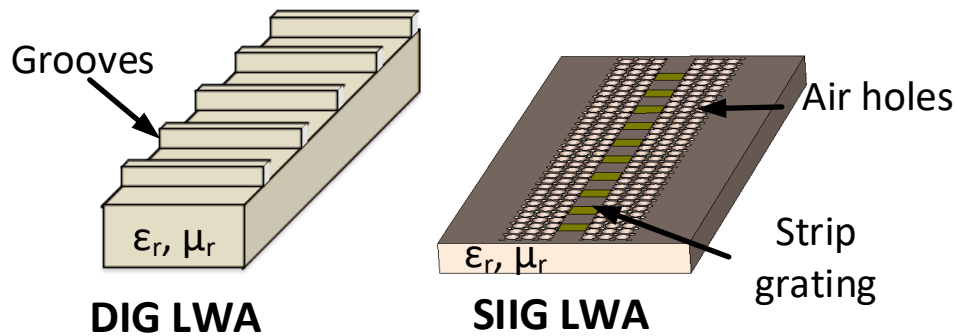
Figure 2.2: Diagrams of dielectric image guide and substrate integrated image guide (SIIG) leaky-wave antennas.

Fig. 2.3). Many leaky-wave antennas implemented using waveguides or other non-planar structures have been re-designed to realise a planar form using this technology. Its competitive characteristics in terms of power handling and low-losses at these frequencies can offer significant advantages when compared to its non-planar counterparts [54], while also allowing for simple feeding using microstrip and other planar designs [55]. A straightforward way to create leaky-wave radiation in these kind of structures is to use a partially reflective surface in one of the sides of the SIW guide while the other acts as a perfect electric conductor (PEC) wall, as explained in [56] (see Fig. 2.3). In particular, the dominant mode for SIW is a fast-wave which can become leaky by introducing the partially reflective surface.

In addition, recent studies demonstrate that it is possible to independently control the leakage rate and the phase constant enabling pointing and beamwidth customization as desired [57, 58]. Other advancements include the suppresion of the open stopband problem. This region, present in most periodic leaky-wave antennas [59], features high reflections back to the source and poor radiation when the beam is scanning at broadside. This is because the travelling-wave becomes a standing-wave with a leakage rate α dropping to zero [3, 59, 60]. This is due to one of the fast spatial harmonics being radiating. At this point, all the reflections from the different periodic discontinuities are added in phase back to the source [3]. This effect can be easily prevented with a reduction of the SIW width in a small section of the bounding channel, as explained in [61], where full scanning, including at broadside, is reported. Besides, another limitation of leaky-wave antennas that can be overcome using SIW is reported in [62], where scanning in the end-fire direction can be achieved by using a slotted SIW. This can be done since the fields present at the
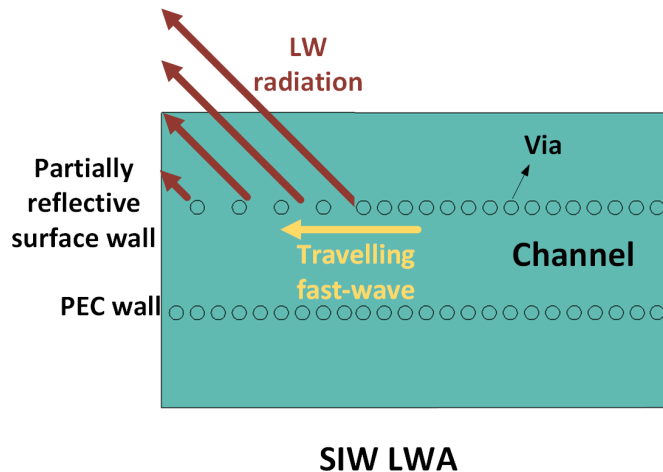
Figure 2.3: Diagram of an SIW leaky-wave antenna and its radiation principle.

slots are equivalent to magnetic currents in the longitudinal direction.

As a combination of these two technologies for millimetre-waves, in [63] researchers proposed the use of substrate integrated image guides (SIIGs), which consist of air holes drilled instead of plated vias on the sides of the guide to confine the propagating fields. As depicted in Fig. 2.2 and explained further in [64], the use of this technology combined with metallic strips for leaky-wave antenna excitation can obtain up to 84.00% radiation efficiency for a 50.00% smaller structure when compared to dielectric image guide antennas. Yet, this structure involves a more complex manufacturing process including the attachment of waveguide transitions. Nevertheless, it simplifies the feed matching given the bounded characteristics. Despite its modest complexity, SIIG is a novel technology that is in full development nowadays and several leaky-wave antenna systems have already been developed. Designs with an efficiency of 60.00% have been demonstrated for frequencies around 60.00 GHz in [65] and [66].

On the other hand, for indoor communications at lower frequencies bands such as VHF, UHF or L bands, planar and non-planar leaky-wave antennas are also commonly employed. For instance, in [67] a leaky-wave antenna in SIW is implemented for wireless power transfer with possible applications to charging handhold devices. In [68], a leaky coaxial cable is installed inside a room to detect bad postures from patients in order to prevent ulcers and other bedsore symptoms. These cables are also used inside airplanes as airborne WiFi providers reducing death spots, as explained in [33].

2.2.1 Challenges for Leaky-wave Antennas

Leaky-wave antennas are versatile structures useful for many different applications and that can be implemented on different technologies as desired. Nevertheless, there are different issues that these antennas still need to overcome. Many studies have been focused on different alternatives to solve these constraints and allow leaky-wave antennas to be more attractive to modern applications. For example, when installed inside airplanes [33], leaky feeders present certain limitations. Modern airplanes can have many control systems that employ wireless technologies to acquire data from a large number of sensors [69, 70]. When these conventional implementations are cable based as well, it can be problematic in that additional fuel is required to support the weight limitations during flight. Leaky feeders are usually heavy and their radius of curvature is limited [9], this is because the placement of the cable on a bended area could lead to the obstruction of the radiating slots preventing the radiation to occur. Moreover, if the leaky feeder antenna got an accidental cut the whole cable would have to be replaced, being an expensive and involved process.

Alternatively, more classic and non-adaptive distributed antenna systems have also been widely used in the past for indoor wireless communications to reduce leaky feeder limitations [71]. These systems generally consist of several standard antennas separated by a few wavelengths and connected by a coaxial cable [71, 72]. Therefore, the typical range of frequencies for these structures is dependent on the type of antennas selected for the distributed antenna systems, which offers an alternative for leaky feeders at higher frequencies. Previous studies found in the literature have been focused on the enhancement of these kind of systems for the indoor communications such as the analysis of fading channels [73, 74] or the calculations for the optimum antenna location [75, 76]. There have also been some research on distributed antenna systems in high speed trains where wireless coverage is complicated due to continuous handover at high speeds [77, 78] that could replace leaky feeders [30–32]. Yet, leaky feeders or current distributed antenna systems do not offer any adaptive and simple switching mechanism to selectively distribute RF power within the coverage area, which leads to lower transmitted levels that may not satisfy the higher data requirements nowadays.

Furthermore, when moving towards higher frequencies, antenna designers struggle to find a simple, efficient and fully integrated feeding network for certain planar

1D leaky-wave antennas. This is very common for dielectric image guide and SIIG configurations given their physical characteristics. The typical feeder for dielectric image guide structures is a horn-shaped waveguide [66, 79], which consists of a tapered dielectric section inserted into the open waveguide horn. However, integrating this system in a planar form is not easy as the junction between the dielectric image guide and the planar device can introduce losses from impedance mismatching or unwanted radiation [66, 79]. To reduce the impedance mismatch, the use of microstrip-fed slots on the ground plane or a flared conducting strip from the microstrip line to the dielectric image guide have already been proposed [80–82]. Nevertheless, these structures are less efficient, e.g., insertion losses around 2.5 dB for the flared conductor strip, and can be complex to manufacture requiring tapered dielectrics with intricate milling process that prevent mass production. Additionally, SIIGs are normally fed by coplanar waveguides connected to horn waveguides transitions [83]. This involves complex manufacturing for millimetre-wave and optical frequencies as lasers are needed to avoid the air gap between the ground plane and the dielectric, making this system not very popular for low cost applications.

One solution available is the use of surface-wave launchers that are common for grounded dielectric slabs and can achieve efficient ($> 80.00\%$ launching efficiency) and uniform wavefront excitation of the fundamental surface-wave mode [60, 84–88]. This can be achieved using simple technologies such as microstrip lines or truncated parallel-plate waveguides. Surface-wave launchers are also typical for 2D leaky-wave antennas as they can provide fully planar configurations. Some surface-wave driven structures that have been recently reported exploits surface-waves for the transformation from a slow guided wave to a fast leaky-wave mode [84, 89–91]. As shown in these studies, planar Yagi-Uda like slot arrangements in the ground plane can couple power into the dominant TM_0 surface-wave mode of a grounded dielectric slab. Cylindrical-waves can be observed with radial propagation along the planar guiding surface. These printed structures are also typically fed by coplanar waveguide transmission lines, and this means that the launcher system is typically implemented in the ground plane. This might not be practically favoured when a continuous metallic backing is required for low profile positioning on an airplane fuselage for example.

Other possibility is to employ leaky-wave features for feeding purposes. For instance,

the independent control of the phase and attenuation constants [6,57] may allow to direct the excited leaky-wave in one direction or in other, while also being able to create uniform wavefront propagation by controlling the phase constant. One example where the use of leaky-waves has been demonstrated to be useful is when feeding slot array systems, where efficient aperture illumination and element excitation are critical for the performance of the antenna. In [6], a partially reflective surface based on leaky-wave theory was implemented to illuminate the reflectors used to feed the slot array. In this case, the application of quasi-optical concepts to create a planar and fully integrated structure was studied, where reflected waves eventually formed a uniform field distribution starting from a cylindrical leaky-wave. The use of two parabolic reflectors required to generate the desired wavefront makes this antenna electrically large, as the main reflector was at least $5\lambda_o$ in size (2.5 times the wavefront), being larger the feeding network than the antenna array. Some systems have also been fed by two coaxially fed probe pins (perpendicular to the ground plane) to shape and control the cylindrical-wave launched inside the parallel-plate waveguide when using a partially reflective surface for leakage, such as in [92]. This type of feed arrangement can easily excite the reflector system, however, at the same time, does not allow for simple integration and compact feeding of linear slot arrays. Also, some undesired mutual coupling effects between the sources can be problematic in these designs, requiring some compensation techniques to enable the desired parallel-plate waveguide field launching and antenna radiation when considering grid-based slot arrays.

Different feed network arrangements have been investigated previously using various approaches with application to slot antenna arrays etched on the top conducting layer of parallel-plate waveguides. For example, the concept of integrated launching of a uniform transverse electromagnetic (TEM) mode for slot arrays was introduced in [4], where a coaxial-fed rectangular metallic waveguide was placed under the parallel-plate substrate. This feed system operated at 11.50 GHz with an efficiency of almost 50.00% by means of coupling slots on top of the waveguide. Moreover, this technique required a multi-layer implementation which increased the volume and manufacturing complexity of the launching system.

In order to avoid such multilayer structures, several approaches to uniformly distribute the TEM field have been proposed for more planar implementations. For

example, the use of metallic walls was proposed in [93] as a series of T-junctions inside an air-filled parallel-plate waveguide. Dense post-walls were also employed in [5] acting as narrowband coupling windows, which required careful design for each cavity to efficiently set the phase and amplitude along the structure. While the amplitude stays fairly constant with variations of $\pm 5.00\,\mathrm{dB}$ and $\pm 3.00\,\mathrm{dB}$ in [93] and [5], respectively, uniform phase can be difficult to achieve for the excited field at the design frequency. For instance, a decrease of $60.00°$ in phase was observed in [93] for the T-junctions cavities while phase variations between $10.00°$ and $-20.00°$ were observed for the post-wall structure in [5]. These structures reduce the launcher size while sacrificing design and manufacturing simplicity, but yet do not obtain a uniform amplitude and phase distribution.

When conical beam scanning is required for radars or other tracking applications, the trend is to use phased-array structures since they provide same features in terms of high directivity and beam steering capabilities [43,94,95] as leaky-wave antennas. Nevertheless, low-cost and efficient designs can be complex or challenging to achieve due to the different passive or active elements needed to feed and control the radiation of the elements within the array [43, 95]. Therefore in the recent years, the interest for steerable planar conical beam configurations is increasing as a low-cost and efficient alternative in such applications, specially at millimetre-wave frequencies [96]. However, fully planar and low-profile designs seem difficult to achieve. For instance in [97], a wideband horizontally polarised conical beam for wireless applications was explored. This configuration can seem bulky as it is implemented by a pair of sectorial-shape horizontal plates achieving a gain of $5.00\,\mathrm{dBi}$. Alternatively, a linearly polarised (LP) antenna with switchable radiation from a conical beam to broadside was implemented in [98]. This structure has three layers, an RF switch circuit on the bottom, a monopolar patch on the central layer and a L-probe fed patch antenna on top. While the antenna efficiently radiates a conical beam, the design is still very intrincate and non-planar. A more compact design is presented in [96], where an open circular waveguide fed by a coaxial probe excites a conical beam with gain values around $9.00\,\mathrm{dBi}$ for the K_a band. A circular grounded dielectric slab is required as a transition between the probe and the circular waveguide. This causes some losses and limits the impedance bandwidth in the system. A fully planar design is presented in [99] based on a coplanar annular ring microstrip an-

tenna with shorting strips. Nevertheless, this design has a maximum pointing angle of 40.00° and a broad beamwidth being unsuitable when high directivity is required. Other feeding networks for these systems are based on directive folded magnetic dipoles implemented on the ground plane to keep a fully integrated system when single layer structures are required [84, 89]. This can be problematic if the structures do not allow for ground plane modifications because of the presence of another metallic surface under or very close to the ground plane.

These limitations will be addressed in the following chapters of the thesis, presenting planar alternatives to improve the current state-of-the-art.

2.3   Relevant Background Theory

Leaky-wave and surface-wave propagation have been key concepts for the development of this research. Therefore, fundamental theory to provide a better understanding of the structures implemented on this thesis will be discussed next.

A surface-wave is a type of travelling-wave that is propagating on the interface between the dielectric material and the air as depicted in Fig. 2.4. They are excited by a source and propagate along a guiding media until they reach a discontinuity where they get radiated in the end-fire direction or reflected back to the source [100, 101]. Their excitation is commonly avoided since it can significantly affect the expected radiation performance of systems implemented on the same material [60, 100, 102].

Assuming a lossless grounded dielectric slab as the guiding media, surface-wave propagation normally occurs horizontally parallel to the air-dielectric interface, while its amplitude decays vertically when travelling away from the source (see Fig. 2.4) [100, 103–105]. Due to this vertical attenuation, the phase constant β only exists in the longitudinal axis, while the attenuation constant α varies in the transverse direction. This also implies that surface-wave propagation is independent of the other axis (in this case, the y-axis, see Fig. 2.4). Thus, the wavenumbers in the relevant axis can be defined as [60, 100]:

$$k_z = -j\alpha_z \tag{2.3.1}$$

$$k_x = \beta_x \ . \tag{2.3.2}$$
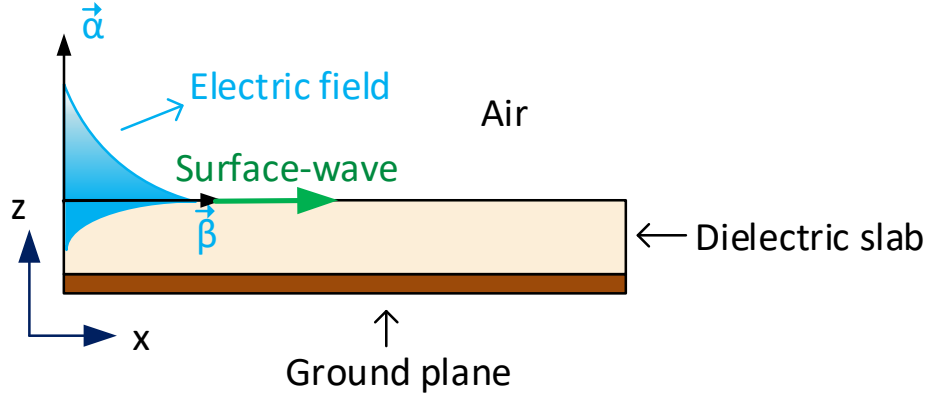
Figure 2.4: Diagram of surface-wave propagation considering a grounded dielectric slab.

Surface-waves are considered slow-waves since their phase velocity is always less or equal to the velocity of air in the hosting media, or in other terms, the phase constant is higher than the propagation constant in free-space ($\beta_x > k_0$) [106]. Another key feature of surface-waves on a grounded dielectric slab is that TM and TE modes are present after a certain cutoff frequency, however, there is always a fundamental mode propagating, the TM_0 [102].

On the other hand, the work carried out by Oliner and Jackson [3, 107–112] helped with the understanding of the phenomena behind leaky-wave radiation, which is more complex than its surface-wave counterpart. Leaky-waves are defined as radiating fast-waves ($\beta < k_0$) that leak energy continuously while propagating as a travelling-wave in a guiding media [109]. For simplicity purposes, a lossless grounded dielectric slab will be used again for explanations as shown in Fig. 2.5. The leaky-wave propagates away from the source leaking energy along the structure, for example, through the periodic perturbations on top of the grounded dielectric slab. Due to this leakage the longitudinal and transverse wavenumbers are complex and defined as [3]:

$$k_x = \beta_x - j\alpha_x \tag{2.3.3}$$

$$k_z = \beta_z - j\alpha_z \tag{2.3.4}$$

which are related as $k_z = \sqrt{k_0^2 - k_x^2}$, being k_0 the propagation constant in the free-space, calculated as $k_0 = \omega\sqrt{\mu_0\varepsilon_0}$, where ω is the angular frequency, μ_0 and ε_0 the permeability and permittivity in free-space respectively.

Furthermore, a leaky-wave can be classified as improper or proper depending on its
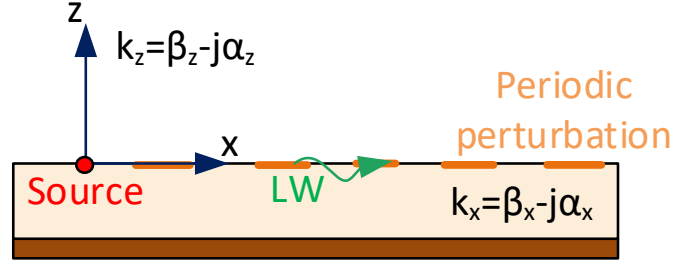
Figure 2.5: Diagram of a leaky-wave antenna where the bound fields are perturbed by the periodic strips placed at the air-dielectric interface, causing them to radiate.

radiated fields behaviour. If the leaky-wave is defined as improper, assuming the wave propagates in the x-direction and radiating away from the guiding surface, the fields in the air region are exponentially increasing ($\alpha_z > 0$) while decreasing in the guided region as the field propagates longitudinally [111, 112]. This behaviour determines the wave as forward, i.e., phase and group velocities are in the same direction. This means that the beam will scan from broadside to forward end-fire [3]. This is illustrated in Fig. 2.6, where the phase constant vector is depicted in an arbitrary slab supporting leaky-waves with darker green colors reporting stronger radiated fields. On the contrary, if a leaky-wave is defined as proper then the radiated fields decay exponentially in the vertical direction away from the source (see Fig. 2.6). In this case, the leaky-wave is a backward wave whose group and phase velocities are in opposite directions, and the beam steering, in this case, is from backward end-fire to broadside [3]. The direction of radiation, assuming α_x to be small, is then defined by [113]:

$$\sin \theta_0 = \frac{\beta_x}{k_0} \quad . \tag{2.3.5}$$

Eq. (2.3.5) indicates that the main lobe pointing angle increases with frequency, which causes the beam scanning behaviour typical from leaky-wave antennas.

In turn, the beamwidth of these radiated fields in the far-field is [3]:

$$\Delta \theta_0 = \frac{2\alpha_x}{k_0 \cos \theta_0} \tag{2.3.6}$$

and the efficiency:

$$\eta = 1 - e^{-2\alpha_x L} \tag{2.3.7}$$

where L is the length of the antenna aperture and λ_0 the free-space wavelength ($\lambda_0 = c/f$, c is the speed of light and f is the frequency of operation).
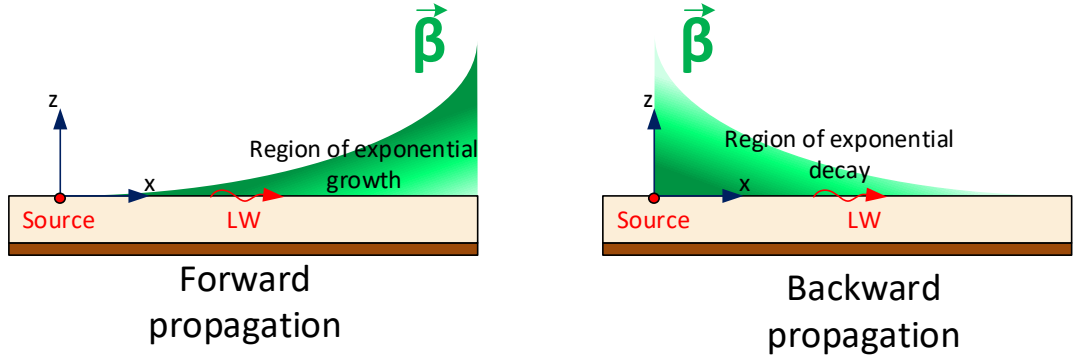
Figure 2.6: Schematic of leaky-wave antenna radiation regions for the improper (left) and proper type (right). Darker green regions illustrate stronger radiated fields.

Highly directive pencil beams can be achieved if β_x and α_x are made small enough, at the penalty of requiring large antenna apertures L. The radiating performance of the leaky-wave antennas significantly depends on the attenuation constant and the physical length of the antenna aperture [60].

In the case of uniform leaky-wave antennas, typically only forward leaky-waves are supported as the radiation mechanism is based on a continuous discontinuity where the fast travelling-wave is leaking energy [3,13]. On the contrary, for periodic leaky-wave antennas (2D or 1D fed at the center), backward and forward leaky-waves can be supported. This could entail a two-sided beam pattern with both beams scanning from end-fire to broadside (see Fig. 2.7) until merging together at broadside where the open stopband region explained in Section 2.2 will happen. In this region, radiation performance is very poor and high reflections will occur [113].

Moreover, the slow-wave propagation when considering periodic leaky-wave antennas can be perturbed to become a leaky fast-wave and decomposed into an infinite number of spatial harmonics or Floquet's modes [19–21] characterised by a phase constant β_n, which in turn is related to the fundamental harmonic ($n = 0$) and by the mathematical representation following the Bloch-Floquet's theorem [3,20,21]:

$$\beta_n = \beta_0 + \frac{2n\pi}{d} \tag{2.3.8}$$

where n is the harmonic order and d is the periodicity of the perturbing element. The space harmonic phase constant, β_n, mainly depends on the periodicity d and the frequency of operation, whereas the leakage rate for the different harmonics is defined by the periodic leaky-wave antenna aperture that alters the fundamental
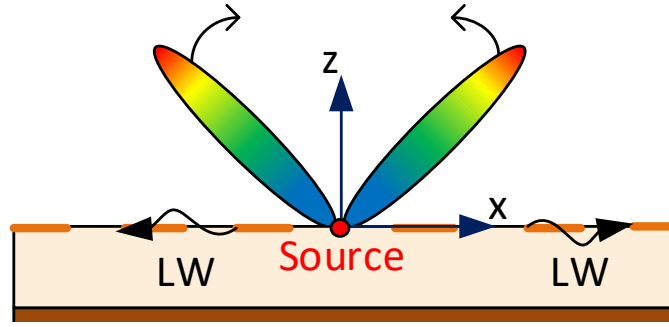
Figure 2.7: Diagram of a periodic leaky-wave antenna where two-beams radiate from end-fire and scan towards broadside with an increase in frequency.

harmonic. The harmonics of order $n > 0$ and $n < 0$ are defined as the positive and negative space harmonics [3, 60]. In this thesis, the structures utilised will only excite the fundamental $n = 0$ and the $n = -1$ harmonics. The phase constant β_0 of the fundamental or unperturbed mode sets the direction of propagation of the bounded wave.

2.3.1 Frequency Regimes

Depending on the frequency of operation, different solutions for the waves can be obtained for an arbitrary dielectric slab, which implies that the leaky-wave regime can only be achieved under a certain frequency range for a propagating mode above cutoff [108]. These regimes are all summarised in Fig. 2.8, where it can be seen that there are five possible frequency regions for the mode to operate in a different way, the key feature for the mode to behave as a radiating leaky-wave is to work in the so-called physical region [100, 108]. This means that the leaky-wave wavenumber is in the fast-wave region ($\beta_x < k_0$) and with a small attenuation constant [108, 111, 112].

The other regimes are also important and present different performance bands for the mode of interest, as explained next. Starting above the cutoff regime ($f > f_c$), there are two solutions for the longitudinal phase constant in the media β_x, a proper surface-wave ($\alpha_z > 0$) and an improper surface-wave ($\alpha_z < 0$) which are by nature slow-waves [3]. The proper surface-wave will be propagating (but not radiating) with the fields vertically decaying away from the source, while the improper one will never be physical [3]. This frequency region above cutoff ($f > f_c$) is also called the passband region where the longitudinal wavenumber is purely real in lossless media due to the absence of leakage ($k_x = \beta_x$) and the transverse one is imaginary

$(k_z = \alpha_z)$ [3, 60, 108].

As soon as the frequency is lowered towards cutoff, the phase constant starts decreasing being equal to k_0 at cutoff $(f = f_c)$ [108]. Below this frequency, the proper surface-wave mode will become an improper surface-wave with an increasing phase constant until reaching the splitting point frequency $(f = f_s)$. In this frequency range $(f_s < f < f_c)$, a stopband region for the slow surface-waves is defined, where the attenuation constant is typically high causing the mode to be reactive and with significant field attenuation along the structure [60, 108].

Once the splitting point is reached $(f = f_s)$, the two improper surface-waves merge to then divert into two complex leaky-wave solutions where one is the conjugate of the other, i.e., having the same β but different α, and is considered non-physical since it grows exponentially in the direction of propagation [108]. The other solution reaches then the physical frequency point $(f = f_p)$, where the leaky-wave enters in the fast-wave region and starts to strongly radiate. This is called the radiative region $(f_l < f < f_p)$, where the leaky-wave has an almost real transverse wavenumber k_z [60]. In this region, there is also a frequency for which the attenuation constant decreases to zero preventing radiation and therefore, creating a leaky-wave stopband region [113]. The frequency region between the cutoff frequency and the physical frequency point $(f_p < f < f_c)$ is called the spectral gap, where the mode is improper and non-physical [108, 111, 112].

If going lower in frequency $(f < f_l)$, the mode will become again a non-physical leaky-wave where its attenuation constant, which mainly corresponds to reactive attenuation and not to antenna leakage, increases significantly achieving values higher than the phase constant [60, 108]. There is no radiation in this region as the mode quickly attenuates along the antenna aperture. These regions are all summarised in Fig. 2.8.

2.3.2 Cylindrical Leaky-wave Antennas

2D leaky-wave antennas behave differently from their 1D counterparts as they support cylindrical leaky-waves that propagate radially outward. This produces an omnidirectional conical beam pattern perpendicular to the antenna aperture [3, 109], which create a two-sided beam pattern in the $z - y$ plane. One example of such 2D
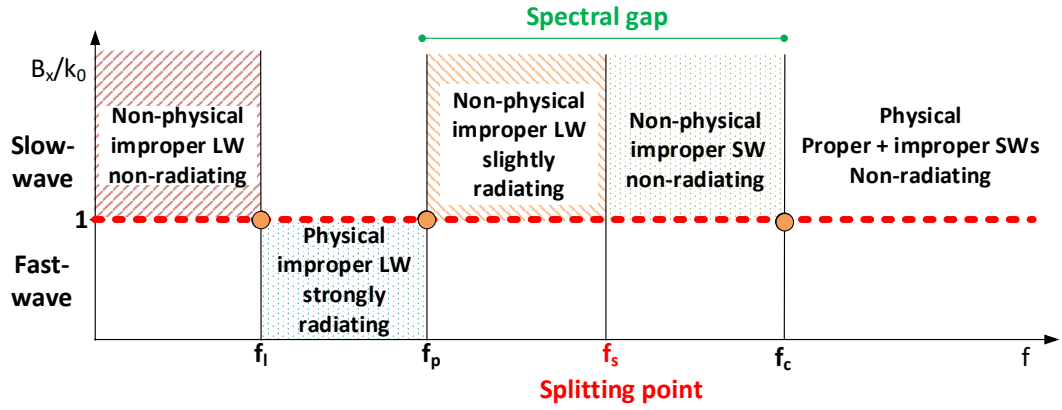
Figure 2.8: Mode regimes for the different frequencies of operation with respect to the normalised longitudinal phase constant, β_x/k_0. Red dashed line represents when $\beta_x = k_0$ and the circles for the frequency points when this occurs, i.e., the lowest physical regime frequency (f_l), the physical point (f_p) and the cutoff frequency (f_c). Coloured sections report whether the wave is a slow or a fast-wave for each frequency region.

leaky-wave antenna can be a grounded dielectric slab with one or several layers with a metallic partially reflective surface on top excited by a finite source (see Fig. 2.9), where the antenna aperture is defined by the interface between the grounded dielectric slab and air (z=0).

Cylindrical leaky-wave modes can either be defined as TE_z or TM_z, where the TM_z mode mainly determines the field component in the elevation plane, E_θ in the far
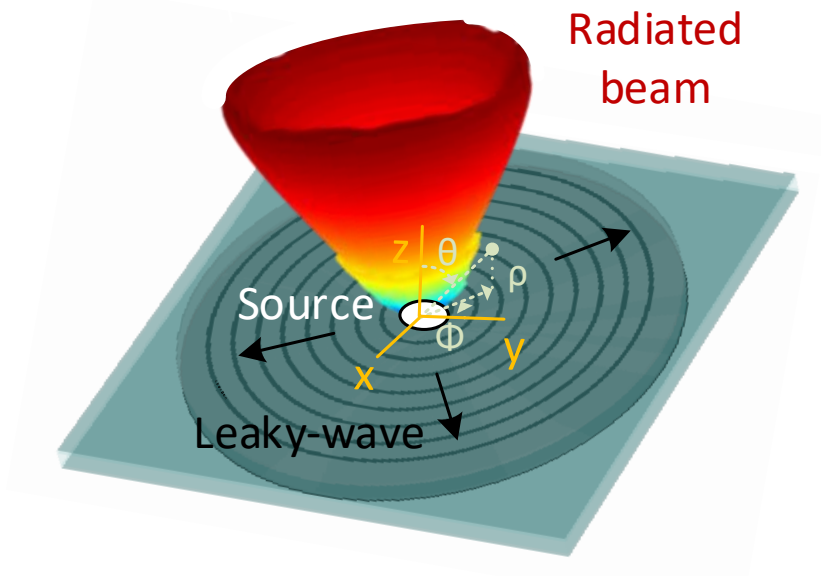
Figure 2.9: Schematic for an arbitrary planar cylindrical leaky-wave antenna showing the typical omnidirectional conical beam.

field, whereas the TE_z determines the far-field in the azimuthal plane E_Φ, defining the beamwidth in the E-plane and H-plane respectively [108]. Closed-form equations for low order modes excited by a vertical or horizontal (launching $n = 0$ and $n = 1$ order modes respectively) electric or magnetic dipoles were developed in [107] for infinite and truncated apertures. These modes were of interest as they would be the only ones excited by an infinitesimal electric or magnetic dipole source. Moreover, their main feature is that there is no variation in the azimuth plane Φ for $n = 0$ while there is a sinusoidal variation in Φ for $n = 1$ [107]. In this thesis, the focus will be on $n = 0$ modes as the source used for the designed and manufactured cylindrical leaky-wave antennas is a vertical dipole, however vector potential functions for $n = 1$ modes will be similar to the ones described below but with the addition of sinusoidal functions describing the azimuthal variations. Detailed explanations and closed-form expressions can be found in [107].

The magnetic vector potential component A_z describing the TM_z and the electric vector potential component F_z describing the TE_z (as TM_z and TE_z only have electric and magnetic field components in the z-direction respectively) excited by a vertical electric or magnetic dipole ($n = 0$ mode excitation) are defined as follows above the aperture [107]:

$$A_z(\rho, z > 0) = \frac{1}{2} H_0^{(2)}(k_\rho^{TM} \rho) e^{-jk_z^{TM} z} \tag{2.3.9}$$

$$F_z(\rho, z > 0) = \frac{1}{2} \frac{\omega \mu_o}{k_z^{TE}} H_0^{(2)}(k_\rho^{TE} \rho) e^{-jk_z^{TE} z} \tag{2.3.10}$$

where $H_0^{(2)}(\cdot)$ is the zero th-order Hankel function of the second kind (due to azimuthal symmetry) with respect to its argument, k_ρ is the radial complex propagation wavenumber of the cylindrical leaky-wave and k_z is the transverse wavenumber defined by $k_\rho^{TM,TE} = \beta - j\alpha$ and $k_z^2 = k_0^2 - k_\rho^2$ respectively (with free-space wavenumber $k_0 = \omega\sqrt{\varepsilon_0 \mu_0}$, where ω is the angular frequency, μ_0 and ε_0 the permeability and permittivity in free-space respectively and the time dependence e^{+jwt} suppressed here and throughout the chapter).

Once the expressions for the electric and magnetic vector potential components are known, magnetic fields can be derived allowing the electric current distributions in the antenna aperture for both modes to be defined by [107]:

$$J_\rho = -k_\rho^{TM} H_1^{(2)}(k_\rho^{TM} \rho) \tag{2.3.11}$$

$$J_\Phi = \frac{1}{2} k_\rho^{TE} H_1^{(2)}(k_\rho^{TE} \rho) \ . \tag{2.3.12}$$

Following [107], the radiation patterns for an infinite aperture for the TM_z case are

$$E_\theta = \frac{j\omega\mu_0}{\pi r} \frac{\sin\theta}{(\frac{k_\rho^{TM}}{k_0})^2 - \sin^2\theta} \cdot e^{-jk_0 r} \tag{2.3.13}$$

$$E_\Phi = 0 \tag{2.3.14}$$

and for the TE_z case

$$E_\theta = 0 \tag{2.3.15}$$

$$E_\Phi = -\frac{j\omega\mu_0}{\pi r} \frac{\sin\theta}{(\frac{k_\rho^{TE}}{k_0})^2 - \sin^2\theta} \cdot e^{-jk_0 r} \ . \tag{2.3.16}$$

These fields produce an omnidirectional conical beam that can be polarised with the electric field in the elevation (TM_z) or azimuthal direction (TE_z). For both cases, the maximum radiation beam angle, θ_P, depends mainly on the phase constant β when the leaky-wave is lightly attenuated ($\alpha << \beta$) as

$$\sin\theta_P = \frac{\beta}{k_0} \tag{2.3.17}$$

while the beamwidth is related to the attenuation constant α

$$BW = \frac{2\alpha}{k_0 \cos\theta} \ . \tag{2.3.18}$$

Normalised radiation patterns are calculated and shown for TM_z with different α and β values in Figs. 2.10 and 2.11. As it was expected following Eqs. (2.3.17) and (2.3.18), for lower values of β, the pointing angle of the radiated beam scans towards broadside and vice-versa. On the other hand, if α is varied, the beamwidth changes becoming narrower for smaller values. It must be noted that when α and β are equal and low enough (see yellow curve in Fig. 2.10) the narrow-beam is pointing almost at broadside, nevertheless it will never completely reach broadside as there will always be a null. To avoid this, higher order modes ($n = 1$) can be excited in a dielectric layered configuration [107]. However, despite how small α could get, a narrow-beam at broadside could only be achieved if the components of both modes are equal ($\hat{\alpha}^{TM} = \hat{\alpha}^{TE} = \hat{\beta}^{TM} = \hat{\beta}^{TE}$). Moreover, in Fig. 2.11 it can be observed that there is a beam squint for $\alpha = 0.5$, this is due to the fact that β is no longer
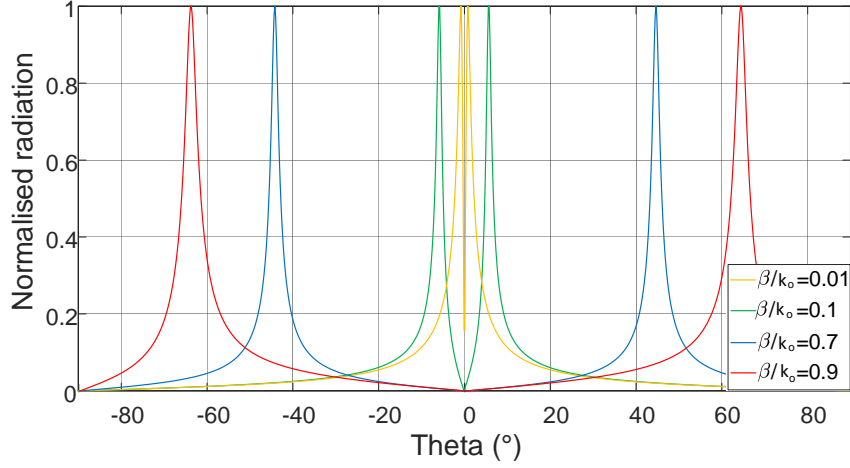
Figure 2.10: Plot of normalised radiation patterns ($|E_\theta|$) for different values of β for a fixed $\alpha(= 0.01)$.
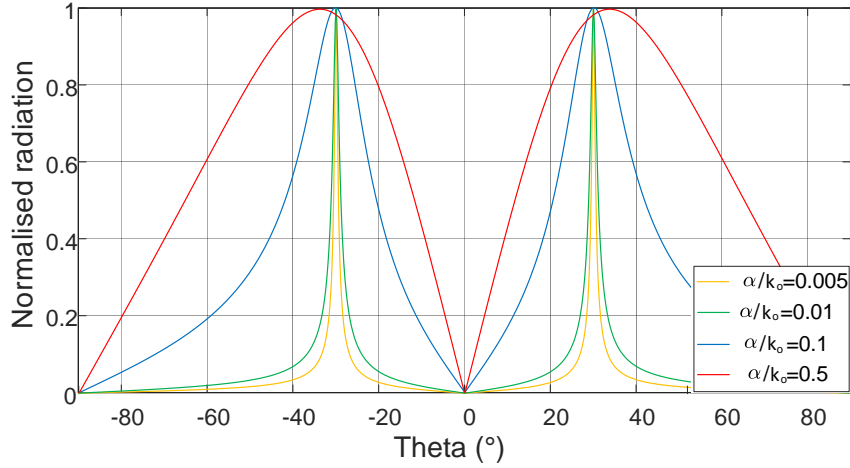
Figure 2.11: Plot of normalised radiation patterns ($|E_\theta|$) for different values of α for a fixed $\beta(= 0.5)$.

the main parameter in Eq. (2.3.17) and therefore a more accurate equation should be used [113]:

$$\theta_P = \arcsin \sqrt{\left(\frac{\beta}{k_0}\right)^2 - \left(\frac{\alpha}{k_0}\right)^2} . \qquad (2.3.19)$$

For practical cases the antenna aperture cannot be infinite and the radiation pattern will not be ideal. Instead, for smaller apertures, higher side lobe levels related to the unwanted radiation can appear and occur at the edges [107]. To better predict this behaviour, equations for a finite aperture, defined for the region $a < \rho < b$, are also obtained for the TM$_z$ fields as [107]:

$$E_\theta = \frac{-\omega\mu_0 k_\rho^{TM}}{r((k_\rho^{TM})^2 - k_0^2 \sin^2\theta)} [k_0\rho' J_0(k_0\rho' \sin\theta) H_1^{(2)}(\rho' k_\rho^{TM}) \sin\theta$$

26

$$- k_\rho^{TM} \rho' J_1(k_0 \rho' \sin \theta) H_0^{(2)}(\rho' k_\rho^{TM})]_{\rho'=a}^{\rho'=b} \cdot e^{-jk_0 r} \tag{2.3.20}$$

$$E_\Phi = 0 \tag{2.3.21}$$

and for the TE_z

$$E_\theta = 0 \tag{2.3.22}$$

$$E_\Phi = \frac{\omega \mu_0 k_\rho^{TE}}{r((k_\rho^{TE})^2 - k_0^2 \sin^2 \theta)} [k_0 \rho' J_0(k_0 \rho' \sin \theta) H_1^{(2)}(\rho' k_\rho^{TE}) \sin \theta$$

$$- k_\rho^{TE} \rho' J_1(k_0 \rho' \sin \theta) H_0^{(2)}(\rho' k_\rho^{TE})]_{\rho'=a}^{\rho'=b} \cdot e^{-jk_0 r} \tag{2.3.23}$$

where J_0 and J_1 are the Bessel functions of the first kind of zero and first order with respect to their arguments.

2.3.3 Leaky Feeder Antennas for Indoor Communications

A leaky feeder antenna mainly consists of a periodically slotted coaxial cable that couples energy to and from different receivers through its forward leaky-wave radiation [27], see Fig. 2.12.

In the past, researchers could not accurately explain the leaky-wave mechanism that
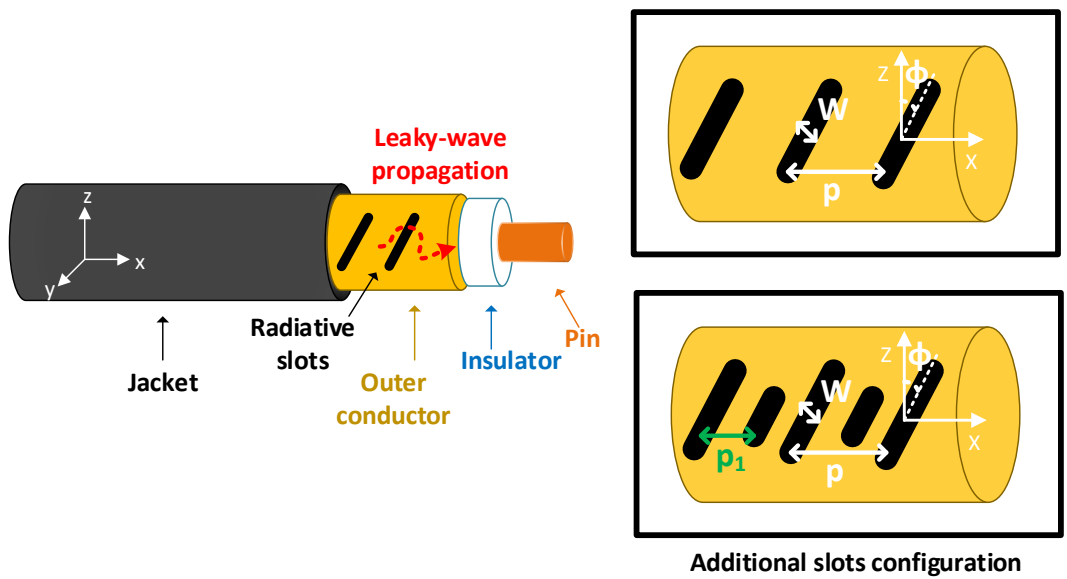
Figure 2.12: Schematic of an arbitrary leaky feeder antenna and the detailed slot configurations covered by the insulating jacket.

causes the radiation in this structure. Instead, two modes used to be defined as the source of this particular performance: the bifilar mode, which is confined between the central pin and the outer conductor and is responsible of the leakage (the actual quasi-TEM), and the monofilar mode, which is considered a surface-wave that is propagating in the outer conductor due to reflections at the slots (higher TM modes excited at the discontinuity) [8, 28, 29, 114]. However nowadays this type of antenna can be easily seen as a 1D periodic leaky-wave antenna whose principle of operation is based on the perturbation of a propagating slow-wave, the quasi-TEM, by a series of discontinuities (i.e., slots) causing its radiation [8]. These periodic slots allow to define the propagating quasi-TEM mode as an infinite number of space harmonics or Floquet modes [19–21]. In the leaky feeder antenna configuration, the main target is to only radiate the fast $n = -1$ harmonic of the quasi-TEM mode in order to achieve optimum radiation performance in the forward direction ($\beta_{-1} > 0$) [8], otherwise bidirectional radiation would occur causing high reflections of the transmitted signal compromising performance. This is because leaky feeder antennas are normally fed at one end and that a bidirectional beam is typically supported from a structure that is fed at the center. The lowest and highest frequencies that define the region where this condition is satisfied can be found using [27]:

$$f_L = \frac{c}{P(\sqrt{\varepsilon_r} + 1)} \qquad (2.3.24)$$

$$f_H = \frac{c}{P(\sqrt{\varepsilon_r} - 1)} \qquad (2.3.25)$$

where c is the speed of light in free-space and ε_r the relative permittivity of the insulator. These frequency ranges for different periodicities P are depicted in Fig. 2.13, where it is shown that smaller values of P allow the leaky feeder antenna to operate in a mono-harmonic configuration over a wider frequency range. However, this would entail an increment in the coupling losses as if the slots are not separated enough, the interference between them for the radiated fields becomes significant [8]. Moreover, if the cable operates in its surface-wave regime and not in the leaky-wave range, coupling losses would also be considerably increased, as most of the radiated power is bounded near the outer conductor which can cause a high attenuation in the radiated fields [8].

On the other hand, to avoid the excitation of higher order harmonics and keep the structure mono-harmonic, additional slots are required between period P (see
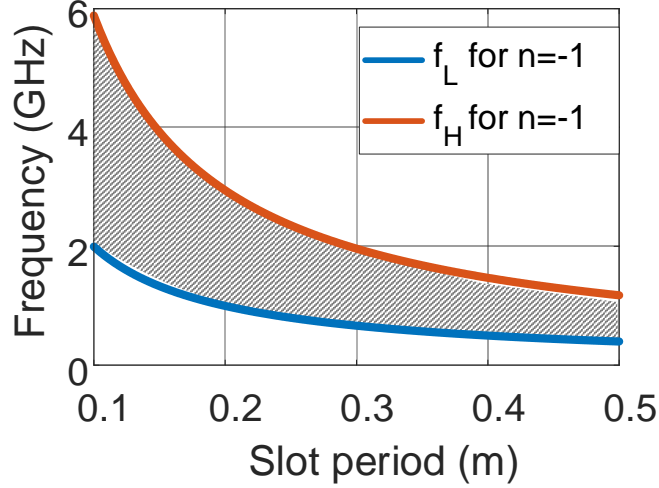
Figure 2.13: Plot of the frequency ranges where only the $n = -1$ harmonic is radiated for different slot periods P (shadowed region). The red solid line represents the highest frequency in the range while the blue line is the lowest one.

Fig. 2.12) to efficiently delay in frequency the excitation of these harmonics [8]. The periodicity P_1 for the additional slots is given by [8]:

$$P_1 = \frac{P}{2(\xi + 1)} \tag{2.3.26}$$

where ξ is the number of extra slots per period.

In addition, there are important constraints related to the losses existing in the structure that a designer needs to take into consideration to implement an efficient leaky feeder antenna. These systems require two types of losses to be assessed: longitudinal and coupling losses [27, 28]. While longitudinal losses are straightforward to calculate, coupling losses are challenging due to their dependence with internal and external factors that leads to uncertainties when theoretically predicting the leaky feeder antenna behaviour. Longitudinal losses are ideally found by basic transmission line theory in coaxial cables [115] and should be set as low as possible to maximize the operating length of the cable.

Coupling losses are not that obvious as they depend on the slots arrangement, their size and shape, while also on environmental factors, such as the position of the cable in the tunnel or corridor or multipath propagation, making this parameter difficult to predict by theory. Coupling losses are defined to be the ratio between the power excited into the cable and the power received in a mobile station at a fixed distance from the cable [34]. Moreover, as the coupling loss is a local parameter of each slot, the characterization of the entire cable requires these losses to be defined in

a statistical fashion. Thereby, two different values of coupling losses are provided by most manufacturers, the 95.00% and the 50.00% of the reception probability, meaning that the 95.00 or the 50.00% of the tested data are less than a certain value of given loss [8]. The distance where these losses are measured also affects the obtained value, therefore a standard distance of 1.50 or 2.00 m has been widely adopted [8, 34]. Furthermore, if the cable is operating low enough in frequency (VHF band especially) external effects such as the tunnel cutoff frequencies or wall materials need to be considered for the loss calculations [27, 29]. One option to reduce these coupling losses is to rotate the slots from the vertical position to an angle ϕ (see Fig. 2.12), however a trade-off is necessary for higher angles since the stability in the coupling losses is compromised with values oscillating along the slot length [8]. The equation that quantifies these losses is given by [8]:

$$A_c = -10 \log \frac{P_r}{P_t} = -10 \log \frac{0.13\lambda_0^2 |E|^2}{120\pi P_t} \tag{2.3.27}$$

being E the total radiated electric field, λ_0 the wavelength in free-space and P_t and P_r are the input power at the cable and the received power at a standard dipole antenna receiver, respectively.

The process to obtain closed-form equations for the radiated electric fields is quite involved and different techniques have been proposed through the years in the open literature, see for reference [8, 28, 29, 114, 116]. However, field equations depends on the shape and orientation of the slots, thus there are specific equations for the different configurations. In [114] for example, reflections and radiated fields in the far-field are found by combining Garlekin's and mode matching methods, where approximated closed-form equations for the radiated electric fields components in cylindrical coordinates for standard circular slots are defined as [114]:

$$E_z \approx 2j \frac{M_v(\cos\theta)}{r H_0^{(1)}(k_0 a \sin\theta)} e^{jk_0 r} \tag{2.3.28}$$

$$E_\theta \approx 2j \frac{M_v(\cos\theta)}{r \sin\theta H_0^{(1)}(k_0 a \sin\theta)} e^{jk_0 r} \tag{2.3.29}$$

where k_0 is the wavenumber in free-space ($k_0 = w\sqrt{\varepsilon_0\mu_0}$ where ω is the angular frequency, μ_0 and ε_0 the permeability and permittivity in free-space respectively), $H_0^{(1)}$ is the zero th-order Hankel function of the first kind with respect to its argument, r is the distance to the observation point, a is the radius of the outer conductor

and M_v is the magnetic surface current that generates the fields due to the slot approximated as a constant [114].

In general terms, leaky feeder antenna design is normally an involved process that varies depending on the slot configuration, cable properties and environmental factors. However, it represents a good solution for RF communications in complicated scenarios at lower frequencies (VHF and low UHF bands). On the contrary, if higher frequencies are required, coupling losses may be unbearable for most of the receiving devices and other systems, like the proposed smart cable, showing higher efficiency with less input power are then more suitable. In addition, leaky feeder antennas are normally expensive systems, with additional losses if the cable is installed in a curved fashion. For the practical case where a part of the cable becomes damaged, the propagation is disrupted and not repairable which can require a completely new cable.

2.4 Summary

In this chapter, the literature review and theory background have been discussed. It can be concluded that leaky-wave antennas have been significantly investigated in the literature during the last few decades, being extremely useful for planar and low-cost electrical beam steering applications. Moreover, leaky-wave antennas features include flexibility for implementation in different technologies such as dielectric image guides, SIIGs or Fabry-Perot cavities, being a reliable solution for higher frequency bands where other common technologies, such as microstrip, fail to provide good performance. Leaky-wave antennas not only show competitive features for modern applications but offer unique scanning capabilities that would require otherwise an involved design process using other kind of antennas.

Issues that motivate this research and that can be found when using modern leaky-wave antennas have been introduced. The focus is established on feeding networks and alternatives to bulky leaky feeders for indoor communications. When analysing the current feeding networks based on surface and leaky-wave launchers, complex, lossy or expensive configurations are found. Similar occurs to 2D leaky-wave antennas that become bulky multilayer or narrowband structures for conical beam radiation. In the case of indoor communications for WiFi or RFID configurations,

leaky feeders are employed which do not allow for selective distributed transmission. This can lead to unnecessary losses that are critical given the restrictive sensitivities for these applications.

The theory necessary to understand the designs that will be presented next is also explained. Special emphasis is made on general leaky and surface-wave theory as it is present in all the systems designed. Additionally, more specific theory such as cylindrical leaky-waves and leaky feeders is also introduced for conical radiation and selective transmission configurations.

Chapter 3

Simple Surface-wave Launcher for Leaky-wave Antennas

3.1 Introduction

In this chapter, a wideband, low profile and fully planar feeding network is proposed. It consists of a surface-wave launcher based on a truncated parallel-plate waveguide for one-dimensional (1D) leaky-wave antennas on grounded dielectric slabs, dielectric image guides and substrate integrated image guides (SIIGs) [117]. This launcher is designed to overcome the feeding limitations encountered when using these technologies for leaky-wave antenna implementation as outlined in Chapter 2.

Surface-waves can be efficiently excited ($> 80.00\%$ efficiency) and confined inside a dielectric [101]. These waves can be useful for feeding antennas that are placed on the same material allowing for full integration. A very practical way of launching a surface-wave into a grounded dielectric slab is the use of truncated parallel-plate waveguides [105, 113]. In [105] it is explained how a transverse magnetic (TM_0) surface-wave mode can be excited with a 90.00% efficiency by the truncation of a parallel-plate waveguide. With the addition of a sub-wavelength matching section composed of an array of square printed patches it is possible to tailor the modal phase constant β in order to avoid radiation losses while also increasing the coupling efficiency [118]. A low profile launcher can be obtained combining these two concepts as depicted in Fig. 3.1. In addition, a microstrip taper is used as a transition from the input microstrip line to the parallel-plate waveguide. Also, the use of a parallel-
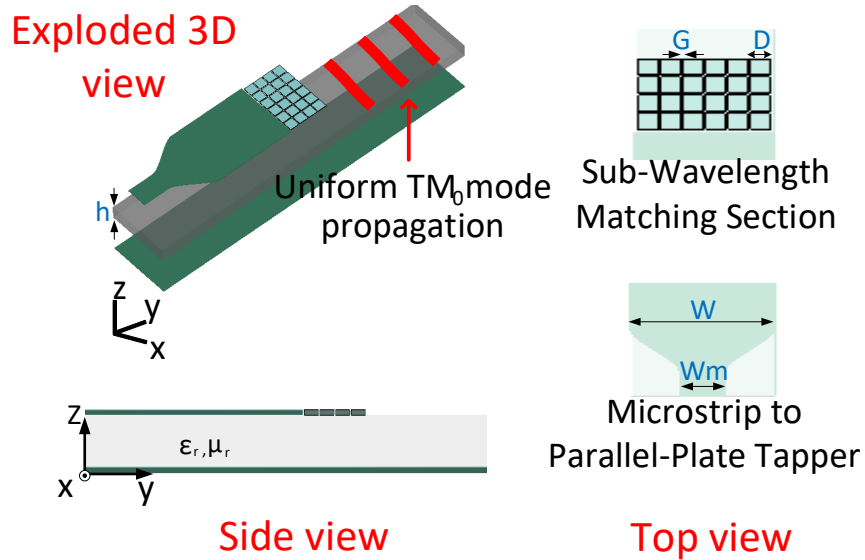
Figure 3.1: Diagrams of the proposed single-layer TM_0 mode launcher using parallel-plate waveguide technology consisting of the microstrip-to-parallel-plate waveguide transition, the truncated parallel-plate waveguide and a sub-wavelength matching section [85].

plate waveguide allows for simple and straightforward design while also low cost and compact implementation.

Theoretical analysis for surface-wave excitation on parallel-plate waveguides using Matlab [10] will be introduced. As a proof of concept, the launcher has been designed to work in different practical scenarios such as an end-to-end structure in a rectangular grounded dielectric slab, a leaky-wave antenna system and in millimetre-wave technologies as dielectric image guide and SIIG systems. These configurations are shown in Fig. 3.2. Simulation results obtained with CST [12] in its frequency domain solver will be presented. Further comparison with measurements of a prototype as well as the issues encountered when manufacturing will be discussed next.

3.2 Theoretical Approach

Due to the necessary discontinuity in the parallel-plate waveguide to excite the surface-wave, some of the incident power can be reflected, partly radiated, and the remainder coupled into the surface-wave on the grounded dielectric slab. Substrate parameters such as thickness h and relative permittivity ε_r, are key to achieve surface-wave coupling efficiencies up to 90.00% [105]. However, these parameters are restricted to the conditions where unimodal surface-wave propagation is en-

sured [105]:

$$k_0 h < \frac{\pi}{\sqrt{\varepsilon_r}} \qquad (3.2.1)$$

$$0 < \arctan(\frac{-1}{\sqrt{\varepsilon_r}} \tan(\sqrt{\varepsilon_r} k_0 h)) < \pi \qquad (3.2.2)$$

where k_0 is the free-space wavenumber ($k_0 = \omega\sqrt{\mu_0 \varepsilon_0}$, where ω is the angular frequency, μ_0 and ε_0 the permeability and permittivity in free-space respectively).

Two analysis for different relative permittivity ε_r and frequency values have been performed to assess the thickness that would satisfy conditions (3.2.1) and (3.2.2). The needed thickness, permittivities and frequencies resulting from these analysis are reported in Tables 3.1 and 3.2. According to these results, low relative permittivity dielectrics imply the use of thicker substrates, this is due to majority of the incident surface-wave remaining close to the upper plate area enabling pronounced radiation at the truncation of the parallel-plate waveguide if the substrate is not thick enough [100, 105]. On the other hand, higher frequencies restrict the available thickness range for a given relative permittivity. Therefore, a trade-off between
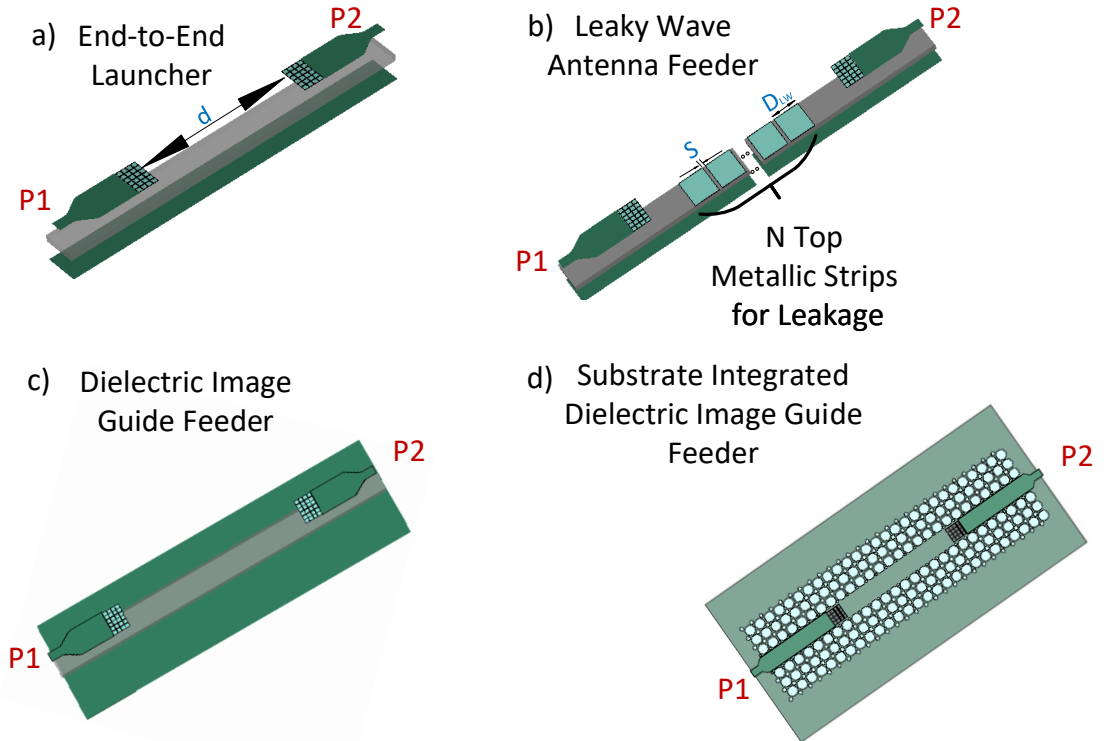
Figure 3.2: Schematics of the different configurations employing the planar surface-wave launcher: (a) the end-to-end test structure in a rectangular grounded dielectric slab, (b) the leaky-wave antenna system, (c) the dielectric image guide and (d) the SIIG feeders.

Table 3.1: Regions for unimodal propagation for different values of relative permittivity ε_r and thickness h, at a fixed frequency of 24.00 GHz

Relative Permittivity	Range of Dielectric Thickness (mm)
10.2	1.00-1.50
8	1.50-2.00
6	1.50-2.50
4.3	2.00-3.00
2.4	2.00-3.50

Table 3.2: Regions for unimodal propagation inside the grounded dielectric slab for different frequencies and thickness h, for a fixed relative permittivity of 10.2.

Frequency (GHz)	Range of Dielectric Thickness (mm)
10.00	1.00
15.00	1.00-1.50
20.00	1.50-2.00
30.00	2.00-3.00
35.00	2.50-4.00

finding high relative permittivity materials and achieving low frequency operation would be necessary for a compact and simple design.

Once the ranges of substrate relative permittivity, thickness and frequency values for unimodal propagation are set, parameters can be chosen using design curves [105], where formulas relate these parameters with the reflection coefficient, surface-wave coupling and radiation efficiency. These curves are calculated in terms of normalised thickness $k_0 h$ and including a possible air gap d between the upper plate of the parallel-plate waveguide and the dielectric. The three equations obtained by Poynting's theorem are described as follows [105]:

$$P_{ref} = \frac{(a_2 + 1)^2 (a_2 - a_1)^2}{(a_2 - 1)^2 (a_2 + a_1)^2} \cdot \exp\left(-\frac{4a_2}{\pi} \int_0^1 \frac{\Omega(x)}{1 + s'^2 - x^2} dx\right) \tag{3.2.3}$$

$$P_{trans} = \frac{4(a_1 - 1)(a_2 + a_1)a_2 a_1 \operatorname{sech}^2(k_0 ds')}{s(a_2 - 1)(a_2 + a_1)^2 (1 + \tanh(k_0 ds))^2}$$

$$\cdot \exp\left(2k_0 ds - \frac{a_2}{a_1}ln\left(\frac{a_1+1}{a_1-1}\right) - \frac{2}{\pi}\int_0^1 \frac{a_2}{a_2{}^2-x^2} - \frac{a_1}{a_1^2-x^2}\Omega(x)dx\right) \quad (3.2.4)$$

$$P_{rad} = \frac{2a_2(a_2+1)(s'-s)^2(1+\sin\varphi)(s^2+\cos^2\varphi)}{\pi(a_2-1)(a_2+a_1)^2(a_1+\sin\varphi)^2(s'^2+\cos^2\varphi)}$$

$$\cdot \frac{\left|\tan(k_0 d\cos\varphi) + \dfrac{\sqrt{\varepsilon_r-\sin^2\varphi}}{\varepsilon_r\cos\varphi}\tan(k_0 h\sqrt{\varepsilon_r-\sin^2\varphi})\right|}{|\mathrm{sech}(k_0 d\cos\varphi)|\sqrt{1+\dfrac{\varepsilon_r-\sin^2\varphi}{(\varepsilon_r\cos\varphi)^2}\tan^2(k_0 h\sqrt{\varepsilon_r-\sin^2\varphi})}}$$

$$\cdot \exp\left(-\frac{2a_2}{\pi}\int_0^1 \frac{1}{a_2{}^2-x^2}\Omega(x)dx + \frac{2\sin\varphi}{\pi}\wp\int_0^1 \frac{\frac{\pi}{2}-\Omega(x)}{\sin^2\phi_0-x^2}dx\right) \quad (3.2.5)$$

$$\Omega(x) = k_0 d\sqrt{1-x^2} + \arctan\left(\frac{\sqrt{\varepsilon_r-x^2}}{\varepsilon_r\sqrt{1-x^2}}\tan(k_0 h\sqrt{\varepsilon_r-x^2})\right) \quad (3.2.6)$$

where x is the variable that represents the path of integration limited between 0 and 1, φ is the angle of radiation defined by $\varphi = 2\arctan(a_1 - s)$, r' and s' are the absolute value of the normalised wavenumbers with respect to the free-space wavenumber of the incident mode in the dielectric $|k_{z_{diel}}/k_0|$ and in the air $|k_{z_{air}}/k_0|$ respectively and a_1 and a_2 are two variables defined for convenience by:

$$a_1 = \sqrt{1+s^2} \quad (3.2.7)$$

$$a_2 = \sqrt{1+s'^2} \quad (3.2.8)$$

being s the absolute value of the normalised wavenumber in the air with respect to the wavenumber for the lowest TM_0 mode in the dielectric $|k_{z_{air}}/k|$, with $k = k_0/\sqrt{\varepsilon_r}$. These wavenumbers are calculated by [102]:

$$r'^2 + s'^2 = \varepsilon_r - 1 \quad (3.2.9)$$

$$\varepsilon_r s' = r'\tan(k_0 h r') \quad (3.2.10)$$

and represented in Fig. 3.3.
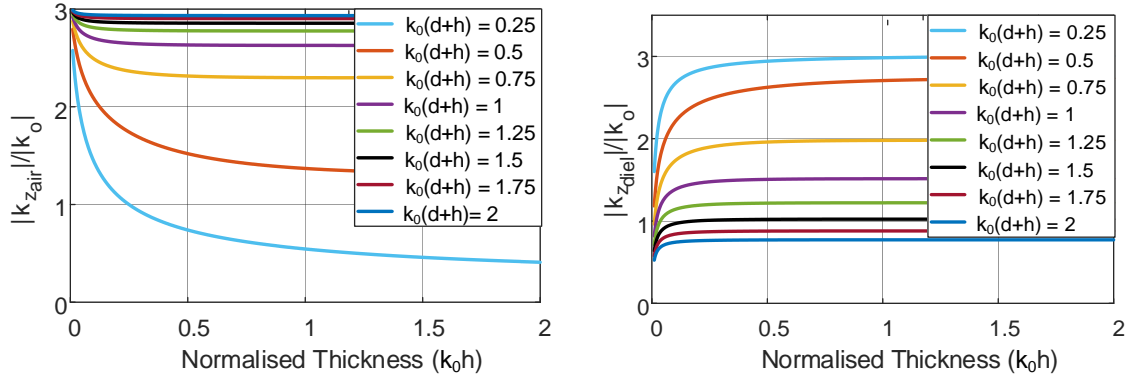
Figure 3.3: Plot of the normalised wavenumbers with respect to the free-space wavenumber of the incident mode in the air and in the dielectric for a relative permittivity of 10.2 for different thickness h and air gap variations d.
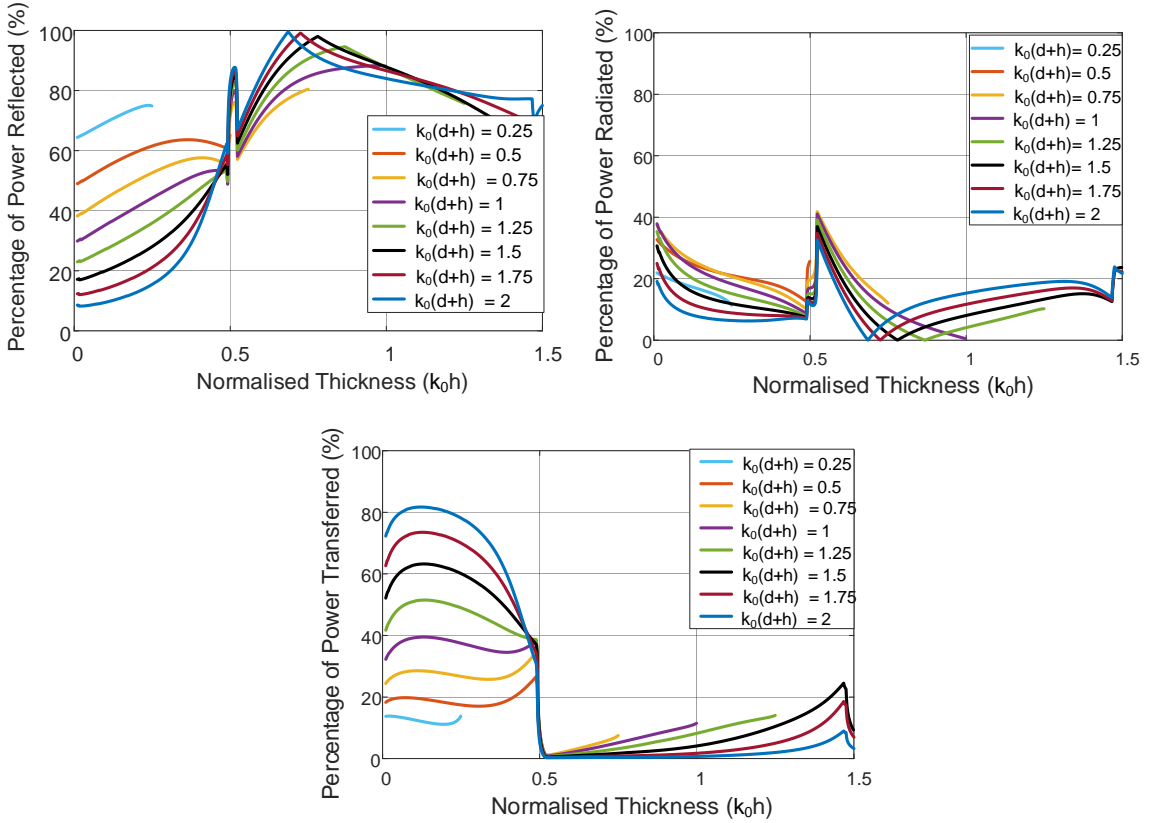
Figure 3.4: Plots of the percentage of power reflected, radiated and transferred for the TM_0 mode at the truncation of the parallel-plate waveguide for different normalised thickness h and air gaps d.

These curves are calculated for a relative permittivity of $\varepsilon_r = 10.2$. As depicted in Fig. 3.4, for normalised thickness as ≥ 0.50, the unimodal condition is no longer preserved and the performance of the system is highly compromised, limiting the bandwidth of the grounded dielectric slab.

To avoid this narrowband performance, a rectangular grounded dielectric slab is used instead (see Fig. 3.1), which allows for mode confinement in two-dimmensions (2D), not only 1D as for the grounded dielectric slab case [119]. Therefore, the width of the rectangular grounded dielectric slab W becomes critical for unimodal propagation in a wider bandwidth, as if too large it can excite higher order modes. These guides support hybrid modes as there are always spurious fields in the orthogonal components to the most significant ones and they are classified as E_{mn}^z (TM-to-z) and E_{mn}^x (transverse electric (TE)-to-x). E_{11}^z and E_{11}^x are the fundamental modes with main transverse field components E_z and H_x for the E_{mn}^z and E_x and H_z for the E_{mn}^x modes respectively [119]. Nevertheless, given the presence of the ground plane, the E_{mn}^x modes have their component E_x shorted allowing the suppression of these modes and increasing the frequency bandwidth for unimodal operation [119].

3.3 Launcher Design, Simulated Results and Discussions

Following the trade-off between high launching efficiency and substrate availability, the selected material has been the ROGERS 6010LM with a relative permittivity ε_r of 10.2. The width W has been set as 3.25 mm and a thickness h of 1.90 mm to operate at K and K_a bands. Once these parameters are set, the transition has been designed for a 50.00 Ω microstrip line with a width W_m of 1.50 mm connected to the parallel-plate waveguide of width W (see Fig. 3.1).

In order to confirm unimodal propagation expected from theory for the selected material and parameters, the phase constant β_x for the designed structure is calculated with CST [12] and plotted in Fig. 3.5. It can be observed how higher order modes start to propagate above 25.00 GHz. In fact, when including the parallel-plate waveguide and the microstrip line, these higher order modes do not significantly alter the performance until 30.00 GHz. As depicted in Fig. 3.6 for an end-to-end configuration, the $|S_{11}|$ and the $|S_{21}|$ for these modes are below -40.00 dB suggesting unimodal E_{11}^z surface-wave excitation.

The matching section, consisting of a subwavelength array of square metallic patches, improves the launching efficiency being a smooth transition between the truncation of the parallel-plate waveguide and the rectangular grounded dielectric slab [118].
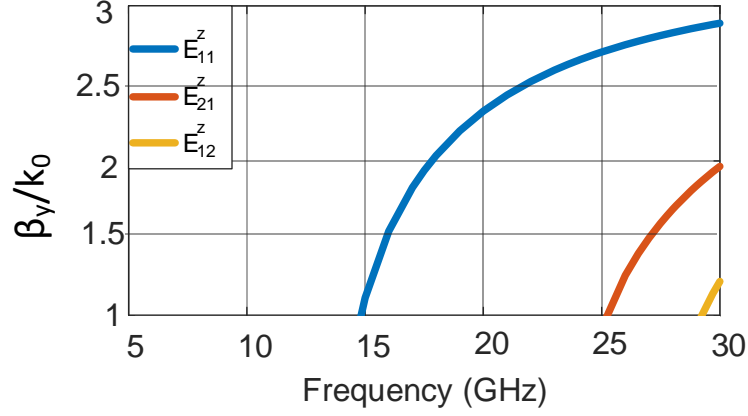
Figure 3.5: Plot of the normalised phase constant for the designed rectangular grounded dielectric slab.
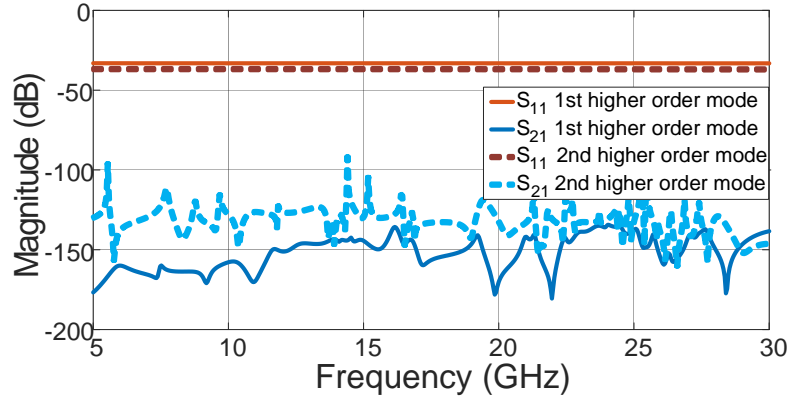
Figure 3.6: Plot of the S-parameters of the higher order modes E_{21}^z and E_{12}^z.

This section has two parameters, the distance D from patch to patch and the gap G between them. The reason why this is considered a sub-wavelength array is because the distance D is more than four times smaller than the free-space wavelength [120]. The surface grid impedance, Z_g, related to the alteration of the gap G between the patches allows the phase constant β of the TM_0 surface-wave mode to be tailored and controlled [118, 120]. In addition, it can be calculated establishing a relation between the gap G and the period of the array of patches D as $G/D = 0.10$. Then parameters can be found using the following equations [118, 120] together with full-wave simulations to calculate the needed grid impedance:

$$Z_g = -j\frac{\eta_{eff}}{2\gamma} \tag{3.3.1}$$

$$\gamma = \frac{k_1 D}{\pi} ln \frac{1}{\sin(\frac{\pi G}{2D})} \tag{3.3.2}$$

where Z_g is the surface grid impedance and $k_1 = k_o\sqrt{\varepsilon_r}$, the effective impedance $\eta_{eff} = \sqrt{\mu_o/(\varepsilon_o\varepsilon_{eff})}$ and the relative effective permittivity $\varepsilon_{eff} = (\varepsilon_r + 1)/2$.

The size of the matching section is a multiple of $\lambda_g/4$, being λ_g the guided wavelength in the dielectric defined as $\lambda_g = \lambda_0/\sqrt{\varepsilon_r}$. The total length of the matching section is $2.96\,\mathrm{mm}$, the distance D between the patches $0.76\,\mathrm{mm}$ and the gap G $0.076\,\mathrm{mm}$.

Different practical design examples with these parameters have been simulated and are described in the following subsections.

3.3.1   End-to-End Structure using Two Launchers

The proposed feeding network has been simulated in an end-to-end configuration, see Fig. 3.2(a), consisting of two launchers facing each other and separated by a distance of $5\lambda_g$ ($d = 20.00\,\mathrm{mm}$). In this way, losses along the dielectric and the transmitted power levels that would go from one port to another in a guiding structure can be understood.

Simulations results in CST [12] of the S-parameters are depicted in Fig. 3.7, where it can be observed that the reflection coefficient is below -10.00 dB from 20.00 GHz onwards, with values slightly above -10.00 dB from 17.00 GHz. Transmitted power levels are around -1.30 dB from 17.00 GHz to 27.00 GHz, which implies 0.65 dB of insertion losses per launcher. These losses are mainly due to the small amount of power being radiated on the parallel-plate waveguide borders as predicted by the design curves in Fig. 3.4. Simulated E-field distributions for different frequencies are also represented in Fig. 3.8, showing uniform E_{11}^z propagation. In addition, normalised E_{11}^z field components are depicted in Fig. 3.9, confirming fundamental mode excitation with the main components as E_z and H_x, while as a consequence of its hybrid nature, spurious components can also be found in the y direction for the electric and magnetic components.

3.3.2   Leaky-wave Antenna Design

An array of 17 printed patch elements have been placed on the rectangular grounded dielectric slab section [88] to study the usefulness of this surface-wave feeding network for a 1D leaky-wave antenna (see Fig. 3.2 (b)). The antenna has been designed to operate in a frequency range from 19.00 GHz to 28.00 GHz with parameters set as following: the patch width is the same as the parallel-plate waveguide, the length D_{LW} is $3.50\,\mathrm{mm}$ and the space S between them is set to be $1.25\,\mathrm{mm}$. The reflection
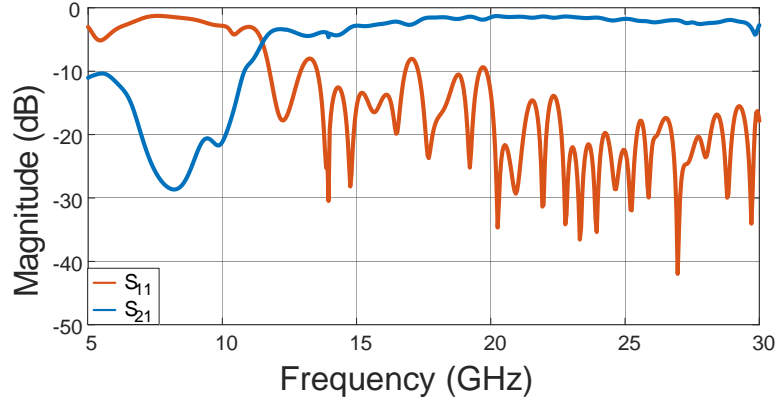
Figure 3.7: Plot of the S-parameters simulation results obtained with CST [12] for the proposed structure in Fig. 3.2(a).
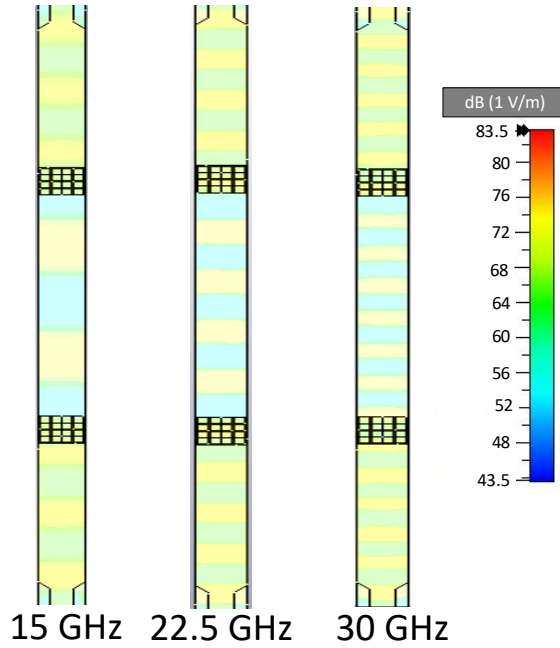
Figure 3.8: Time snapshot of the simulated E^z_{11} electric fields for different frequencies simulated in CST [12].

coefficient, which is shown in Fig. 3.10, is below -10.00 dB from 19.00 to 28.00 GHz except in the open stopband region (Section 2.2, Chapter 2) at broadside [113, 121] which is around 22.50 GHz. The beamwidth, realised gain and pointing angle with respect to frequency are depicted in Fig. 3.12 and the beam steering capability is depicted in Fig. 3.11. It can be observed in these two figures that the main beam scans from -50.00° to 50.00° with gain values about 11.00 dBi and 5.00 dBi in the stopband region at broadside, respectively. Once the leakage rate has decreased significantly above 25.00 GHz, the gain is reduced for higher frequencies as the contribution to the radiated fields from the leaky-wave diminishes. To avoid this, the leakage rate

could be tapered allowing for controlled radiation and power distribution.

These results show the wideband operation of the surface-wave launcher and its good performance in a 1D leaky-wave antenna design which obtains wide beam scanning.

3.3.3 Dielectric Image Guide Feeder

This launcher, when applied to dielectric image guides, has a very good performance in a wide range of frequencies obtaining low level reflections below -10.00 dB and a transmission coefficient around -1.50 dB from about 20.00 GHz onwards with acceptable levels slightly above -10.00 dB from 17.00 GHz (see Fig. 3.13).

This allows for planar and fully integrated implementations while keeping efficient surface-wave excitation. A comparison between the performance of the proposed launcher in a dielectric image guide configuration and the structures that can be
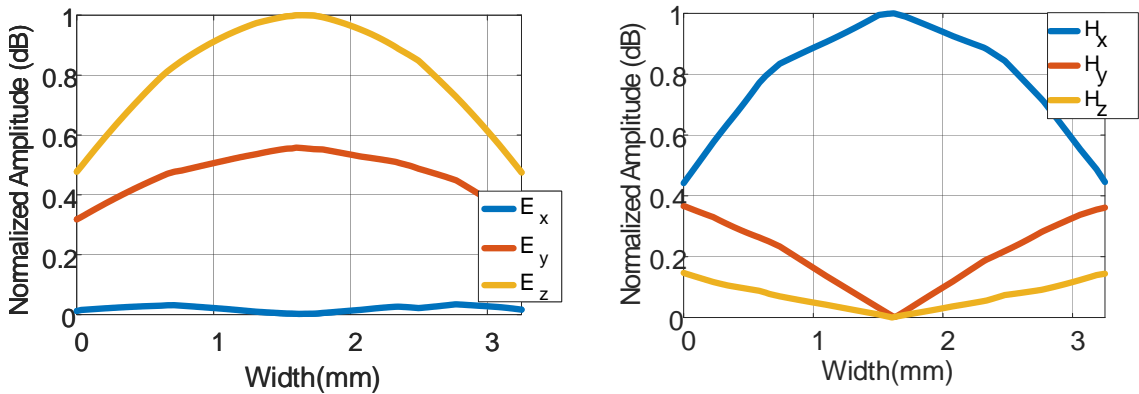
Figure 3.9: Plot of the simulated and normalised E_{11}^z mode amplitude values for the electric and magnetic components in the structure obtained with CST [12].
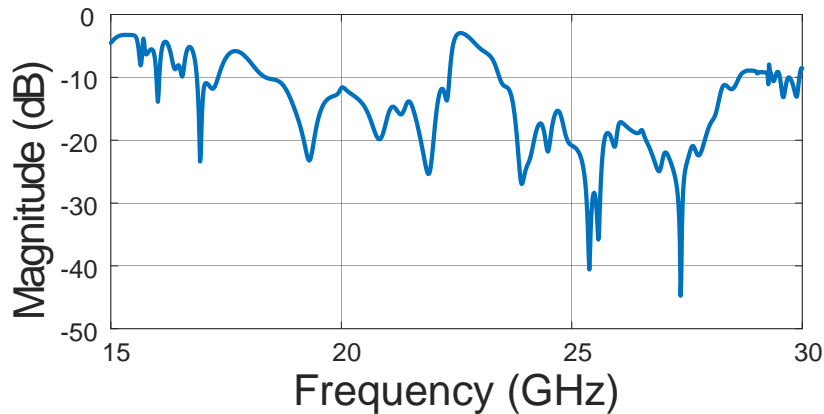
Figure 3.10: Plot of the simulated reflection coefficient for the leaky-wave antenna (see Fig. 3.2(b)) fed by the surface-wave launcher obtained with CST [12].
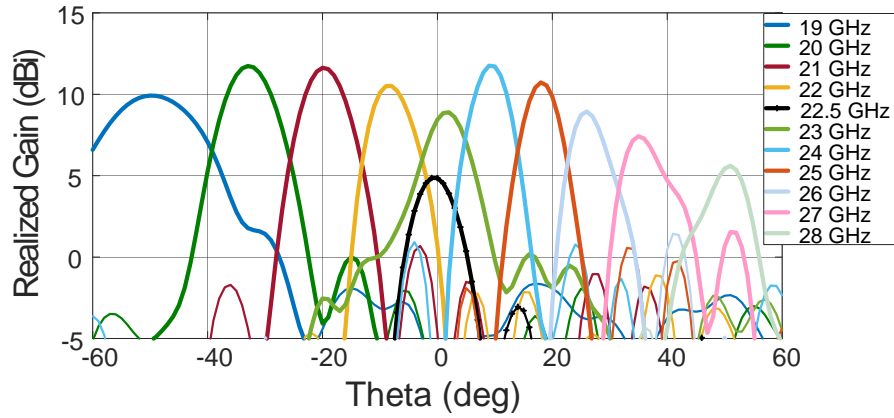
Figure 3.11: Plot of the simulated beam scanning behaviour for the proposed leaky-wave antenna in CST [12]. Each frequency sample from 19.00 GHz to 28.00 GHz is plotted in a different colour.
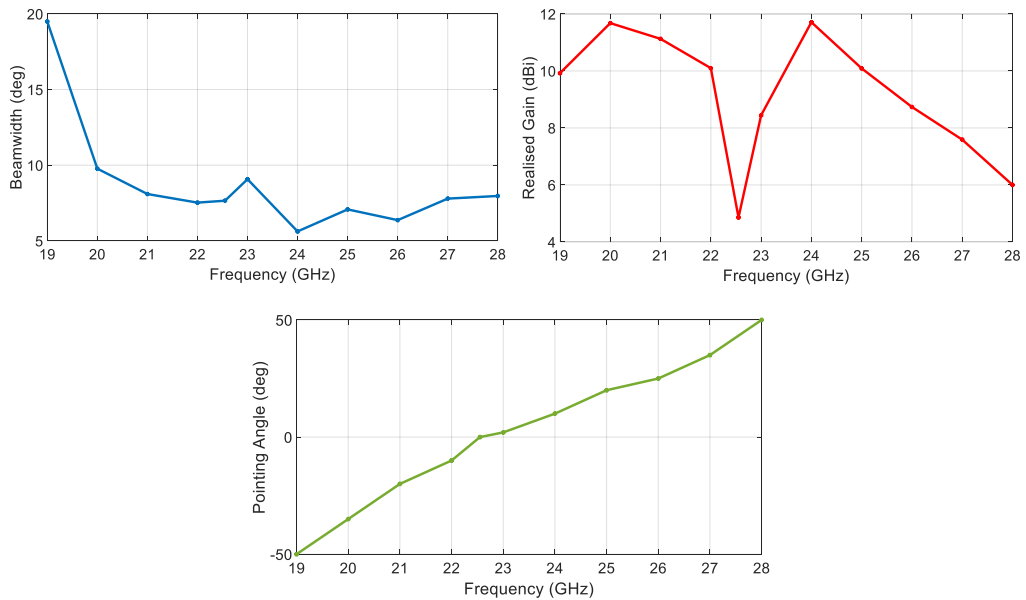
Figure 3.12: Plot of the simulated beamwidth (blue), realised gain (red) and pointing angle (green).

found in the literature is reported in Table 3.3. It is shown that this structure is fully integrated, more compact, with a wider bandwidth of 74.29% and with low insertion losses around 0.65 dB when compared to other feeding networks. This work presents an increased bandwidth of 37.87% with respect to [79] and 90.50% with respect to [81]. This feeding network has a reduced volume of more than 98.66% when compared with [79] and a 44.53% with [81], which demonstrates a more compact approach. Moreover, it provides full integration at the expense of sacrificing efficiency when compared to [79] as insertion losses are around 0.65 dB, which implies an increment of 23.07% with respect to [79].
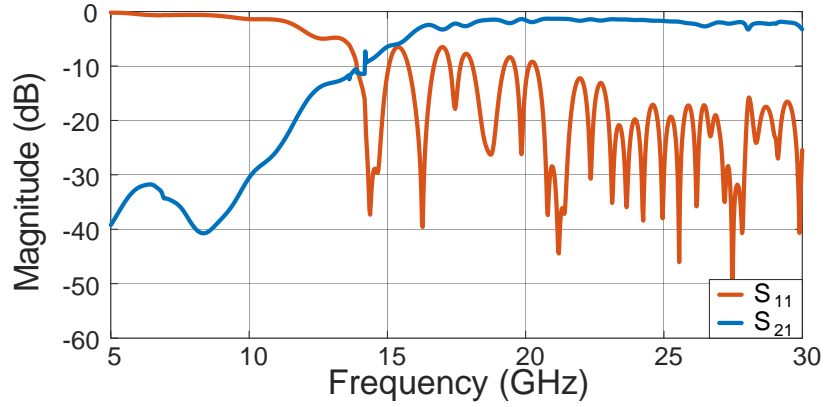
Figure 3.13: Plot of the simulated S-parameters for the dielectric image guide system as illustrated in Fig. 3.2(c).

3.3.4 Substrate Integrated Image Guide Launcher

The proposed feeding network can be also applied to SIIG structures that are becoming popular at microwave and millimetre-wave frequencies giving their field confining characteristics [63]. Air holes are drilled around the wave-guiding channel modifying the effective permittivity ε_{eff}. This value should be close to unity to improve the internal reflection of the modes [63], as depicted in Figs. 3.2 (d) and 3.14. The diameter D of these holes is calculated setting a desired effective permittivity following [63, 122]:

$$\varepsilon_{eff} = \varepsilon_r - \frac{D^2 \pi}{4 p^2 \sin(\pi/3)}(\varepsilon_r - 1) \ . \tag{3.3.3}$$

In this case, small air holes have also been included to improve mode confinement at lower frequencies. The value of these diameters is found by full-wave optimisations with CST [12]. The parameters set for this configuration are the following: $D = 2.00\,\mathrm{mm}$, $d_1 = 0.75\,\mathrm{mm}$, $d_2 = 0.50\,\mathrm{mm}$, $p = 2.20\,\mathrm{mm}$ and $\varepsilon_{eff} = 1.00$. Simulated results and E-field propagation are depicted in Figs. 3.15 and 3.16. Values below -10.00 dB for reflection coefficient are obtained from 21.00 GHz to 27.00 GHz, while the transmission coefficient is around -2.00 dB 17.00 GHz up to 27.00 GHz. Without

Table 3.3: Launcher Performance Simulation Results Comparison for Dielectric Image Guide

	Insertion Losses (dB)	Impedance Bandwidth (%)	Surface-wave Excitation Method	Input Technology	Size $(W/\lambda_0 \mathrm{x} L/\lambda_0 \mathrm{x} H/\lambda_0)$	Integration
[79]	0.50	46.16	Horn Waveguide	Waveguide	$0.77\lambda_0\mathrm{x}3.30\lambda_0\mathrm{x}0.71\lambda_0$	Attached
[80]	0.75	32.30	Flared dielectric	Microstrip	$0.38\lambda_0\mathrm{x}1.44\lambda_0\mathrm{x}0.13\lambda_0$	Attached
[81]	-	7.06	Slot array	Microstrip	$1.52\lambda_0\mathrm{x}0.18\lambda_0\mathrm{x}0.16\lambda_0$	Attached
This work	**0.65**	**74.29**	**Truncated parallel-plate waveguide**	**Microstrip**	$\mathbf{0.20\lambda_0\mathrm{x}1.01\lambda_0\mathrm{x}0.12\lambda_0}$	**Fully integrated**

Table 3.4: Launcher Performance Simulation Results Comparison for SIIG

	Insertion Losses (dB)	Impedance Bandwidth (%)	Surface-wave Excitation Method	Input Technology	Size (W/λ_0xL/λ_0xH/λ_0)	Integration
[83]	0.74	25.8	SIW horn	Coplanar	$1.18\lambda_0$x$2.25\lambda_0$x$0.16\lambda_0$	Attached
[122]	0.5	27.02	Slot dipoles	Coplanar	$0.52\lambda_0$x$0.2\lambda_0$x$0.12\lambda_0$	Fully integrated
[123]	0.5	46.16	Dielectric rod	Horn waveguide	$0.77\lambda_0$x$3.3\lambda_0$x$0.71\lambda_0$	Attached
This work	**1.25**	**50.00**	**Truncated parallel-plate waveguide**	**Microstrip**	$\mathbf{0.2\lambda_0}$**x**$\mathbf{1.01\lambda_0}$**x**$\mathbf{0.12\lambda_0}$	**Fully integrated**

matching section, the impedance bandwidth is reduced and the performance is worse for the central frequency range (20.00-25.00 GHz) with a decrement of transmission coefficient values around 0.50 dB. Moreover, uniform propagation is also obtained, confirming the good wave confinement by the air hole lattice.

This launcher, improves the state-of-the-art for the SIIG feeding networks achieving compact, fully planar and integrated launcher for microwave frequencies avoiding the use of complex multilayer structures or bulky metallic horn feeds causing unwanted radiation and reflections at discontinuities. A comparison between the performance of the proposed launcher in a SIIG configuration and the structures that can be found in the literature is reported in Table 3.4. This work presents an improved bandwidth of 50.00%, which is an increment of 7.63% with respect to [123] and 48.40% with respect to [83]. This feeding network has a reduced volume of more than 95.30% when compared with [83] and a 98.66% with [123], which demonstrates that is a more compact approach. Moreover, it provides full integration at the expense of efficiency when compared to other systems as insertion losses are around 1.25 dB, which presents an increment of 60.00% when compared to [122, 123].
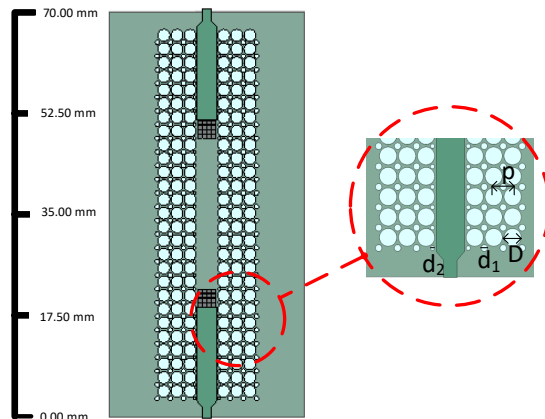
Figure 3.14: Diagram of the SIIG structure for the E_{11}^z excitation fed by two microstrip lines.
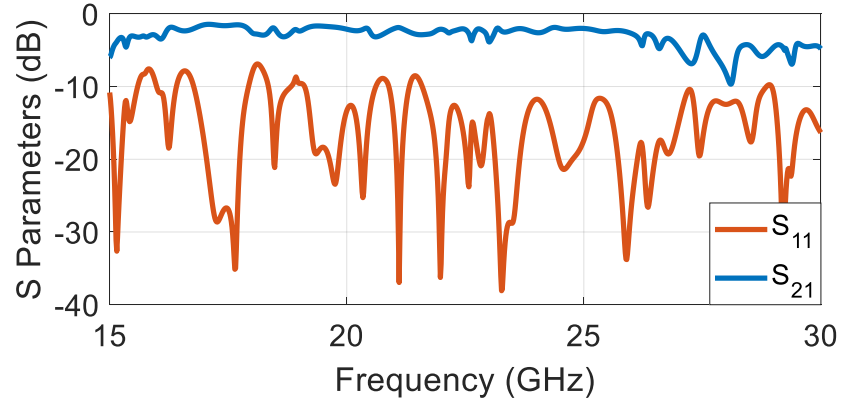
Figure 3.15: Plot of the simulated S-parameters for the SIIG system with the matching section obtained in CST [12].
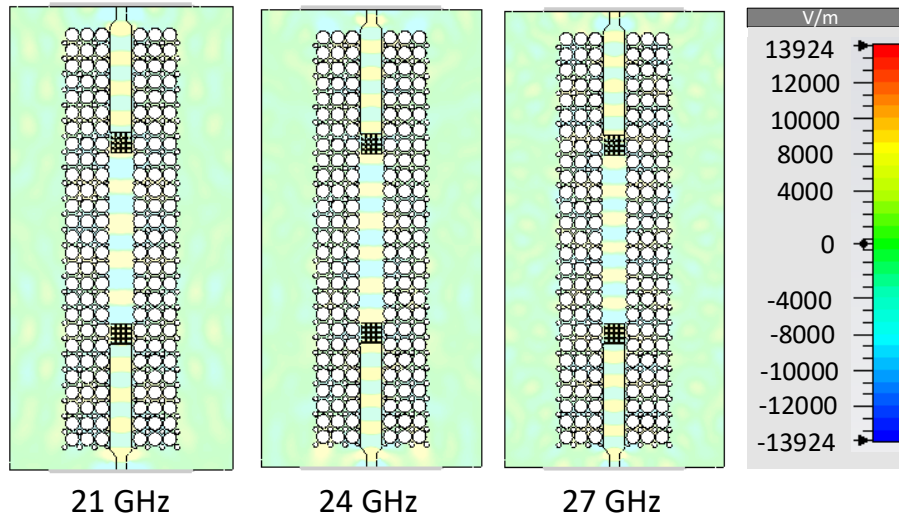
Figure 3.16: Time snapshot of the simulated E_{11}^z electric field at different frequencies.

3.4 Feeding Networks

The main concern raised during the design of this surface-wave launcher is the use of appropriate connectors that perform efficiently for this relative permittivity, thickness and frequency. While 2.92 mm or 2.40 mm connectors are widely used for K and Ka bands, it has been found that they become problematic when attached to thick high relative permittivity dielectrics as shown in Fig. 3.17, where the simulated S-parameters of the SIIG structure with a 2.40 mm connector are illustrated. The performance of the launcher is significantly compromised causing high reflections and negligible transmitted power levels.

Two end-launch 2.40 mm connectors are simulated and attached to a simple 50.00 Ω
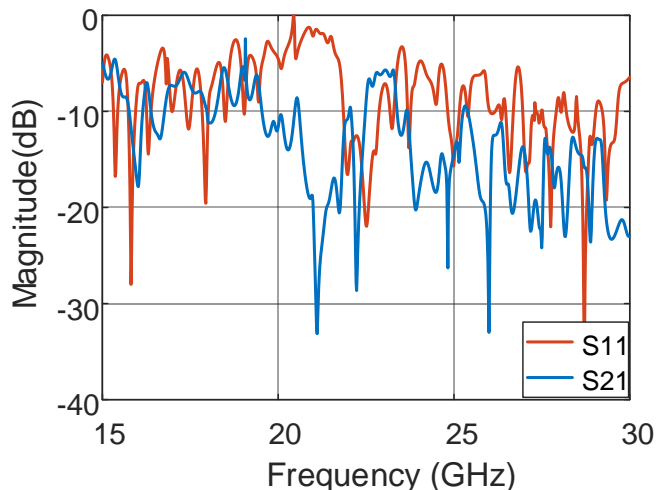
Figure 3.17: Plot of the simulated S-parameters for the SIIG system feed by a microstrip line and 2.40 mm connector in CST [12].

microstrip line with PEC conductor and lossless dielectric to better isolate the losses caused by the connectors. This is depicted in Fig. 3.18, where it can be observed how the increment in thickness for a 10.2 relative dielectric permittivity affects the performance of these connectors after 15.00 GHz. For a thin substrate, i.e., 0.653 mm thickness, the reflection coefficient is below -10.00 dB for the whole frequency range with transmission levels of -0.20 dB. When using thicker substrates around 1.27 mm, reflection levels are below -10.00 dB and transmission levels above -3.00 dB up to 20.00 GHz. For the case of this launcher, the use of a 1.91 mm thickness material implies a maximum frequency of operation for the connectors of 15.00 GHz as reflections become extremely high with poor transmission levels. However, the possibility of using thinner substrates is automatically rejected as it would significantly alter the surface-wave launcher performance exciting higher order modes, as demonstrated in Section 3.2.

In order to solve this problem, de-embedding connector S-parameters from measurements results may be an interesting option. Nevertheless, given the small size of the structure, fringing fields couple into the system invalidating the lumped equivalent circuit approach needed to model the connectors for de-embedding [124].

Given the issues to use radio frequency (RF) end-launch connectors for our microstrip input, an alternative feeding network has been designed. It consists of the use of a coaxial probe, connected $\lambda_g/4$ away from a non-leaky wall made of metallic
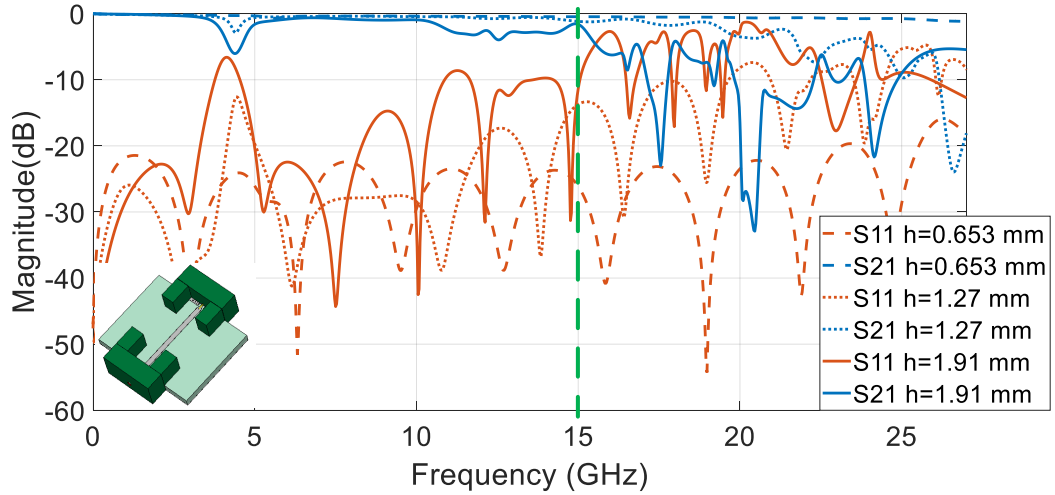
Figure 3.18: Plot of the simulated S-parameters comparison for the different dielectric thickness with 10.2 relative permittivity for the structure depicted in the left bottom corner. Dashed green line represents the lowest frequency of operation for the surface-wave launcher. Solid lines represent the S-parameters for the thickness $h = 1.91$ mm used for the surface-wave launcher design, dotted lines for a thinner substrate $h = 1.27$ mm and dashed lines for $h = 0.653$ mm.

vias surrounding the probe for an increased matching bandwidth [125]. Nevertheless, this feed system reduces considerably the bandwidth but allows good transmission power levels in comparison to connectors attached to the microstrip, as depicted in Fig. 3.19. The S-parameters for the SIIG structure fed by a coaxial probe with via diameter of $d_v = 0.20$ mm and pitch $p = 0.30$ mm are presented in Fig. 3.19. It can also be observed how the bandwidth has been significantly reduced but still the performance is satisfactory from 24.00 GHz to 27.00 GHz with reflection levels below -10.00 dB while transmission power values are about -2.50 dB.

The SIIG launcher with the probe configuration was manufactured industrially given the small tolerances required for etching (microstrip gaps below > 0.10 mm). The prototype is depicted in Fig. 3.20 together with the measured results of the S-parameters using a 2-ports network analyser. As it can be observed transmission levels reach a maximum of -7.00 dB during the low reflection $(< -10.00$ dB$)$ region from 26.00 to 27.00 GHz. These results are in disagreement with simulated S-parameters depicted in Fig. 3.19. The reason behind this unexpected performance can be a possible small air gap due to drilling processes for the probe. As illustrated in Fig. 3.21, the probe is introduced up to a certain depth in the substrate material (0.80 mm). When drilling this cavity for the probe, a small air gap could have been created between the probe and the end of the cavity (see Fig. 3.21

49
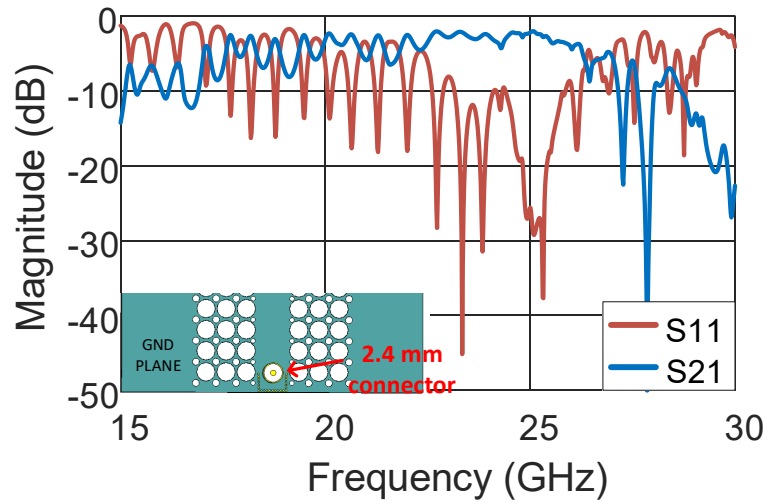
Figure 3.19: Plot of the simulated S-parameters for the SIIG system fed by a coaxial probe shown in the left bottom corner obtained with CST [12].
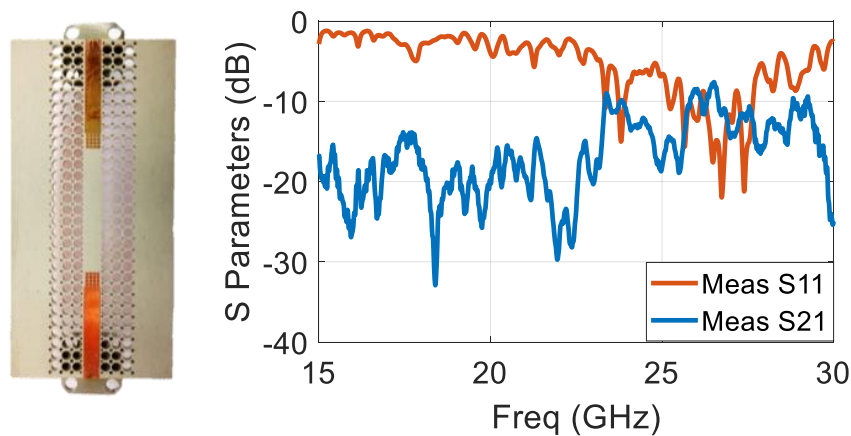
Figure 3.20: Photograph of the manufactured SIIG launcher (left) and the plot of the measured S-parameters (right).

(left)) due to the non-planar shape of the drill bit. To test this possibility, an air gap has been simulated in the probe cavity and its relative permittivity has been varied from 1 (air) to 9 (close to substrate permittivity as 10.2 results are already depicted in Fig. 3.19). It can be observed how the simulated S-parameters are in better agreement with measurements for lower permittivities, causing high reflections and low transmission power levels around -7.00 dB at 27.00 GHz. This behaviour is expected given the high difference between dielectric and air relative permittivities, which causes the wave to be reflected back to the source.
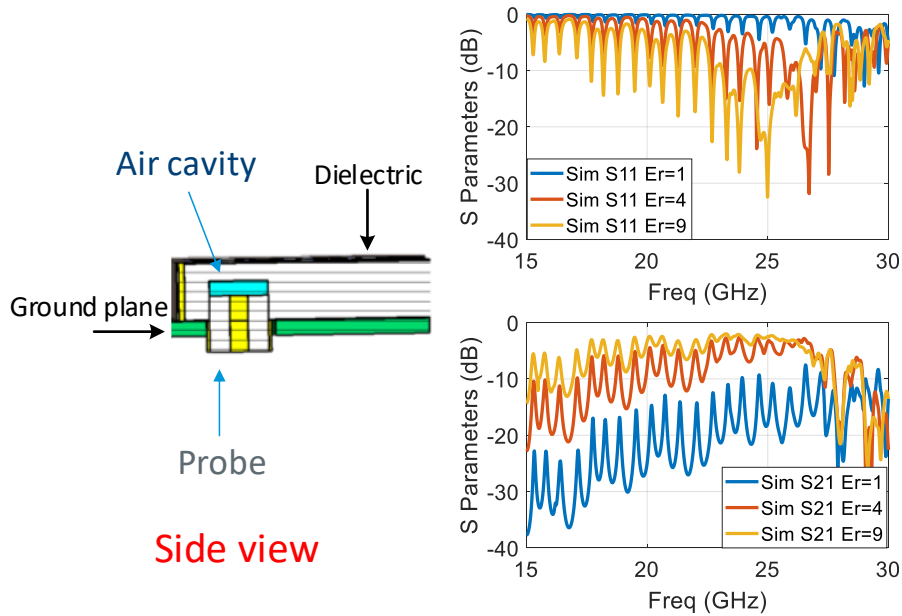
Figure 3.21: Diagram for the probe implementation in CST [12] (left) and plot of the simulated S-parameters for the different relative permittivities (right) to show the effects on the structure of a possible air cavity.

3.5   Summary

A wideband, low profile and fully planar feeding network has been proposed in this chapter. It has been shown how by the truncation of a parallel-plate waveguide on a grounded dielectric slab surface-waves can be efficiently excited (>80.00%). The launcher employs common grounded dielectric slab and surface-wave theory to find the needed design parameters and it consists of a microstrip to parallel-plate transition, parallel-plate waveguide and a subwavelength matching section. This feeding network has been designed for a rectangular grounded dielectric slab, dielectric image guide and SIIG as a proof of concept.

Simulation results show wideband behaviour improving more conventional surface-wave feeding found in the literature. It is shown that this work presents an increased bandwidth of 37.87% with respect to [79] and 90.50% with respect to [81] and a reduced volume of more than 98.66% when compared with [79] and a 44.53% with [81], which demonstrates that is a more compact approach. Moreover, it provides full integration at expense of sacrificing efficiency as insertion losses are around 0.65 dB, which implies an increment of 23.07% with respect to [79].

This feeder can also be easily applied to SIIG technology maintaining high efficiency and compactness. It can be seen how this work presents an improved bandwidth of

50.00%, which is an increment of 7.63% with respect to [123] and 48.40% with respect to [83]. This feeding network has a reduced volume of more than 95.30% when compared with [83] and a 98.66% with [123]. Moreover, it provides full integration sacrificing efficiency when compared to other systems as insertion losses present an increment of 60.00% if compared to [122, 123]. As an alternative, SIW horn antenna [126] instead of a parallel-plate waveguide could also be used. However, it would sacrifice launching efficiency given the constraints introduced by the aperture angle to maintain the unimodal excitation.

Special attention should be given to the feeding network for thick and high relative permittivity dielectrics, since the performance of the system is affected by the attachment of RF connectors to the microstrip line. An alternative feeding approach is designed by using probes which might be preferred although the frequency bandwidth may be limited.

Chapter 4

Leaky-wave Theory Applied to New Planar Feeding Systems

4.1 Introduction

In this chapter leaky-waves are used to excite other leaky-wave antennas instead of surface-waves as presented in Chapter 3. A compact, simple and low-cost configuration for transverse electromagnetic (TEM) launching into a parallel-plate waveguide by suitably and originally combining substrate integrated waveguide (SIW) technology and leaky-wave theory whilst operating close to the splitting beam point for the structure is presented, see Fig. 4.1. This enables simple and compact uniform wavefront formation into the parallel-plate waveguide.

Unlike [6] and [92], where a cylindrical-wave was generated, our proposed feed arrangement can achieve a uniform planar wavefront with a direction of propagation perpendicular to one sidewall of the SIW. This launcher is simply fed by a single input $50.00\,\Omega$ microstrip line and defines a single-layer implementation for slot arrays and other planar parallel-plate waveguide feed systems. The proposed feeding network consists of conventional microwave elements such as a T-junction in SIW technology, where one sparse via wall acts as a partially reflective surface [6, 92, 127] for power leakage, avoiding the use of other mechanisms, such as reflectors, to obtain a planar TEM wavefront in parallel-plate waveguide.

The proposed planar parallel-plate waveguide launcher has also additional applications as an end-fire antenna or as the feeding network to other parallel-plate based
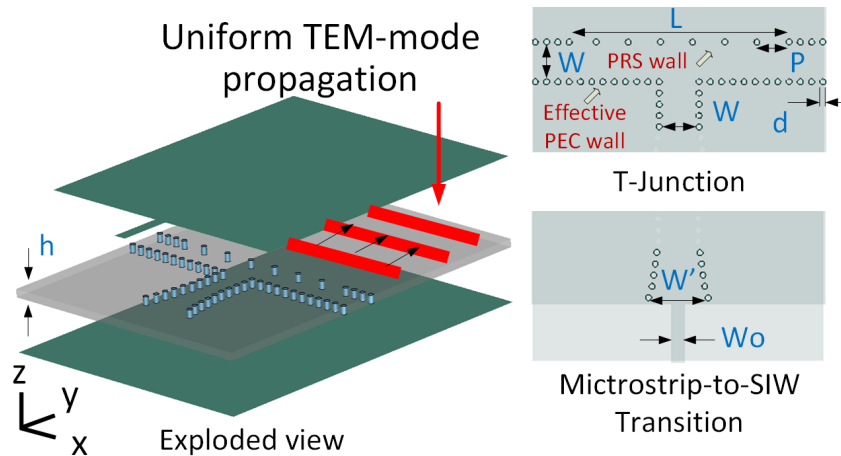
Figure 4.1: Schematic for the proposed parallel-plate waveguide TEM mode launcher consisting of the microstrip-to-SIW transition, an SIW T-junction with one sparse row of vias defining a partially reflective surface, and the parallel-plate waveguide region [From [128] © 2019 IEEE].

guides, new low-cost transitions, and compact dividing/combining circuits. Furthermore, if the parallel-plate waveguide is truncated after the partially reflective surface aperture, this structure can efficiently work as a surface-wave launcher exciting the fundamental transverse magnetic (TM_0) mode of the grounded dielectric slab. This represents an interesting alternative to feed, for example, planar leaky-wave antennas in grounded dielectric slab since it can be challenging in terms of design size and simplicity at microwave and millimetre-wave frequencies. Therefore, the proposed structure could also be used to avoid the problems caused by surface-wave launchers implemented on the ground plane, as explained in Chapter 2, while keeping a low profile design simply fed by a $50.00\,\Omega$ microstrip line.

Some initial findings were investigated in [131] but no theoretical analysis or general design guidelines were provided. Furthermore, a thinner substrate for this work is employed while operating at the same frequency, in order to reduce microstrip radiation losses at the input considering microwave and millimetre-wave frequencies. Theoretical approaches as a transverse resonance equation and a Bloch analysis will be developed to accurately analyse the mode propagation and set the parameters needed for the launcher. Full-wave simulation results using the frequency domain solver of CST [12] will be shown to assess and confirm the expected performance. Measurements are reported at $15.00\,\text{GHz}$ for a fabricated two-launcher test circuit prototype, then comparisons to the expected results will be discussed. Moreover, it will also be explained that by the addition of the matching network used in Chapter

3, this structure could be implemented as a surface-wave launcher itself, as well as an end-fire antenna as additional applications.

4.2 Substrate Integrated Waveguide Overview

SIW structures are defined by their width W, the pitch P and their diameter d (see Fig. 4.1). One perhaps unwanted feature of SIW structures is their predisposition to generate leakage losses into the substrate due to the practical separation of the vias P. These losses can be negligible if the ratio between the via post separation P and their diameter d is small enough ($P/d < 2$) [54], hence a wall of dense vias can act as perfect electric conductor (PEC). Otherwise, a fraction of the power will be leaked and the losses will become significant, and the wall of vias will behave as a partially reflective surface [129]. More specifically, if P is large enough, it can allow the conversion of part of the propagating wave inside the SIW into the TEM parallel-plate waveguide modes. This characteristic can be useful when implementing efficient planar leaky-wave antennas in SIW by controlling these two parameters, as shown for example in [56].

According to these restrictions, the following rules can be considered in order to reduce these losses keeping radiation at a minimum level in an SIW system [130]:

$$d < \frac{\lambda_g}{5} \tag{4.2.1}$$

$$P \leq 2d \tag{4.2.2}$$

The dispersion characteristics of the SIW when non-leaky conditions are satisfied are the same as for rectangular waveguides. Therefore, equations defined to obtain the width W are related to the equivalent width of a rectangular waveguide at the same frequency of operation and the ratio P/d, as explained in [54]. Although these equations provide a good approximation for the design of SIW structures, they still lack the flexibility for non-standard relations of P/d. Thus, as explained in following sections, a valid solution for this problem is to perform a full-wave analysis in order to get an accurate estimation of the propagation constant in a wide range of values of P/d.

The dispersion characteristics of the SIW and rectangular waveguides are very similar as proved in [54]. Therefore, the width W of an SIW determines its cutoff

frequency and it can be calculated from the width W_{WG} needed in a rectangular waveguide [54]:

$$f_{TE_{10}} = (2W_{WG}\sqrt{\mu_0\mu_r\varepsilon_0\varepsilon_r})^{-1} \tag{4.2.3}$$

$$f_{TE_{20}} = 2f_{TE_{10}} \tag{4.2.4}$$

with μ_0 and ε_0 being the permeability and permittivity of free-space and μ_r and ε_r of the material, respectively.

Thereby, the SIW width can be found by [54]:

$$W = W_{WG} - 1.08\frac{d^2}{P} + 0.1\frac{d^2}{W_{WG}} \tag{4.2.5}$$

These formulas will be used to calculate the parameters needed for the bounded SIW section, where Eqs. (4.2.1) and (4.2.2) will be set to satisfy the non-leaky condition.

4.3 Parallel-plate Waveguide TEM Mode Launcher

The parallel-plate waveguide TEM launcher has two main components: the well-known microstrip-to-SIW transition and the open T-junction, as shown in Fig. 4.1. In addition, it should be highlighted that the modified SIW section with the sparse via sidewall defining the partially reflective surface supports a perturbed transverse electric (TE_{10}) mode which couples to the TEM mode of the parallel-plate waveguide in the form of a non-radiating leaky-wave for propagation into the parallel-plate waveguide region. Thus, careful modal analysis of the dispersion for this quasi-TE_{10} leaky mode, and its complex wavenumber, is essential for accurate design and for optimum operation of the proposed parallel-plate waveguide launcher in SIW technology.

Due to the application of leaky-wave theory, planar TEM propagation is obtained right after the partially reflective surface via side wall. This avoids the physical space typically required between the input transmission line or feed point and the generated wavefront as in previous designs [5, 6, 92, 93]. In this case, the uniform phase front is formed at the leaky SIW side wall, and, when considering operation at microwave and millimetre-wave frequencies, this can lead to minimal conductor and dielectric losses, mainly due to the compact and efficient nature of the launcher and the generated field profile.

To minimise reflections and radiation losses, a launching efficiency of over 90.00% for the proposed TEM parallel-plate waveguide launcher is set. Therefore, the size of the leaky partially reflective surface aperture is defined to be $2.50\lambda_o$, making the design more compact and efficient when compared to the other previously reported configurations [5,6,92,93]. Also, to achieve leakage normal to this partially reflective surface wall, the complex propagation constant and field profile of the leaky SIW should be accurately characterised and set to be around the beam splitting condition [56,57]. This can provide TEM propagation in the broadside direction with respect to the SIW launcher aperture and with a uniform amplitude and phase field profile (see Fig. 4.1).

4.3.1 T-junction in Substrate Integrated Waveguide

This is the primary component of the launcher and consists of a modified H-plane T-junction power divider for equal power distribution within the parallel-plate waveguide region. This structure is similar to a two-sided periodic structure for leaky-wave radiation into free-space, but designed here for a non-radiating application; i.e. an SIW to parallel-plate waveguide transition and with $50.00\,\Omega$ microstrip feeding. The more conventional design of this T-section structure has been widely explained in the literature, for instance in [102, 132–134]. As mentioned, our design is further based on leaky-wave theory applied to SIW structures [62, 135] and considering optimised broadside leaky-wave radiation from periodic structures [113].

Several guidelines can be defined to successfully design this launcher. The main function of the T-junction is to equally split the power along the aperture, as illustrated in Fig. 4.2. By means of the partially reflective surface wall, the waves will be leaked into the parallel-plate waveguide. The control of its propagation constant with the via diameter, periodicity and width of the SIW section would allow for uniform amplitude and phase distribution of the TEM mode in the parallel-plate waveguide section. Therefore, this partially reflective surface should be initially defined as a non-leaky structure in order to find the SIW T-junction parameters. Depending on the desired frequency of operation the SIW width W can be found following Eq. (4.2.5).

It should be noted that to achieve this uniform propagation, the frequency of operation must be very close to cutoff to work under the beam splitting condition. As

the frequency of operation selected for this structure is 15.00 GHz, it is assumed to be the cutoff frequency that will define the value of W according to Eq. (4.2.5). Knowing W, the design of the bounded section of the SIW becomes straightforward once the ratio P/d is set to accomplish the non-leakage condition and the standard guidelines for power dividers in waveguide technology provided in [102] are followed. Three bounded SIW sections with same parameters are put together in a T shape. It should also be considered that to avoid high reflections at the input port, the addition of an extra inductive post around the middle of the T-junction is necessary [132]. The inductive post diameter d' and position s can significantly affect the level of return losses. Design curves based on numerical analysis, such as finite element or the finite-difference time-domain method, have been proposed in [132]. These curves have been used as a starting point for this T-junction, however, optimal parameters have been refined by the optimization tools provided by CST [12]. Parameters for the non-leaky T-junction are set as follows: $W = 7.80$ mm, $d = 1.00$ mm, $p = 1.92$ mm, $d' = 0.64$ mm and $s = 3.20$ mm (see Fig. 4.2). The leakage rate will influence the efficiency of the launcher. If it is set high enough (80.00%), most of the power will be leaked preventing it to reach the side arms of the T-junction, which would cause spurious radiation at the edges and reflections.
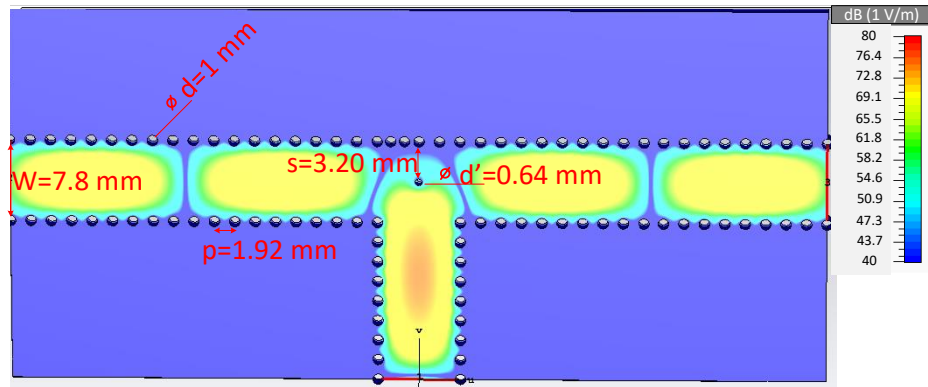
Figure 4.2: Time snapshot of the simulated electric field distribution inside the non-leaky T-junction in SIW technology above 15.00 GHz.

4.3.2 Leaky-wave Theory for Partially Reflective Surface Wall

For the proposed launcher, leakage losses are necessary to couple power into the TEM mode of the parallel-plate waveguide. Thus one of the walls of the T-junction should ensure the vias are separated as to not satisfy the $P/d < 2$ ratio condition [54, 56]. This ensures controlled leakage into the parallel-plate waveguide region as illustrated in Fig. 4.1.

To design this leaky partially reflective surface in SIW technology, several general guidelines are established from previous SIW-based leaky-wave antennas [57]. In particular, to design the partially reflective surface, it is necessary to analyse the complex propagation constant of the relevant leaky-wave mode. The leakage rate α (i.e., the imaginary part of the complex propagation constant) sets the fraction of power that couples into the parallel-plate waveguide TEM mode and it depends on the separation P and the diameter d of the vias. The higher this separation the higher the leakage rate is observed on the opposite side of the SIW-to-parallel-plate waveguide transition. At the same time, the phase constant β (i.e., the real part of the complex propagation constant) establishes the direction of propagation for the TEM mode in the parallel-plate waveguide region [113].

The uniformity of the amplitude and the phase can be obtained by selection of the leaky-wave propagation constant. In particular, broadside leakage from the SIW T-junction into the parallel-plate waveguide region can be achieved by satisfying the so-called beam-splitting condition which is based on having approximately equal phase and leakage constants; i.e., it is necessary to work slightly above the cutoff frequency (where $\beta \approx \alpha$ and with $\beta > \alpha$). Also, the leakage angle θ_{m} (see Fig. 4.3) increases if β increases according to $\theta_{\mathrm{m}} = \sin^{-1}(\sqrt{(\beta/k_0\sqrt{\varepsilon_r})^2 - (\alpha/k_0\sqrt{\varepsilon_r})^2})$ [113]. Thus, if there is an increase in frequency above cutoff, the angle θ_{m} will be larger. The simulated behaviours of the electric fields for the structure for these different variations between β and α are depicted in Fig. 4.4. On top, the frequency of operation is below the cutoff frequency ($\beta < \alpha$); i.e., the TEM mode is not propagating. In the center, the structure is working at the design frequency where $\beta \approx \alpha$. It can be observed that the TEM mode is propagating with a uniform phase front and perpendicular (or broadside) to the leaky SIW sidewall. On the bottom, $\beta > \alpha$, therefore the
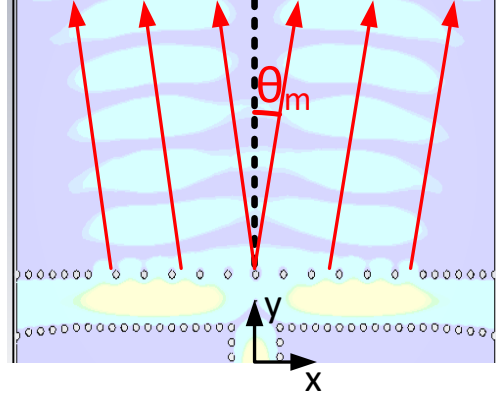
Figure 4.3: Diagram of leaky-wave propagation through SIW partially reflective surface wall.

propagation angle for the bound TEM waves are not normal to the launcher

Once the width W of the bounded SIW section is known, a dispersive analysis of the SIW for different values of P and d must be completed [57]. This analysis can be performed using an adapted version of the transverse equivalent network as previously defined in [56, 57] and the approaches presented in [136]. The transverse equivalent network is based on an equivalent transmission line circuit of the structure under analysis operating at the frequency of operation. One of the conditions of this network is that, at any point on the line, the sum of the input impedances seen looking to either side must be zero. Therefore, from this network, the transverse resonance equation that allows propagation constant calculation can be obtained [102]. In this case, the right side of the transverse equivalent network depicted in Fig. 4.5 is not terminated with the radiation impedance as presented in [57], instead, the characteristic impedance of an infinite parallel-plate waveguide is now defined for the developed circuit model [136] as the parallel-plate waveguide is not truncated anymore. Moving towards the left side of the model, a T-network characterises the partially reflective wall of vias. Specifically, it can be modelled with two capacitors in series and one inductor in parallel following the equivalent model for inductive posts in parallel-plate waveguides described in [136]. This T-network is followed by the second transmission line of length W, which is the space between the two rows of vias, i.e. the width of the SIW section. Finally, the last element of the model is the non-leaky PEC wall represented by a short circuit.

The transverse resonance equation at the reference point in Fig. 4.5 is enforced to determine the dispersion behaviour of the leaky section. This equation is $Z_L(k_y) +$

f=14 GHz

f=15 GHz

f= 15.3 GHz
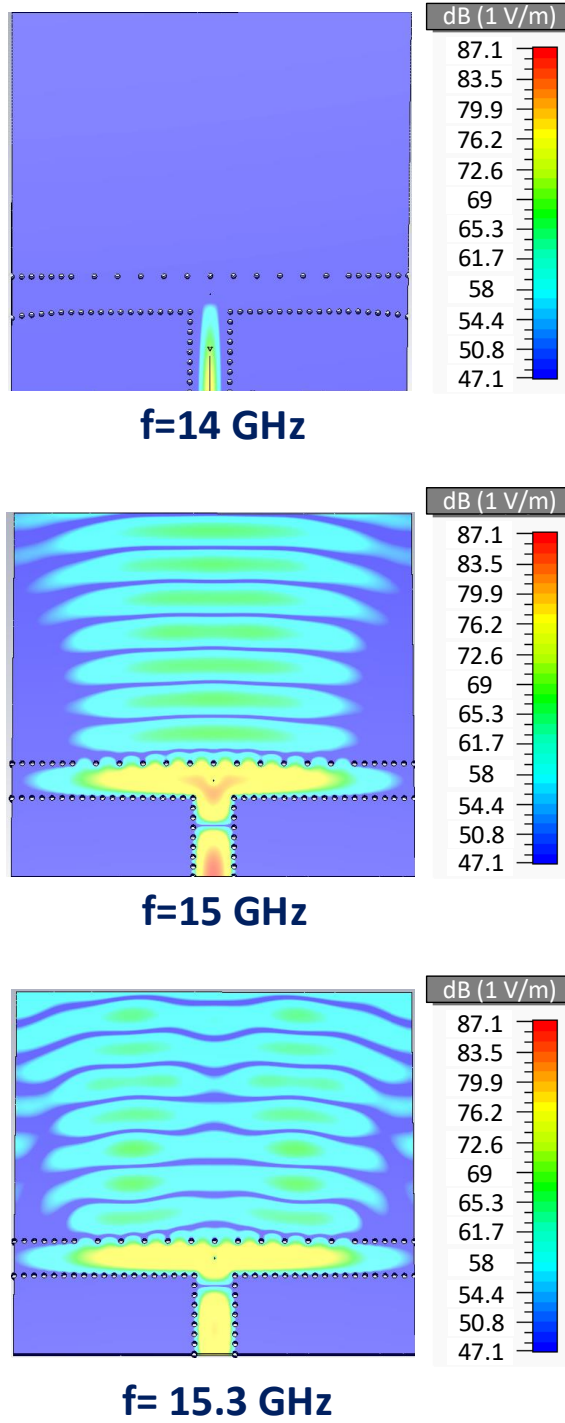
Figure 4.4: Snapshot in time of the simulated electric fields generated by the launcher. [From [128] © 2019 IEEE].

$Z_R(k_y) = 0$ where

$$Z_L(k_y) = j \tan(W \cdot k_y) \cdot Z_{o_{TE}}(k_y) + j \cdot X_b \tag{4.3.1}$$

$$Z_R(k_y) = \frac{jX_a \cdot (Z_{o_{TE}}(k_y) + jX_b)}{jX_a + Z_{o_{TE}}(k_y) + jX_b} \tag{4.3.2}$$

and $k_y = \sqrt{k_0^2 \varepsilon_{\mathrm{r}} - k_x^2}$ is the transverse wavenumber inside the SIW, where X_b and
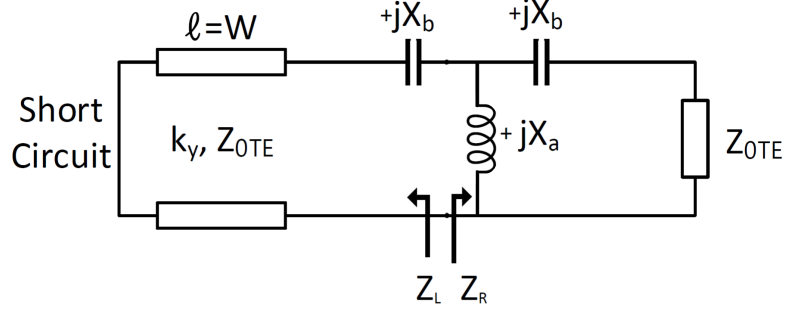
Figure 4.5: Schematic of the transverse equivalent network circuit model for the proposed SIW structure enabling bound TEM-mode launching inside a parallel-plate waveguide. [From [128] © 2019 IEEE].

X_a are the capacitances and inductance whose equations are explained in [136], and $Z_{0_{TE}}$ is the characteristic impedance for the TE_{10} mode. Dispersion analysis considering no dielectric and conductor losses is reported in Fig. 4.6. It can be observed that the frequency where $\beta = \alpha$ is very close to 15.00 GHz.

This leaky-mode dispersion analysis is needed to tune the pair of values W and P which determine the leaky SIW dimensions that provide the desired beam-splitting condition; i.e. $\alpha \approx \beta$ at the design frequency of 15.00 GHz, as depicted in Fig. 4.7, where it can be observed that the launcher design frequency and the leakage rate can be controlled by modifying W and P. As already deduced from SIW theory, higher cutoff frequencies are obtained when W is smaller. On the other hand, the leakage rate is affected by P. For example, for $P = 2.00$ mm the leakage rate is close
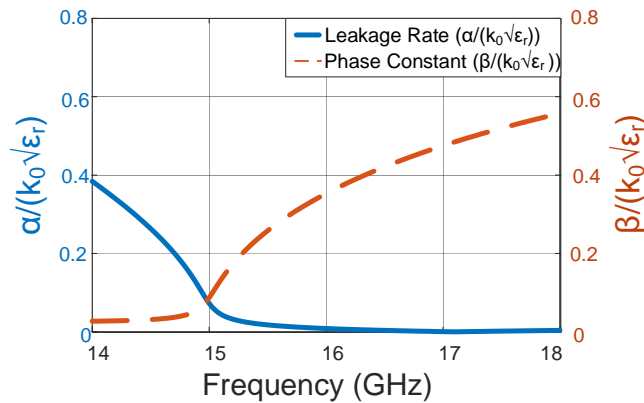
Figure 4.6: Plot of the calculated results of the dispersive analysis for the SIW launcher designed to work at about 15.00 GHz for $W = 6.80$ mm, $P = 4.50$ mm and $d = 1.00$ mm with $\varepsilon_r = 2.2$ and thickness $h = 0.79$ mm. The solid lines represent the complex solution of the transverse resonance equation defined by Eqs. (4.3.1) and (4.3.2); normalised leaky-wave phase constant $\beta/k_0\sqrt{\varepsilon_r}$ in red dashed line and $\alpha/k_0\sqrt{\varepsilon_r}$ in blue [From [128] © 2019 IEEE].
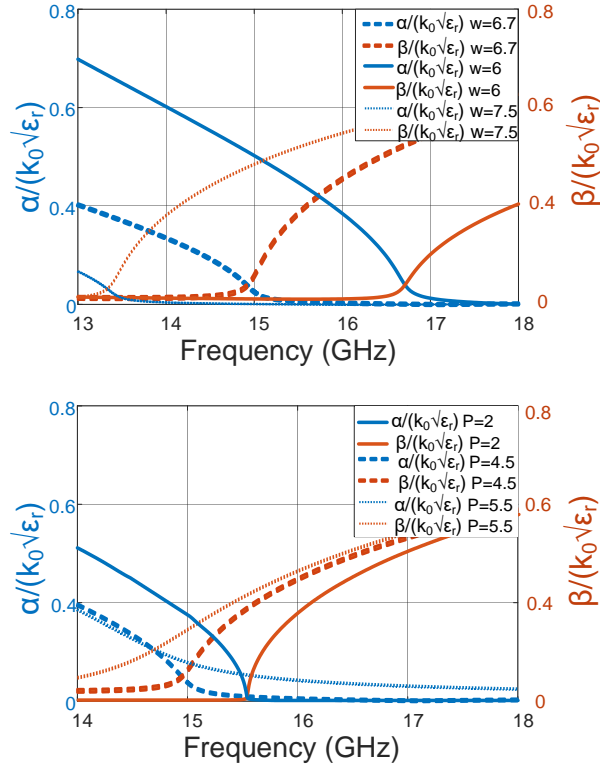
Figure 4.7: Plot of the calculated dispersive analysis for the different values of W (top) and P (bottom).

to zero whereas in the case of $P = 5.50\,\text{mm}$ the normalised leakage rate increases up to 0.10, as depicted in Fig. 4.7.

It should also be mentioned that when using a short circuit to model the PEC wall as in Fig. 4.5, a perfect $180.00°$ reflection is assumed in the analysis for the complex wave. However, the row of vias actually has an inductive behaviour that introduces a phase shift of about $150.00°$ [62] which is $30.00°$ from the perfect short circuit. Following [62] it is possible to achieve a more accurate result if the PEC wall is also modelled with the equivalent circuit used for the partially reflective surface [136] based on a T-network of reactances (see Fig. 4.5) instead of a short circuit .

Next, we can easily find the value for the partially reflective surface wall aperture length L related to α by setting the launching efficiency as 90.00% so $L = 2.3/\alpha$ [131]. The side arms of the T-junction can be left open to ease the design and prototyping process as negligible power is maintained at the end of the arms due to the high launching efficiency. This launching efficiency can be obtained at the edge of the launcher as depicted in Fig. 4.8, where the efficiency is plotted for two different cases (lossless and lossy conditions). The efficiency is 90.00% for the lossless case, falling to 85.00% for the lossy case where substrate dielectric and conductor losses are included. In the lossy case the peak efficiency is shifted in frequency by less than
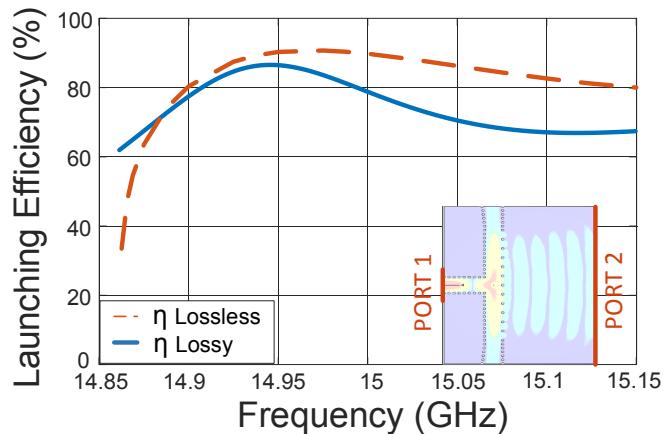
Figure 4.8: Plot of the simulated launching efficiency (η) obtained at the edge of a single launcher structure (shown in inset on the right). The dashed red line shows the launching efficiency obtained for lossless conditions, while the blue line includes dielectric and conductor losses. [From [128] © 2019 IEEE].

0.5%. This shift is caused by some small changes in the lossy case to the loads which model the leaky partially reflective surface sidewall as well as the wave impedances are present which change the reactive values for Eqs. (4.3.1) and (4.3.2). A good agreement is observed with the theoretical leaky-wave model (Figs. 4.5 and 4.6) and the efficiency simulations of the structure (Fig. 4.8), that is calculated directly from the linear values of the simulated transmission coefficients.

The calculation steps for the parameters of interest $W, d, P, L,$ β and α can be summarised as the following:

- Find the width W of the bounded SIW section for a frequency of interest using equations in [54].

- Dispersive analysis of the SIW for different values of P and d satisfying the splitting condition ($\beta = \alpha$) at the operating frequency and then by using the transverse equivalent network model presented in Fig. 4.5.

- Use the calculated α in the previous step to find the length L of the partially reflective surface using $L = 2.3/\alpha$ for an efficiency of 90.00%.

4.3.3 Bloch Analysis

The dispersive analysis has also been alternatively completed by means of a Bloch analysis [137] calculation using CST [12]. Basically, simulations were completed for a cascaded number N of unit cells, considering a straight SIW section with one side
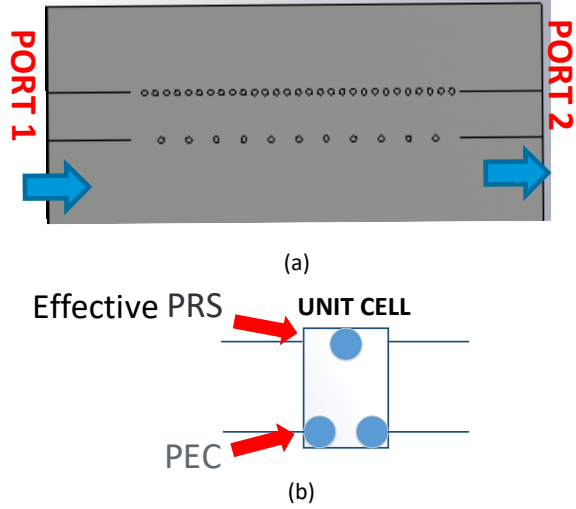
Figure 4.9: Diagrams of (a) SIW section with PEC and partially reflective surface walls defined as a cascaded connection of N periodic unit cells for Bloch analysis; (b) Detailed unit cell consisting of one via from the partially reflective surface wall and two from the PEC wall.

as a PEC wall and the other side as a leaky via side wall, as illustrated in Fig. 4.9, where each unit cell contains one via from the partially reflective surface wall and two vias from the PEC wall. As explained in [138], the S-parameters of this structure are used to find the transfer matrix, or T-matrix, given that the propagation constant is defined by [102]:

$$\cosh \gamma d = (A + D)/2 \tag{4.3.3}$$

where γ is the complex propagation constant and A and D are the elements of the T-matrix.

However, these calculations would be sufficient for an infinite array but not for a limited number of unit cell [137, 138]. This is due to evanescent modes, i.e.,modes below cutoff, contribution at the first and the last unit cell, causing β to have infinite solutions [137, 138]. In order to obtain the correct complex propagation constant γ, simulations for a N+1 unit cell system must also be carried out to obtain the T-matrix. Then, "dividing" both matrices and setting the result to [138]:

$$T = \frac{T_{N+1}}{T_N} \tag{4.3.4}$$

γ can be found using Eq. (4.3.3) as both matrix have the same values for the first and last unit cell [138].

These analysis are compared to the results theoretically obtained using the transverse resonance equation as shown in Fig. 4.10. Nevertheless, small disagreement is
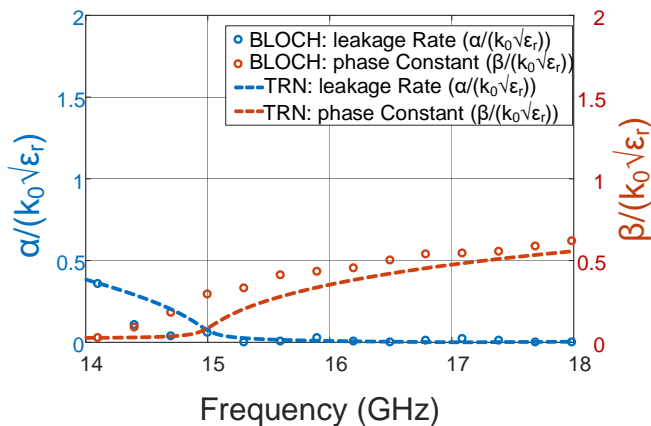
Figure 4.10: Plot of the calculated comparison between the normalised phase constant β and leakage rate α calculated by the Bloch method and the theoretical results obtained with the transverse equivalent network.

observed due to the aforementioned simplifications used in the transverse equivalent network (see Fig. 4.5) when assuming a short circuit to model the PEC wall instead of a T-network of reactances as for the partially reflective surface wall [136].

4.3.4 Microstrip to Substrate Integrated Waveguide Transition

Most of the microstrip-to-SIW transitions are based on the use of a tapered microstrip line which improves the matching from the $50.00\,\Omega$ microstrip line to the SIW input [139].

The taper represents a transition from the quasi-TEM mode into the SIW TE_{10}. The excitation of this mode is possible because of the similarities in the orientation and profile of the electric fields [139]. The general guidelines to design linear tapered lines are well explained in the literature [55]. It is also is possible to model the taper for a non-linear shape as shown in [140], where equations to characterize different shapes depending on the function used for the impedance variation (exponential, cosine or tangential hyperbolic) are reported. Moreover, many different transitions have been designed for better matching purposes or frequency range increase as in [141–143]. For example in [142], two extra vias are added directly on the substrate at the edge between the microstrip taper and the SIW section, these vias improve the matching over a wideband achieving measured return losses values around $30.00\,\mathrm{dB}$.

Nevertheless, the traditional tapered microstrip line could not work in SIW struc-

tures with a higher characteristic impedance in comparison to the microstrip line, as in our proposed structure. This is because the field distribution in the microstrip line is wider than the one in the SIW, and even an optimised design of the traditional microstrip tapered transition does not achieve a good field coupling, as explained in [144]. Hence, the SIW section should be tapered instead of a straight microstrip line [144]. The impedance of the SIW is defined by [144]:

$$Z = \frac{2h}{W} \frac{\eta}{\sqrt{\varepsilon_r}} \frac{1}{\sqrt{1 - (\frac{f_c}{f})^2}} \qquad (4.3.5)$$

being η the wave impedance in the dielectric.

The impedance of the SIW would decrease and the matching would highly improve by means of varying the width W', see Fig. 4.1, between the rows of vias following Eq. (4.3.5), as shown in Fig. 4.11.

The closer α is to β, i.e. closer to the beam splitting point, the higher is going to be the impedance in the SIW structure for the width calculated, making necessary a non traditional microstrip-to-SIW transition.

As usual in the design of matching networks, the length of this taper should be set for any multiple of $\lambda_g/4$. The width W_o and length L_o of the microstrip line are calculated for a given frequency and impedance [102]. Once the maximum width of the taper W' is found for the desired impedance, the width between the following vias must be set. In [?] it is shown that for a better matching the position of the vias should follow an exponential distribution given by (4.3.6) and (4.3.7):
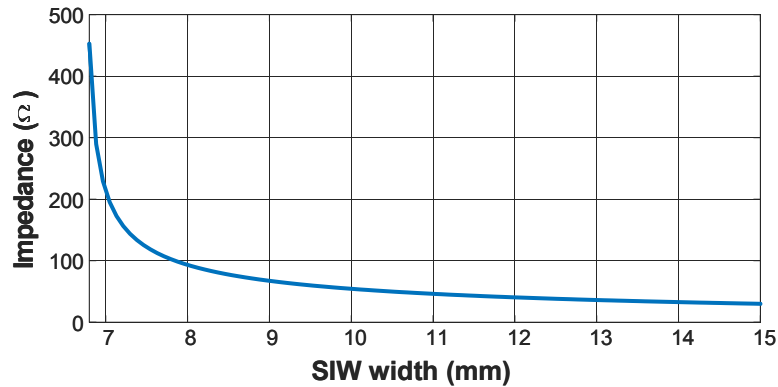
Figure 4.11: Plot of the calculated impedance of a SIW as a function of the separation between the vias depending on the desired impedance value starting from the width of our structure W=6.80 mm.

$$y = 0.01\frac{W}{2}e^{bx} + 0.99\frac{W}{2} \qquad (4.3.6)$$

$$b = \frac{\ln(100\frac{W'}{W}) - 99)}{L_t} \qquad (4.3.7)$$

where y is the half separation between the vias, x the distance to the point of the desired impedance and L_t is the length of the taper [144].

4.3.5   Excited Fields and Modes

TE_{10} and TEM modes can be excited within the SIW feed structure. In order to confirm that the modes excited in the structure are the expected ones, E-fields and H-fields have been simulated in the corresponding sections, inside the bounded SIW section and the TEM mode along the width of the parallel-plate waveguide region. The simulated field components for these modes, the TE_{10} mode inside the SIW section and the TEM mode inside the parallel-plate waveguide, are depicted in Fig. 4.12. These modes are compared to the ones existing in a typical SIW and parallel-plate waveguide. For the TE_{10} mode, it is shown that there is no E-field component along the direction of propagation ($E_y = 0$) whereas the magnetic field component is non-zero ($H_y \neq 0$). On the other hand, inside the parallel-plate waveguide, there are no components in the direction of propagation ($E_y = 0$, $H_y \approx 0$) as expected for a TEM mode.

The normalised amplitude distribution and the phase are further depicted in Fig. 4.13, where it can be observed that the amplitude is uniform along most of the launcher aperture and start to decay by about 5.00 dB when approaching the PEC sections at the end of the T-junction arms. On the other hand, the phase maintains small variations of 5.00° or less along the entire aperture while the maximum variation of the amplitude values is about 1.50 dB. This is a significant improvement when compared to other designs found in the literature [5,6,92,93]. It should also be mentioned that our aperture profile provides a more uniform distribution when compared to [131], since in that work phase and magnitude variations of more than 25.00° and 2.00 dB were observed, respectively. Some comparisons between the proposed structure and previous feeding networks for slot based planar antennas found in the literature have also been included in Table 4.1. The launcher is more compact as it provides a
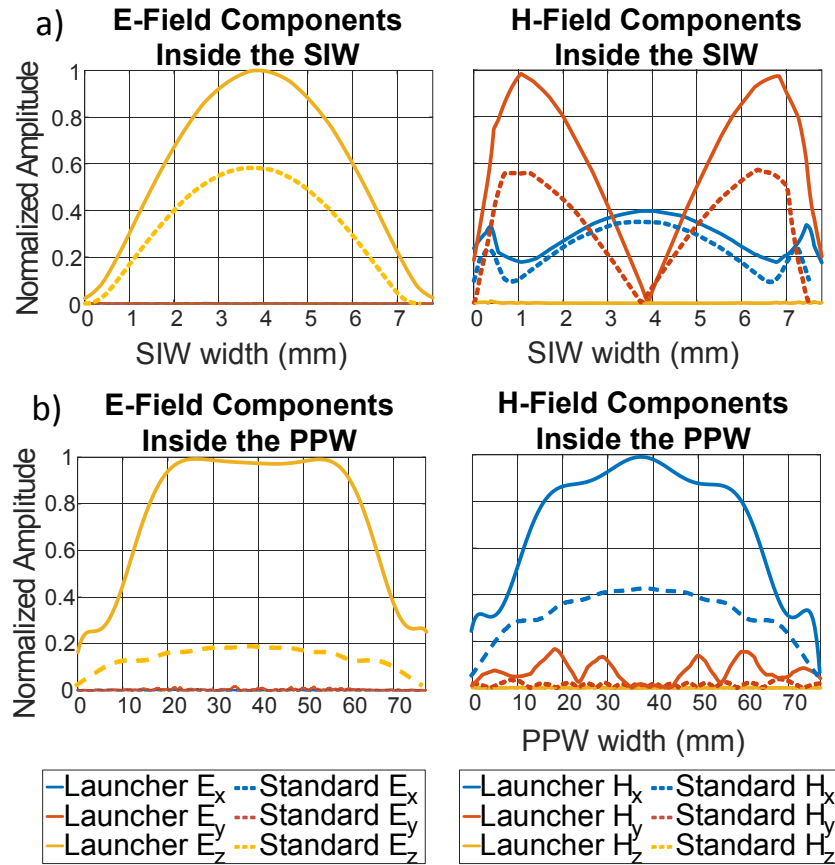
Figure 4.12: Plot of the normalised simulated field components within the end-to-end configuration compared to the fields existing in a standard SIW or parallel-plate waveguide along the x-direction: (a) electric and magnetic field components for the excited TE_{10} mode inside the bounded SIW section, (b) the TEM mode inside the parallel-plate at a distance of $10.00\,\mathrm{mm}$ from the aperture [From [128] © 2019 IEEE].

reduction of 61.56% and 55.90% when compared to [5] and [6]. Furthermore, more stable amplitude and phase values are obtained. In terms of amplitude, this work presents a small variation of $\pm 1.50\,\mathrm{dB}$ which is a 85.00% and a 50.00% more stable than [4] and [5]. The phase, on the other hand, has a variation of $\pm 5.00\,^{\circ}$, representing a 75.00% and a 83.33% of improvement with respect to [4] and [5]. Moreover, the launching efficiency achieved by this launcher is a 44.44% and a 10.00% higher than [4] and [6].

Following these developments and modal characterization, an end-to-end test device using two launchers has been designed and optimised using the commercial full-wave simulation tool CST Microwave Studio [12]. See Fig. 4.14 where the simulated electric fields are depicted and show uniform propagation within the parallel-plate waveguide region.

Table 4.1: Feeding Network Performance Comparison

	Aperture size	Amplitude variation (dB)	Phase distortion (deg.)	Efficiency (%)	Feeding mechanism
[4]	$1.93\lambda_0$	± 10.00	± 20.00	50.00	Slotted waveguide
[5]	$6.50\lambda_0$	± 3.00	± 30.00	50.00	Coupling windows
[6]	$5.67\lambda_0$	-	-	81.00	Multiple reflector system and twin pin feeder with leaky partially reflective surface ($\beta > \alpha$)
This work	**$2.50\lambda_0$**	**$< \pm 1.50$**	**$< \pm 5.00$**	**>85.00**	**Leaky SIW T-junction and Single-input microstrip feed ($\beta \approx \alpha$)**
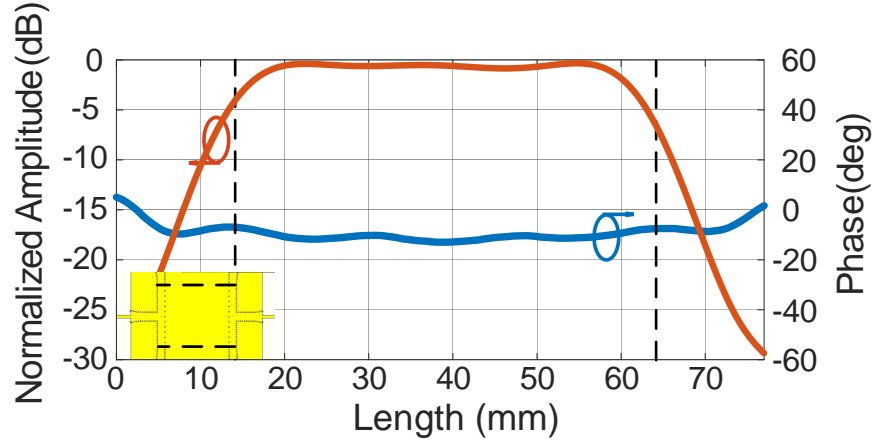
Figure 4.13: Plot of the normalised simulated amplitude in dB and the phase in a transverse plane within the end-to-end for the dominant component E_z. The two dashed black lines define the ends of the partially reflective surface wall [From [128] © 2019 IEEE].

4.3.6 Measurement Results and Discussion

As a proof of concept, an end-to-end structure has been manufactured on a ROGERS RT5880 substrate with a thickness h of 0.79 mm and a relative permittivity $\varepsilon_r = 2.2$ at 10.00 GHz; a photograph of the realised prototype is shown in Fig. 4.15 while measurements are shown in Fig. 4.16. The relevant parameters defined for this parallel-plate waveguide launcher to achieve a design frequency of 15.00 GHz are as follows: $W = 6.80$ mm, $W' = 10.20$ mm, $W_o = 2.35$ mm, $P = 4.50$ mm and $d = 1.00$ mm.

The two launchers were placed $4.30\lambda_g$ apart for practical demonstration purposes. This introduced some conductor and dielectric losses which slightly increased the port-to-port insertion losses, but still the launcher is operating as expected as shown in Fig. 4.16. The measured $|S_{21}|$ for the test structure is about 1.30 dB at the design frequency of 15.00 GHz and $|S_{11}| > 20.00$ dB. The electromagnetic coupling between the two launchers is not of concern because the complete end-to-end struc-
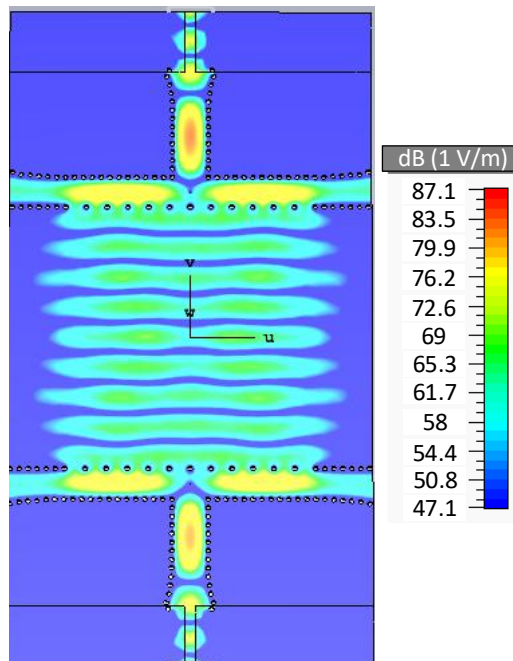
Figure 4.14: Snapshot in time of the simulated electric fields within the examined PCB test circuit using two launchers. [From [128] © 2019 IEEE].

ture was simulated in CST [12] and no significant losses were found, as shown in Fig. 4.17. This is important because the launchers are not in the respective far-field regions for each wave-guiding structure, which we consider to be $32\lambda_g$ following $R = 2D^2/\lambda_g$ [145] (where $\lambda_g = \frac{1}{f\sqrt{\varepsilon_r \varepsilon_0 \mu_0}}$ and ε_0 and μ_0 are the free-space permittivity and permeability, respectively, and D is the length of the leaky aperture). Also, as it can be seen in Fig. 4.16 the measurements obtained with a 2-ports vector network analyser are in good agreement with the simulations as well as the center frequency for the structure designed using leaky-wave theory and the developed transverse equivalent network circuit model. The difference between the measurements and simulations can be attributed to the practical variation of the relative permittivity of the substrate (see yellow dashed lines). Regardless of these practicalities the launcher is still operating as expected, showing proof of concept

Higher losses for the measured structure at the design frequency can be explained by the importance of the substrate relative permittivity as well as the fabrication tolerances for via placement and via diameters. More specifically, the via drilling processes defines the exact via placement and its diameters and small variations from any nominal value can result in minor performance variations and small frequency shifts away from the original design frequency. For example, for any minor variation
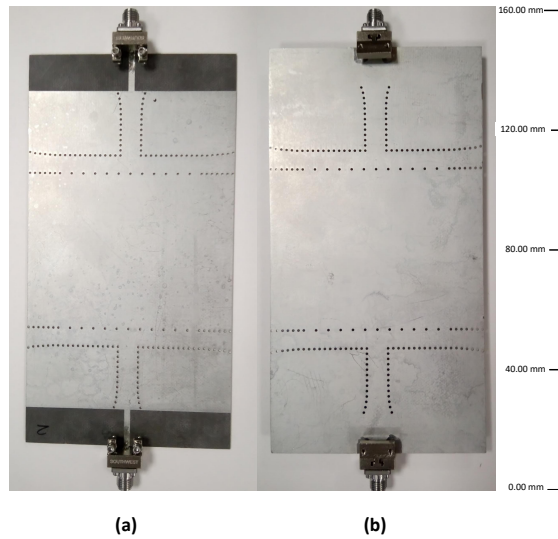
Figure 4.15: Photograph of the manufactured prototype to work at 15.00 GHz on ROGERS RT5880 with $\varepsilon_r = 2.2$ for the relative permittivity [From [128] © 2019 IEEE].
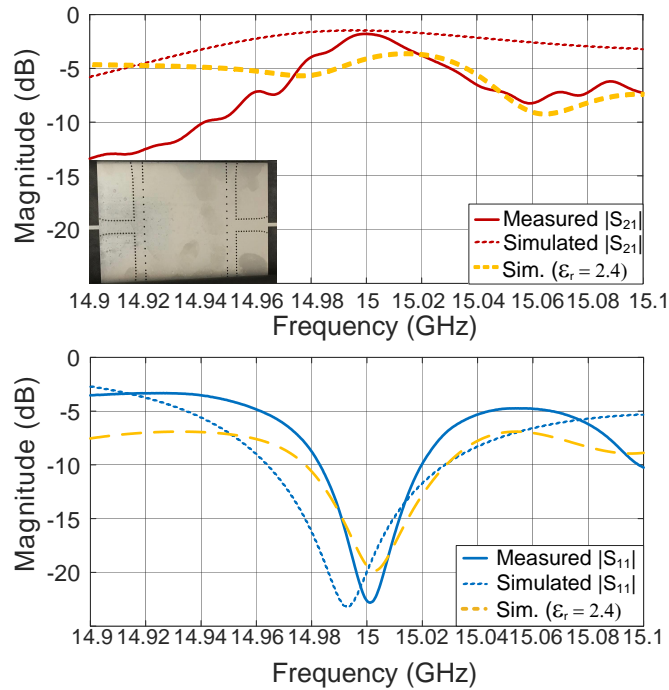
Figure 4.16: Plot of the measured S-parameters for the structure under test (solid lines) compared to simulations (dashed lines) using the rated values for the dielectric $\varepsilon_r = 2.2$ at 10.00 GHz. [From [128] © 2019 IEEE].

in ε_r (see Fig. 4.16) port matching can be maintained, however the maximum value for $|S_{21}|$ can be shifted in frequency because the initially designed $\alpha \approx \beta$ condition is no longer preserved at the original design frequency. This can be observed in Fig. 4.16 when considering $\varepsilon_r = 2.4$ since good port matching is still obtained at 15.00 GHz ($|S_{11}| > 15.00$ dB) while $|S_{21}|$ is less than 4.00 dB at about 15.02 GHz as observed for the simulations. Also, in the simulation model it has been considered a
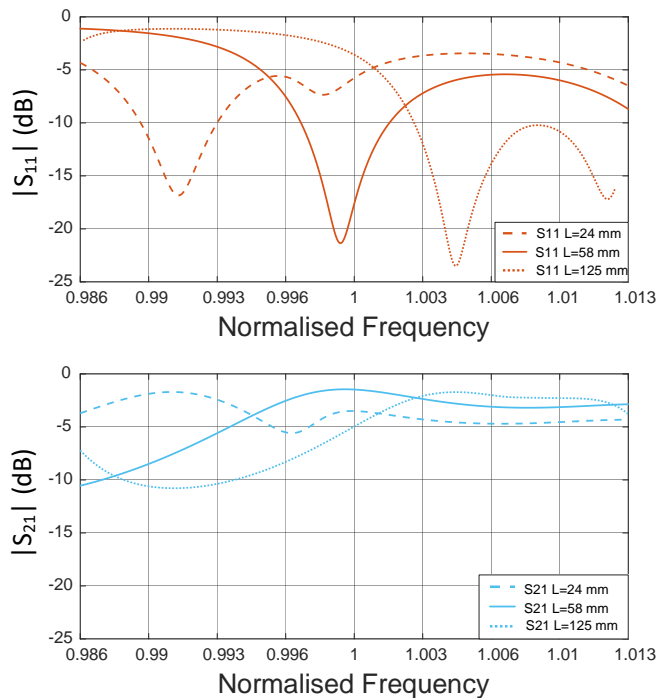
Figure 4.17: Plot of the simulated S-parameters response for different parallel-plate waveguide length variations. The response of the launchers placed close to each other is represented in dashed lines, original design length in the solid lines while the launchers separated by a longer distance in dotted lines.

$\pm 5.00\%$ variation in the diameters of all the vias within the transition structure and about a 0.50% frequency shift in the minimum of $|S_{11}|$ was observed (see Fig. 4.18). Despite these practicalities, the measured performance is still in good agreement with the full-wave simulations. The structure is also inherently narrow band due to the $\alpha \approx \beta$ condition at the design frequency. This can be observed in Fig. 4.16 for both the measurements and the simulations as $|S_{11}| > 10.00\,\text{dB}$ from about $14.98\,\text{GHz}$ to $15.02\,\text{GHz}$.

4.4 Truncated Parallel-plate Waveguide Surface-wave Launcher

An interesting alternative to the launcher explained in Chapter 3, would be the use of this parallel-plate waveguide launcher as a planar TM_0 surface-wave feed system offering a uniform phase front. As it is based in the parallel-plate waveguide TEM launcher structure, by following these earlier developments and the work in [85, 128, 131], we offer an alternative surface-wave feed system while using a planar
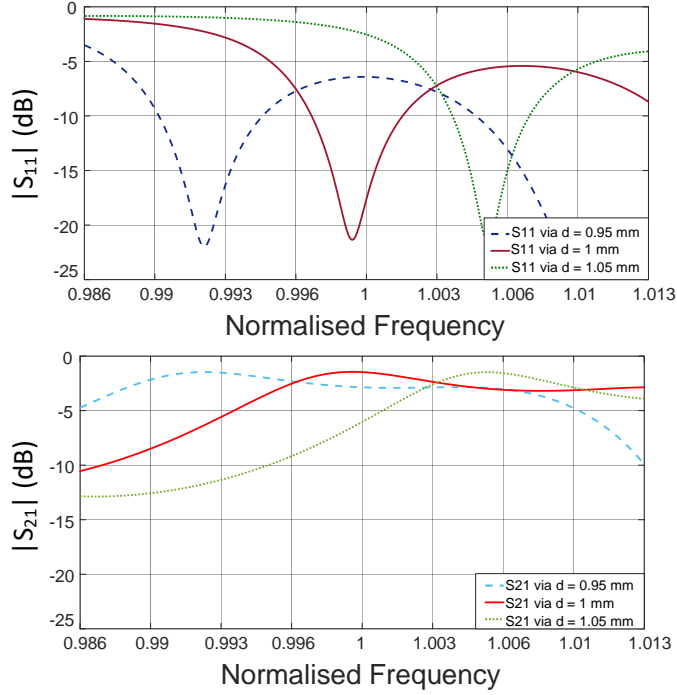
Figure 4.18: Plot of the simulated S-Parameters for three different via diameters with respect to the normalised frequency. Dashed blue lines represent the results obtained for a slightly smaller via diameter, on the contrary green dotted lines depict a larger diameter, while the solid red lines depict S-parameters for the originally intended via diameter.

substrate for low-cost fabrication. In particular, it is now designed with a parallel-plate waveguide section that supports a TEM mode, and a surface-wave section, that supports the TM_0. Power leaked into the TEM mode by the via separation and coupled into the TM_0 surface-wave mode by truncating the parallel plate at a fixed distance S while also including a matching section which employs sub-wavelength patches [118, 120]. The complete structure (transition and matching section) for this TM_0 surface-wave launcher is shown in Fig. 4.19.

4.4.1 Design and Simulation Results

The modified launcher also operates at 15.00 GHz, keeping stable the surface-wave phase front in a narrow bandwidth. This is due to the design principles of the leaky SIW T-junction; i.e. if the frequency is below 15.00 GHz the propagating mode is evanescent (under cutoff) with limited field penetration into the parallel-plate waveguide and the surface-wave regions. At higher frequencies (above 15.00 GHz) two different wavefronts are possible which diverge from the broadside direction of propagation (perpendicular to the leaky wall).

The design procedure can be divided in three parts. While two of them have already been explained in Section 4.3 (the microstrip to SIW transition and leaky SIW T-junction), in this section the focus will be on the new matching network utilised to smooth the transition from the parallel-plate waveguide TEM mode to the TM_0 surface-wave of the grounded dielectric slab. Also, the dielectric material selected for the TEM parallel-plate launcher is kept for this structure being the ROGERS RT5880 with a relative permittivity of 2.2. However, in this case a larger thickness of 1.575 mm is chosen to better confine the surface-wave in the grounded dielectric slab. It should also be mentioned that this structure offers unimodal behaviour due to the high cutoff frequencies for the following TE_1 higher modes which are 64.16 GHz in the parallel-plate waveguide and 43.47 GHz in the grounded dielectric slab.

The transition between the TEM parallel-plate waveguide mode to the TM_0 surface-wave mode is made by first truncating the parallel-plate waveguide at a fixed distance S from the SIW conducting via edge. This distance is set to be a multiple of $\lambda_g/4$ to prevent high reflections. This follows the principles explained in Chapter 3, Section 3.2, where efficient surface-wave excitation was achieved by means of a truncated parallel-plate waveguide [100, 101, 105, 117].

Nevertheless, there is some mismatching between the phase constants β of the
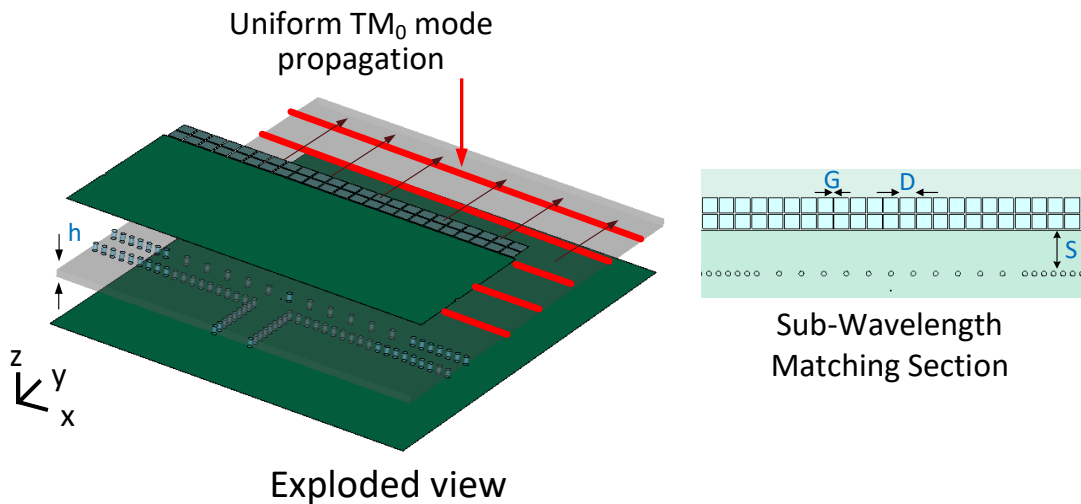
Figure 4.19: Diagram of the proposed TM_0 surface-wave launcher system for grounded dielectric slab with a 50.00 Ω microstrip input. It is composed of a microstrip transition, the leaky SIW T-junction, and the added sub-wavelength matching section for surface-waves [From [85] © 2017 IEEE].
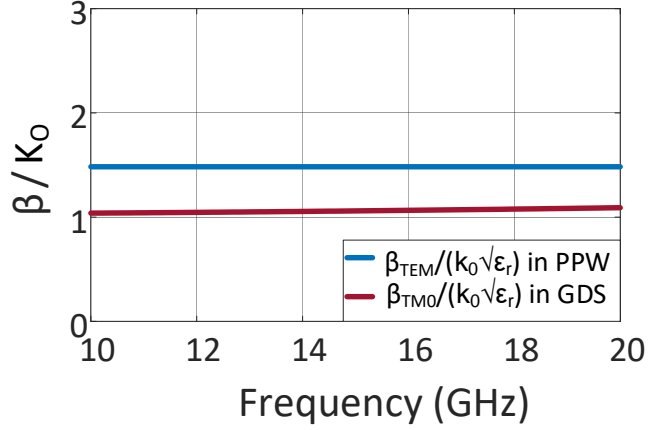
Figure 4.20: Plot of the normalised phase constant calculations for the parallel-plate waveguide TEM mode (blue) and the TM_0 surface-wave mode of grounded dielectric slab (red) [From [85] © 2017 IEEE].

parallel-plate waveguide mode and the TM_0 surface-wave mode, as shown in Fig. 4.20. This can cause reflections and therefore the necessity of a matching section which can be included next to the edge of the parallel-plate waveguide. In particular, in our case the parallel-plate waveguide is truncated a distance S of a $\lambda_g/4$ from the leaky SIW T-junction for improved matching and general design compactness. This matching section for surface-waves consists of a sub-wavelength square array of metallic patches printed on top of the substrate [118, 120]. This section has two parameters, the distance D between patches and the gap G between them. The surface grid impedance, Z_g, related to the alteration of the gap G between the patches allows the phase constant β of the TM_0 surface-wave mode to be tailored and controlled [118, 120]. The size of the matching section is also $\lambda_g/4$, with a total length of 10.05 mm, a distance D between the patches of 4.80 mm and a gap G of 0.48 mm. The reason why this is considered a sub-wavelength array is because the distance D is more than four times smaller than the free-space wavelength [120]. Also, these parameters can be found by using the following equations [118, 120] and full-wave simulations:

$$Z_g = -j\frac{\eta_{eff}}{2\gamma} \tag{4.4.1}$$

$$\gamma = \frac{k_1 D}{\pi} ln \frac{1}{\sin(\frac{\pi G}{2D})} \tag{4.4.2}$$

where Z_g is the surface grid impedance and $k_1 = k_o\sqrt{\varepsilon_r}$, the effective impedance $\eta_{eff} = \sqrt{\mu_o/(\varepsilon_o\varepsilon_{eff})}$ and the relative effective permittivity $\varepsilon_{eff} = (\varepsilon_r + 1)/2$.

A comparison of the reflection coefficients versus frequency for the structure with
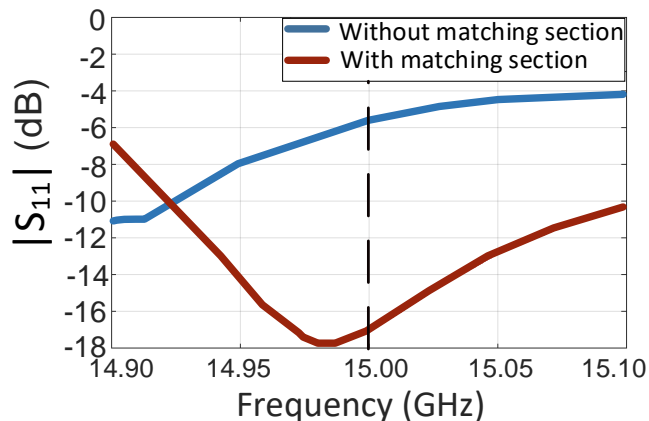
Figure 4.21: Plot of the simulated reflection coefficient versus frequency with and without the matching section for surface-wave excitation [From [85] © 2017 IEEE].
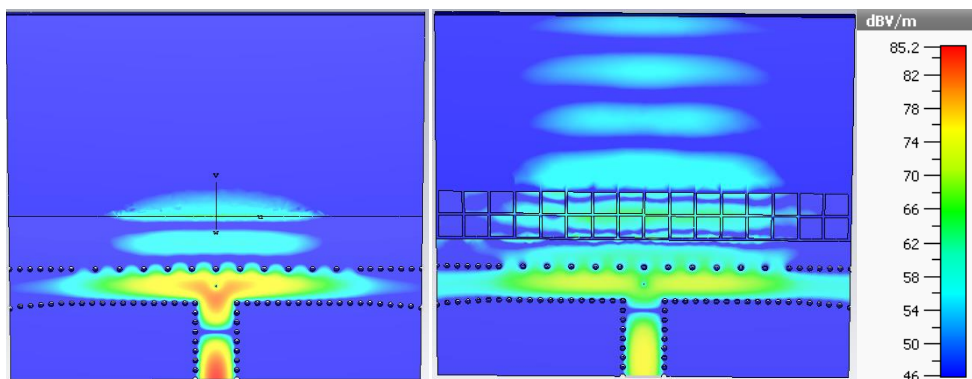
Figure 4.22: Plot of the full-wave CST [12] simulations of the instantaneous E-field intensity within the structure without (left) and with the matching section (right) [From [85] © 2017 IEEE].

and without the matching section is in Fig. 4.21. An improvement of 11.00 dB at the design frequency is obtained; i.e. $|S_{11}| > 17.00\,\mathrm{dB}$ at the $50.00\,\Omega$ microstrip input. Moreover, in Fig. 4.22 the full-wave simulations show the plane wavefront for both cases with and without the matching section. Furthermore, it can be observed that field strength decreases beyond the parallel-plate waveguide region due to radiation at the discontinuity (see Fig. 4.22 (left)), whereas for Fig. 4.22 (right), the sub-wavelength network causes the fields to be confined to the surface until the end of the substrate.

On the other hand, these launchers (parallel-plate waveguide launcher and surface-wave launcher), if truncated at the end of the substrate, can support end-fire radiation. As it can be observed in Fig. 4.20, phase constant values are very close to k_0 suggesting free-space radiation if better optimised. Therefore, these structures
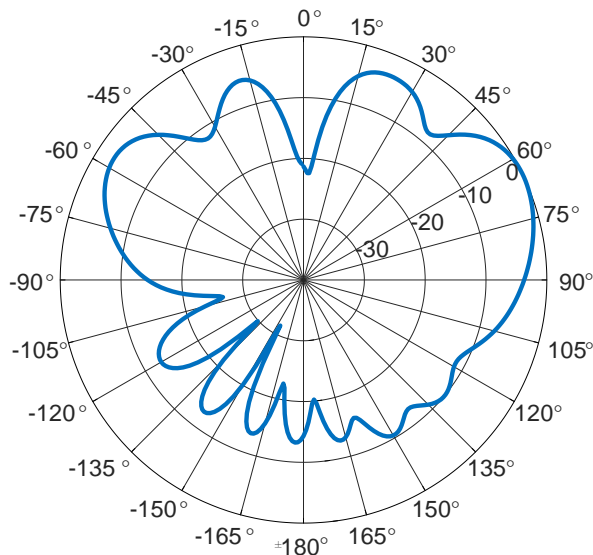
Figure 4.23: Plot of the full-wave CST [12] simulations of the normalised radiation pattern of the surface-wave launcher from Fig. 4.19.

could also have applications as linearly polarised (LP) end-fire antennas if the dielectric substrate is truncated after the matching section. As depicted in Fig. 4.23, this structure when truncated, even without being optimised for such edge radiation, as this is beyond the scope of this thesis, it has a main beam pointing towards the end-fire direction ($\theta = 65.00°$) with realised gain values around $12.00\,\text{dBi}$. The other important feature to appreaciate is the back-lobe radiation which is generally unwanted in end-fire surface-wave antennas [60, 101, 146–148].

4.5 Summary

In this chapter, the use of leaky-wave concepts to efficiently feed other antenna systems have been discussed. Design guidelines and measured results for a novel parallel-plate waveguide TEM mode launcher for feeding planar circuits and low-cost antenna systems have been presented. This SIW-to-parallel-plate waveguide transition is compact, maintains a low profile for simple fabrication and offers $50.00\,\Omega$ microstrip feeding. By design of the structure, uniform and bound propagation at broadside (with respect to the leaky SIW side wall) can be achieved within the parallel-plate waveguide region. Due to the practical substrate variations and SIW technology fabrication tolerances, the measurements of the demonstrator circuit are not exactly as per the full-wave simulations. However, measurements of this end-to-

end test structure still suggest that the two launchers operate at about 15.00 GHz, as per design, and follow the developed leaky-wave theory and waveguide dispersion analysis. When compared to previous configurations found in the literature, this launcher is more compact as it provides a reduction of 61.56% and 55.90% when compared to [5] and [6]. Furthermore, more stable amplitude and phase values are obtained. In terms of amplitude, this work presents a small variation of ± 1.50 dB which is a 85.00% and a 50.00% more stable than [4] and [5]. The phase, on the other hand, has a variation of $\pm 5.00\,°$, representing a 75.00% and a 83.33% of improvement with respect to [4] and [5]. Moreover, the launching efficiency achieved by this launcher is a 44.44% and a 10.00% higher than [4] and [6].

The proposed parallel-plate waveguide TEM planar launcher can be re-designed when using different permittivity substrates and when considering operation at higher millimeter-wave frequencies. Also, the relatively narrow band behaviour of the structure could be improved by employing a double layer of partially reflective surfaces. This can create two cavities where the modes can couple as studied in [149] increasing the possible frequency range of the structure.

In turn, additional applications as the proposed structure for TM_0 surface-wave plane wave excitation, offers an alternative to Yagi-Uda like slot arrangements in the ground plane which can couple power into the dominant TM_0 surface-wave mode of a grounded dielectric slab and to the launcher presented in Chapter 3. Full-wave simulations confirm operation of the feed system and reduced reflections are observed, i.e. $|S_{11}|$ is about 20.00 dB, thanks to the use of a sub-wavelength matching section consisting of an array of square patches. Moreover, efficient end-fire antennas can be also implemented following the proposed design. High gain values are achieved around 12.00 dBi for a non-optimised antenna. Also, back-lobe radiation effects could be minimised if the aperture length is increased allowing for improved directivity.

To the Author′s knowledge, such a compact, simply-fed, and low-cost design, using well-known SIW microwave elements to efficiently launch the TEM mode into parallel-plate waveguide or the TM_0 mode into the grounded dielectric slab with a planar wavefront, has not been reported previously beyond the scope of this PhD.

Chapter 5

Omnidirectional Conical Radiation Through Cylindrical Leaky-waves

5.1 Introduction

In this chapter, two low-cost configurations for two-dimmensional (2D) leaky-wave antennas with simple vertical dipole feeding will be presented and compared. Both antennas are fed at the centre of the structure which will enable cylindrical leaky-wave propagation resulting in conical beam radiated patterns for the K_u and K bands. These antennas can be an alternative to the use of phased arrays in applications that include wireless power transfer, indoor localization, radar or surveillance systems [150].

Both cylindrical leaky-wave antennas were designed and simulated at La Sapienza University during an ERASMUS+ research exchange where the leaky-wave phase and attenuation constants were characterised using the method of moments (MoM), and results were prepared with the assistance of Davide Comite, Paolo Bacarelli, Paolo Burghignoli, and Symon K. Podilchak. The antennas were manufactured and measured at Heriot-Watt University. Results and comparisons with theoretical and simulated results are presented in the following sections.

The first design is a "bull's-eye" antenna based on the use of a partially reflective surface consisting of a periodic metallic ring grating. This antenna is fed by a simple vertical electric dipole at the center instead of the typical surface-wave launchers or slots [41, 43, 44]. Radiation is based on the excitation of the fast harmonic $n = -1$

of the fundamental transverse magnetic (TM_0) mode that is radially propagating in the grounded dielectric slab. This mode increases the bandwidth when compared to more traditional feeders that excited the higher order mode transverse electric (TE_1) limiting the bandwidth of the antenna. Analysis of the performance of this antenna and the advantages it presents for the near and far-field will be discussed [151]. Simulation results on CST [12] and measurements will be reported.

The second configuration consists of a planar multilayered circular Fabry-Perot cavity antenna [45] fed by an individual vertical electric dipole. Moreover, this dipole will be loaded with three rings of vias to increase the impedance bandwidth. This antenna is based on a parallel-plate cavity with a subwavelength partially reflective surface on top that allows for translational invariance which means that the system will produce the same conical beam response, regardless of how many dipole sources are used. With this feature, the conical beam produced by means of the radiation of the fundamental harmonic $n = 0$ of the fast TM_1 leaky-wave can be used as an element pattern for a phased array in the feeding network. This array of dipoles can enable 2D scanning performance using a reduced number of sources with respect to more conventional array designs [95, 150]. Simulations with the frequency domain solver of CST [12] together with measurement results for a single dipole will be provided showing beam scanning behaviour, while simulations for a 2x2 array of sources will be shown as a proof of concept for 2D scanning.

5.2 Bull's-eye Antenna Design for Omnidirectional Conical Radiation

This cylindrical leaky-wave antenna is based on the perturbation of the TM_0 surface-wave in a grounded dielectric slab with radial geometry exciting the fast spatial harmonic ($n = -1$) [3, 43]. The modal behaviour for this kind can be described by an equivalent one-dimmensional (1D) infinite linear array of straight metallic strips, this is due to the fact that beyond the near-field region each mode has a similar wavenumber k_ρ to its equivalent infinite linear counterpart when keeping the same geometrical parameters [44, 151, 152]. The "bull's-eye" configuration (see Fig. 5.1) is thus capable of radiating a conical beam while also allowing for broadside radiation with simple feeding [41, 44].

Typical theoretical feeding topologies for this microstrip-based planar "bull's-eye" leaky-wave antenna are vertical electric dipoles. In practice, coupling rectangular slots etched over the ground plane in a multilayer version are more common. In addition, directive folded magnetic dipoles implemented on the ground plane have also been proposed keeping a fully integrated system as an alternative when single layer structures are required [84,89]. In the present case, one simple vertical electric dipole is placed at the center of the antenna exciting the fundamental TM_0 mode, which is perturbed by the microstrip grating and transformed into a cylindrical leaky-wave defined by a Floquet-Bloch spatial harmonic $n = -1$ [19–21, 43, 151]. In this way, the bandwidth of the antenna can be increased as the excited mode is the fundamental and not the first higher order mode, TE_1, as for horizontal magnetics dipoles. This vertical electric dipole is a coaxial probe introduced through the center of the dielectric leaving a small air gap for matching enhancement purposes. Relative permittivity from the teflon material that surrounds the pin is very close to the relative permittivity of the dielectric and air, allowing for a smooth transition from the coaxial transverse electromagnetic (TEM) mode into the surface-wave on top.
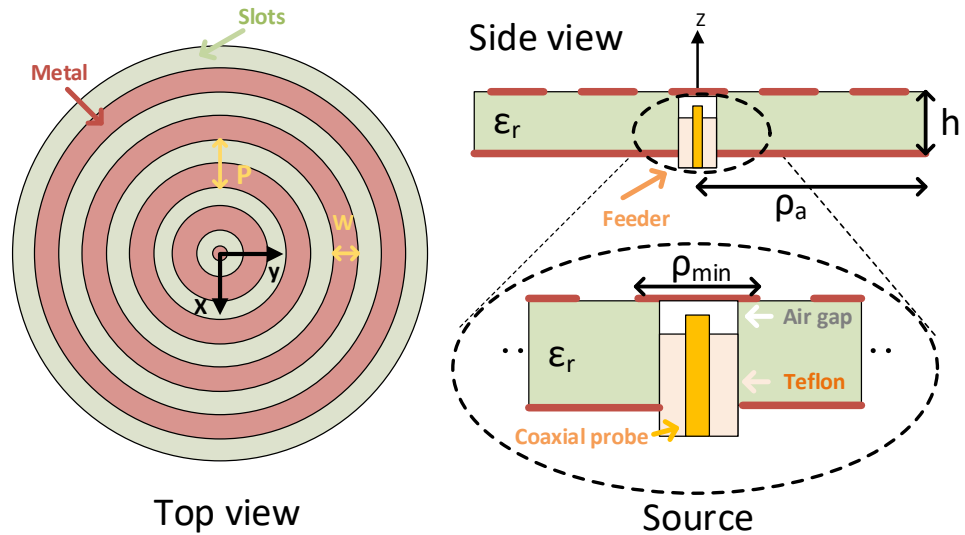
Figure 5.1: Schematic for the proposed "bull's-eye" antenna with parameters: $p = 10.00\,\text{mm}$, $w = 4.00\,\text{mm}$, $\rho_a = 140.00\,\text{mm}$, $h = 3.14\,\text{mm}$ and $\varepsilon_r = 2.2$. In addition, the schematic for the feeding system is also included with the inner ring radius set to $\rho_{min} = 5.00\,\text{mm}$ for matching purposes.

5.2.1   Antenna Design

Modal analysis can be performed by linearising the "bull's-eye" geometry causing the structure to be seen as a 1D periodic array of metallic strips and therefore allowing it to be characterised in terms of space harmonics [43, 44, 151, 152]. The longitudinal wavenumber of the n-th space harmonic propagating in the y direction (see Fig. 5.1) can be found as

$$k_{yn} = k_{y0} + \frac{2\pi n}{p} \tag{5.2.1}$$

being p the periodicity and k_{y0} the fundamental harmonic $n = 0$ wavenumber ($k_{y0} = \beta_0 - j\alpha$) [3]. Following the linearisation method aforementioned, k_{xn} can be assumed to be equal to the radial wavenumber $k_{\rho n}$ of the cylindrical leaky-wave. The transverse complex wavenumber k_{zm}, which is defined by $k_{zn} = \sqrt{k_0^2 - k_{\rho n}^2}$, depending on its backward or forward nature will be a proper harmonic with $\alpha_{zn} < 0$ or an improper harmonic with $\alpha_{zn} > 0$ respectively [3, 153].

Antenna parameters are selected in a way that the fast spatial harmonic $n = -1$ is supported along the frequency range with a backward nature ($\beta_{-1} < 0$). In addition, in-house manufacturing tolerances of ± 0.05 mm were taking into account for the dimensional parameters defined. Therefore, the strip width is set to $w = 4.00$ mm, periodicity $p = 10.00$ mm, grounded dielectric slab radius $\rho_a = 140.00$ mm, a small air gap between the top of the dielectric and the pin of the probe of 0.2 mm to improve matching and a total thickness $h = 3.14$ mm. Moreover, in order to obtain a wideband behaviour, a low permittivity substrate has been selected such as the Taconic TLY5 with a relative permittivity ε_r of 2.2 to expand the impedance bandwidth to lower frequencies [43].

A dispersive analysis by the MoM for the selected parameters was developed and fully described in [44, 151] and it is shown in Fig.5.2. The microstrip width w defines the phase constant behaviour while the phase constant is mainly dependant on the periodicity p. Furthermore, the chosen periodicity $p = 10.00$ mm defines a central frequency around 18.00 GHz with a wide angular beam scanning from 14.00 GHz to 23.00 GHz. On the other hand, strip width is set to $w = 4.00$ mm as it will allow for radiation efficiency values over 90.00% for the whole frequency range [151].

In order to support the required TM_0 cylindrical leaky-wave, a 50.00 Ω coaxial probe is placed at the center of the antenna entering from the ground plane and going
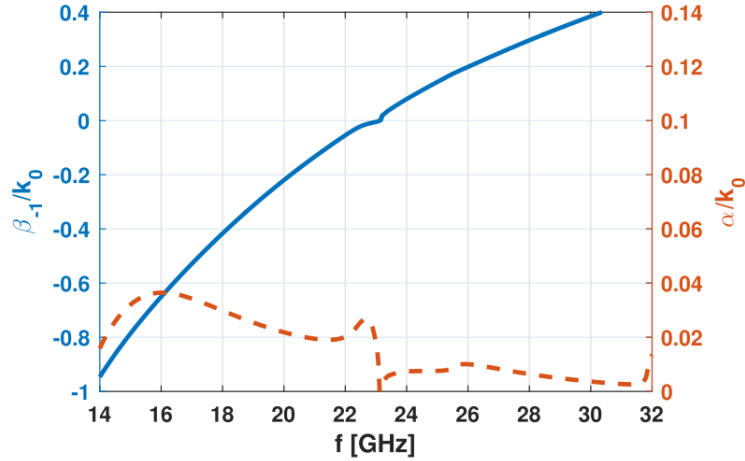
Figure 5.2: Plot of the dispersive analysis for the "bull's-eye" antenna obtained by the MoM for the selected values $w = 4.00\,\text{mm}$ and $p = 10.00\,\text{mm}$. On the left axis the normalised phase constant (blue line) for the fast spatial harmonic, while on the right axis the normalised attenuation constant (red line). [From [151] © 2018 IEEE].

through the z axis up to almost the top of the structure (see Fig. 5.1), where the annular microstrip grating will transform the excited TM_0 surface-wave into the fast cylindrical leaky-wave. The matching is optimised varying the distance between the probe and the first microstrip ring and its radius, which is set to $\rho_{min} = 5.00\,\text{mm}$. As depicted in Fig. 5.3, an impedance bandwidth of more than 45.00% is obtained with reflection coefficient levels below -10.00 dB, except at the open stopband (23.10 GHz) where they increase up to -6.00 dB. Furthermore, maximum realised gain obtained by full-wave simulations in CST [12] is shown in Fig. 5.3 and compared to a MoM analysis based on a Galerkin procedure explained in [154]. A good agreement can be observed for the reflection coefficient specially closer to the maximum gain region. A maximum deviation of 4.00 dB is observed below 21.00 GHz due to manufacturing tolerancies. As expected, maximum gain values are obtained around 23.00 GHz where the beam is pointing to 2.00°. Then it starts decaying again due to the conical nature of the beam that expands its aperture towards the end-fire direction. Open stopband phenomena appears right after 23.00 GHz not affecting the performance since no radiation at broadside is possible.

5.2.2   Far-field Results

The antenna is implemented on a Taconic TLY5 substrate with relative permittivity of 2.2 and thickness of 3.14 mm. The manufactured prototype is depicted in Fig. 5.4.
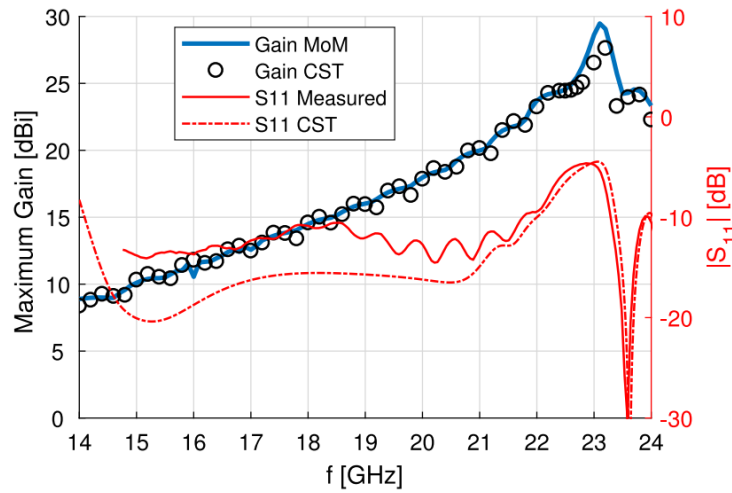
Figure 5.3: Plot of simulated S-parameters of the proposed "bull's-eye" antenna with lossy media in CST [12] compared to measurements in red lines for the designed frequency range (right axis). In addition, expected gain values are depicted in blue and black lines respectively for an arbitrary cut in the azimuthal plane (left axis) [From [43] © 2018 IEEE].
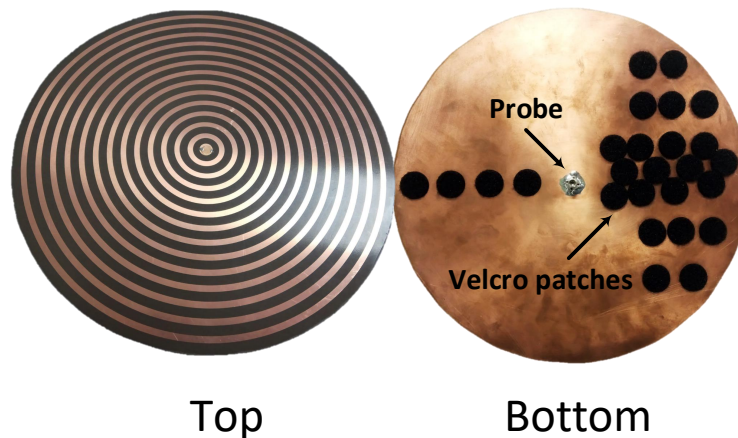
Figure 5.4: Photograph of the manufactured prototype for the "bull's-eye" antenna. Velcro patches on the bottom layer were used for attachment to the NSI system positioners.

Measurements were performed in a calibrated anechoic chamber with the near-field system NSI2000, which transforms the obtained results into the far-field for planar, cylindrical or spherical coordinates, and a two-port network analyser (see Fig. 5.5 for setup details). In addition, gain values are found by the three antenna test method [155]. In this gain comparison method, two pre-calibrated standard gain antennas, in our case the Standard Horn 20240 from Flann, are used to determine the realised gain of the desired antenna by means of different gain measurements to formulate a set of three equations with three unknowns by simple calculations using Friis free-space formulation [155].
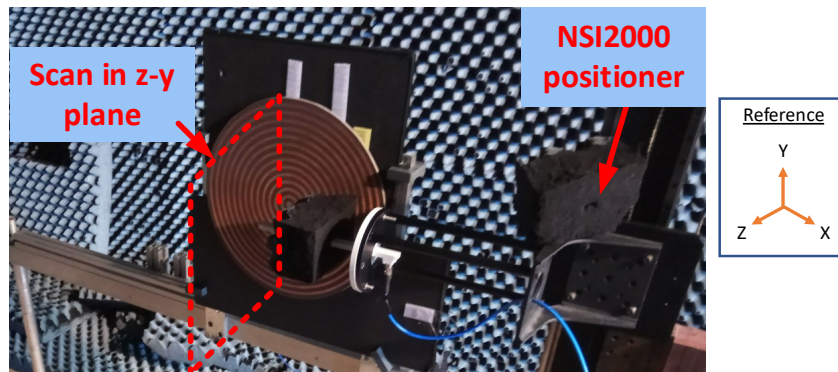
Figure 5.5: Photograph of the setup for measurements with the NSI2000 system inside the calibrated anechoic chamber using a rectangular waveguide probe for the frequency range between 18.00-26.00 GHz.

This cylindrical leaky-wave antenna radiates a highly pure vertical polarised electric field due to the azimuthal symmetry of the structure and the source. Therefore, only measurements of E_θ component are of interest and are normalised and depicted in Fig. 5.6 for the frequency range of operation. As it can be observed, the maximum field values are kept fairly constant in the Φ axis with small variations of $\pm 2.00°$, which indicates an omnidirectional conical pattern. Moreover, these fields are depicted in 3D in Fig. 5.7, where a clear conical beam pattern scanning in frequency is obtained. It must be noted, that there is a gain variation of the conical beam along the azimuth plane, this is likely due to strong mechanical vibrations produced by the NSI2000 positioner when obtaining the measured samples in small increments $(\Delta \simeq 1\,\text{mm})$. In addition, due to in-house prototyping the antenna aperture is not perfectly flat with a deviation of $1.00\,\text{mm}$ over the whole diameter of the antenna. This deviation can also introduce inaccuracies in the measurements.

A cut of the 1D conical beam shape in the far-field for $\Phi = 0.00°$ is also compared to the theoretical equations (using Eq. (2.3.13) from Chapter 2) and assuming $k_\rho = k_y^{LW}$ with the prototype parameters values for consistency) and simulations at different frequencies. As shown in Fig. 5.8, the truncation of the structure causes the appearance of side-lobes, however they are kept below -12.00 dB and can be further reduced if the radius of the antenna ρ_a is increased or locally modulating the complex leaky-wave wavenumber across the radiating aperture, as in [156] where an Archimedean-spiral shape grating was used. Minor discrepancies between the theoretical results and the simulations and measurements are explained by the fact that the physical-optic approach adopted by leaky-wave theory only considers the spuri-
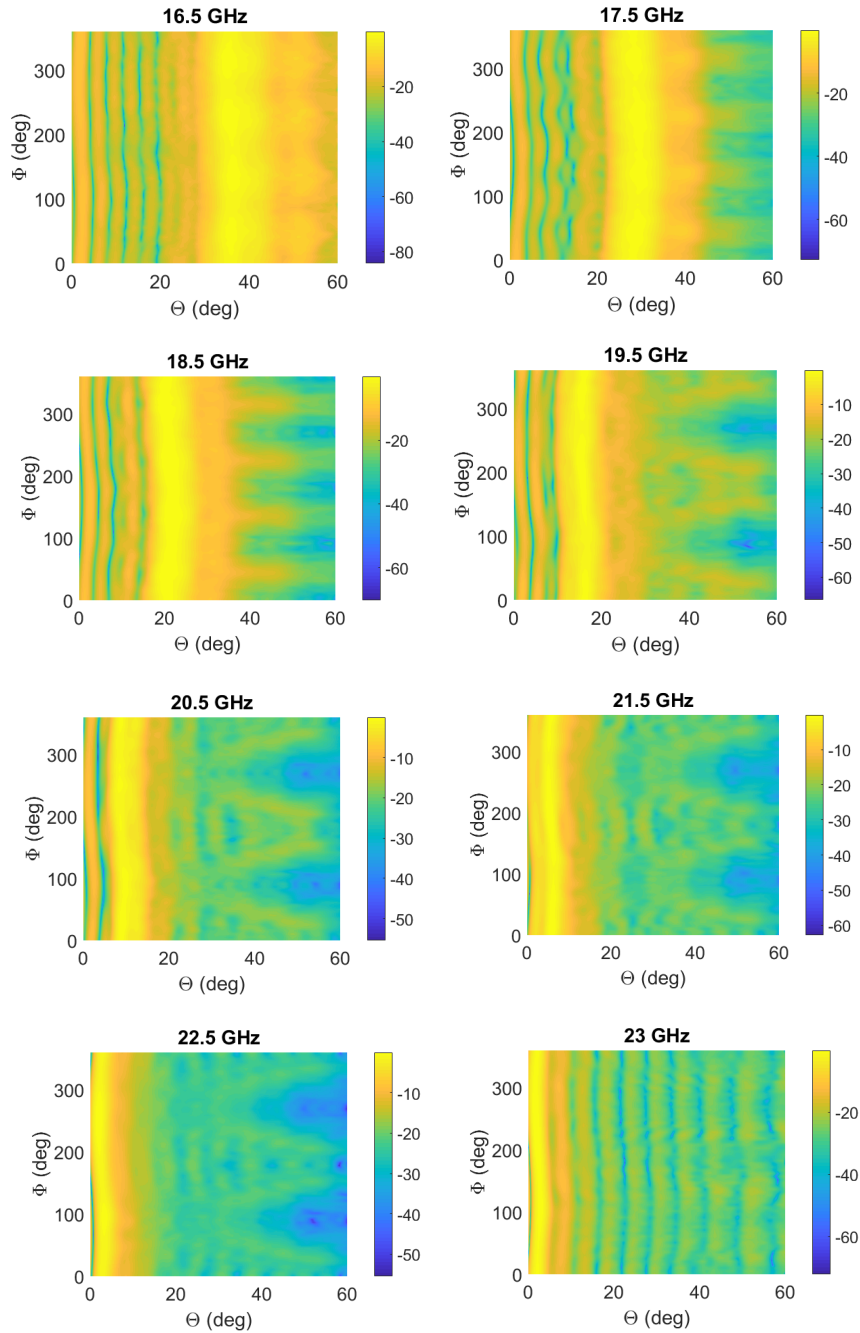
Figure 5.6: Plot of the measured and normalised E_θ fields in the far-field in the $\Phi - \theta$ plane for different frequencies showing beam scanning capabilities.

ous diffraction at the edge of the structure but not the direct space-wave radiation coming from the feeder.

On the other hand, the realised gain, obtained by the three test antenna method aforementioned [155], is compared to the one calculated by full-wave simulations showing good agreement in Fig. 5.9 with gain values up to 20.00 dBi. Furthermore, the conical beam pointing angle θ_p is also compared to the theoretical one obtained
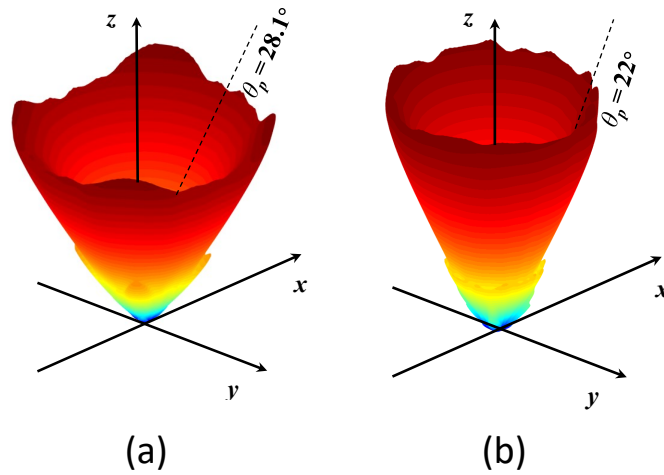
Figure 5.7: 3D plot of measured conical beam pattern for two frequencies showing beam scanning at two frequencies: (a) 17.50 GHz and (b) 18.50 GHz [From [43] © 2018 IEEE].
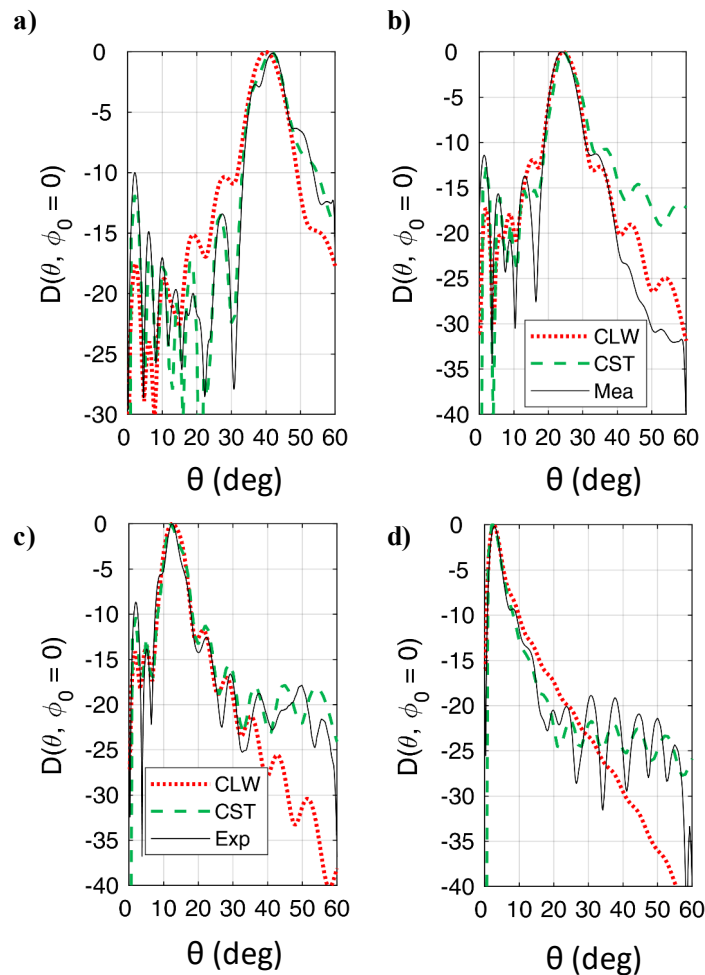
Figure 5.8: Plot of measured and normalised 1D profile for the conical beam at $\Phi = 0$ in the far-field for different frequencies compared to theoretical and simulated results in CST [12]: (a) 16.00 GHz, (b) 18.00 GHz, (c) 20.00 GHz and (d) 22.50 GHz [From [43] © 2018 IEEE].
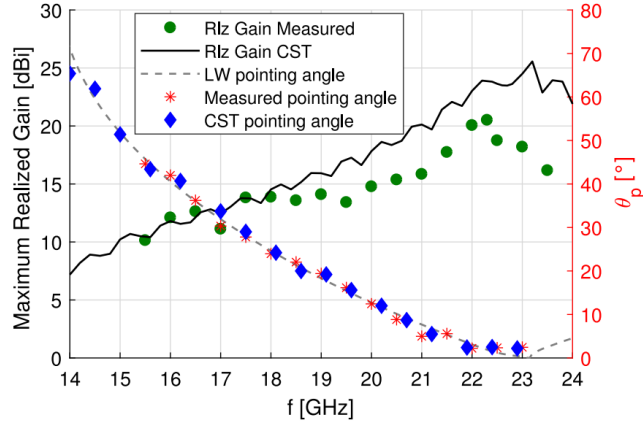
Figure 5.9: Plot of measured realised gain (left axis) and pointing angle (right axis) compared to simulations and theoretical results. In black line the expected realised gain calculated by full-wave simulations and green dots represent the measured realised gain from the three antenna test method. For the pointing angle results, black dashed line depicts the theoretical leaky-wave pointing angle, while red asterisks and blue diamonds show the measured and simulated pointing angles respectively [From [43] © 2018 IEEE].

following Eq. (2.3.17) in Chapter 2 showing excellent agreement with both, simulations and measurements. However, the measured gain is not in perfect agreement with the expected results likely due to practical limitations encountered at the time of measuring. These limitations include the finite size of the anechoic chamber for the large electrical aperture of this antenna, significant free-space loss and cable attenuation. This caused extremely low and noisy received power levels which required the use of amplifiers and could lead to inaccuracies in the gain calculations. Despite these inaccuracies for gain measurements, the reported results are consistent with theory and simulations.

5.2.3 Non-diffracting Behaviour in Near-field

Apart from the conical radiation pattern, this antenna has other attractive features such as its non-diffracting performance in the near-field [151]. This non-diffracting feature is a consequence of the excitation of the Bessel beams by truncating the aperture inside a limited region in the near-field known as non-diffracting range, defined by [43]

$$NDR = \rho_a \cot[\sin^{-1}(\beta_{-1}^{LW} k_0)] \ . \tag{5.2.2}$$

Within this region, the Bessel function can accurately characterise the transverse profile of the beam while beyond it, the beam is not non-diffracting and the Bessel

function representation is not valid anymore. These Bessel beams are ideal non-diffracting solutions for the scalar wave equation [157, 158], where nth-order Bessel function defines their transverse amplitude profile. These beams can only be excited by transversely unbounded apertures, requiring infinite energy to be illuminated [151].

Many studies have focused on the possibility to generate Bessel beams at microwave frequencies. For example, in [159–163] several configurations are proposed, however they can be intricate designs, bulky or narrowband. Therefore, this proposed antenna demonstrates that it is possible to excite such beams in a wideband and a conventional structure, avoiding bulky, complex or expensive designs.

This antenna was measured using the same NSI2000 system as for far-field results but this time operating for the near-field region. The antenna was placed in front of the probe in the $y - z$ plane (with respect to the NSI2000 axis indicated in Fig. 5.5). Simulated electric fields for the normalised transverse E_ρ and longitudinal E_z components at a distance half of non-diffracting range (15.50 cm) are depicted in Fig. 5.10, where the expected Bessel beam can be observed with the maximum and the null of the radiated near-field in agreement with those of the expected theoretical Bessel function with the radial profile given by $J'_0(k^{LW}_{\rho,-1}\rho)$ whose theoretical positions are known a priori [151]. Measurements of the transverse component E_ρ in the $x - y$ plane (with respect to the schematic in Fig. 5.1), i.e., parallel to the antenna aperture, are reported in Fig. 5.11 for three frequencies with the probe placed at two
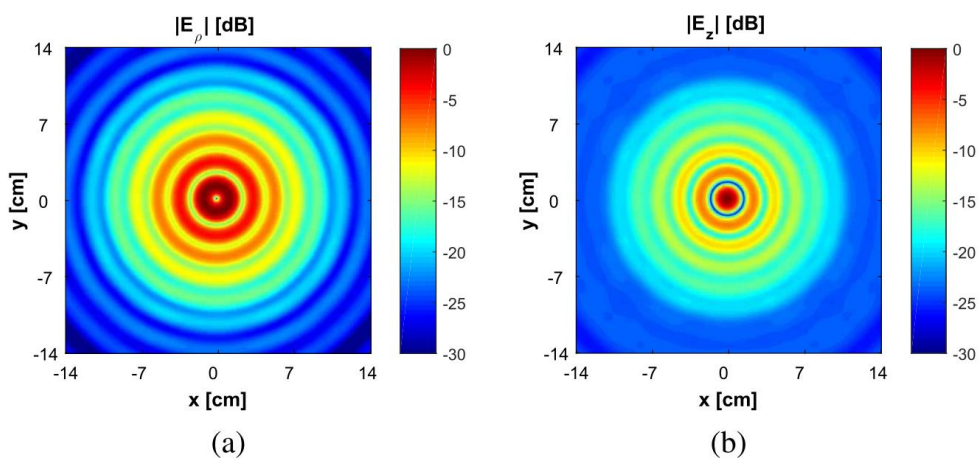
Figure 5.10: Plot of simulated and normalised electric field components (a) E_ρ and (b) E_z at 18.00 GHz in the $x - y$ plane at a distance within the non-diffracting range of 15.50 cm [From [151] © 2018 IEEE]

different distances within the non-diffracting range region for 18.00 GHz. Furthermore, Fig. 5.11(b) shows how the fields diffract when the probe is located beyond the non-diffracting range for that frequency (23.30 cm). As it can be observed, for the 18.00 GHz case (Fig. 5.11(c)) measured results are consistent with the simulated fields for the E_ρ component at 15.50 cm as depicted in Fig. 5.10 (a).
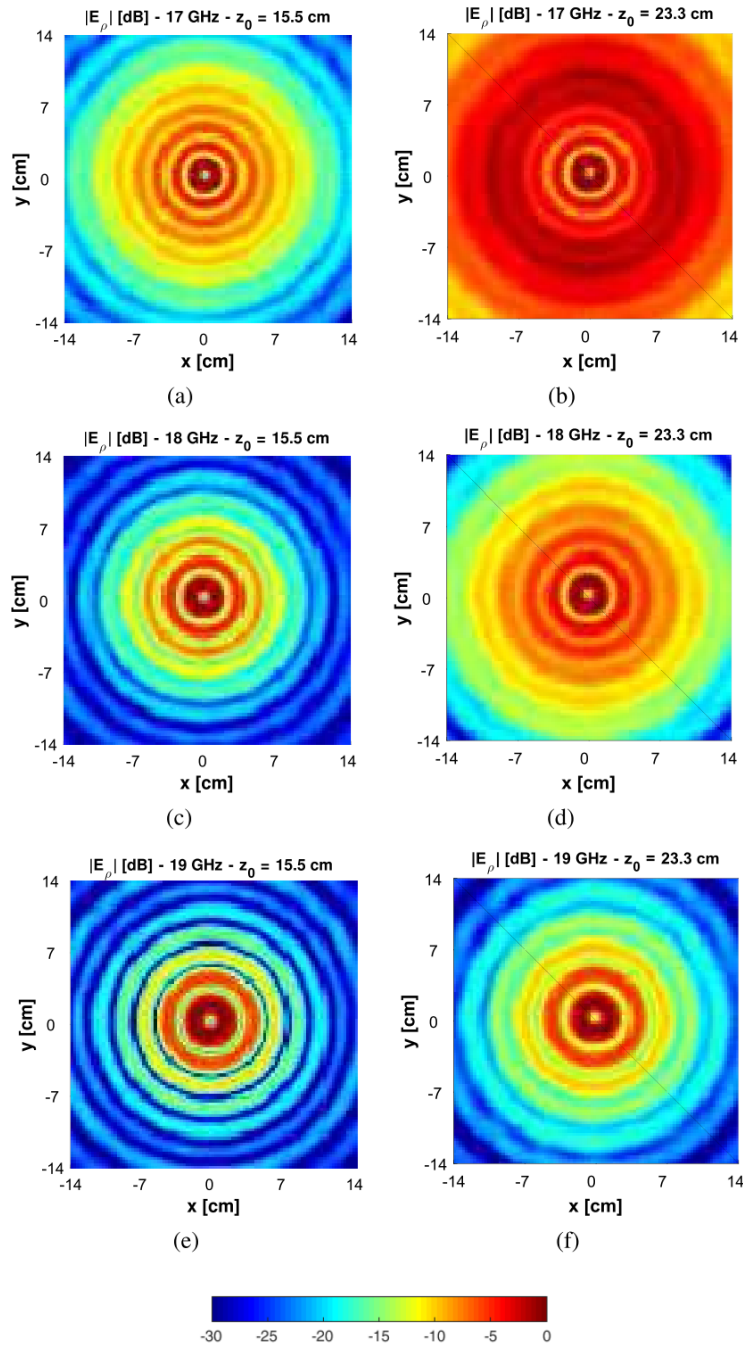
Figure 5.11: Measured and normalised E_ρ transverse component of the electric field in the $x-y$ plane for different frequencies (a) and (b) 17.00 GHz at 15.50 cm and 23.30 cm away from the probe, (c) and (d) 18.00 GHz and (e) and (f) 19.00 GHz [From [151] © 2018 IEEE].

It has been demonstrated that the proposed "bull's-eye" antenna can efficiently produce an omnidirectional conical beam in the far-field steerable along the elevation plane over a wide angular range simply fed by a vertical electric dipole [43, 152]. This structure can be useful for many different applications such as wireless power transfer systems or object-tracking for indoor localisation, while also presenting non-diffracting behaviour in the near-field which could be advantageous for advanced radar system that require near-field data connectivity [43, 151].

5.3 Fabry-Perot Antenna for 2D Beam Steering

The proposed Fabry-Perot antenna is based on the use of the scannable conical beam pattern to synthesise a high directivity pencil beam steerable in 2D which would have similar performance to phased-array antennas with a reduced complexity. The key for this transformation is the feeding method used for this kind of cylindrical leaky-wave antenna. If we used a square or circular array of elementary sources inside the cavity as a feeding network, the beam could be scanned in the azimuthal (phasing the array of sources) and elevation planes (varying the frequency of operation) [45, 150]. This would reduce the number of sources needed improving the system performance in terms of losses while keeping high directivity values.

As shown in Fig. 5.12, the proposed antenna consists of a grounded cavity with a subwavelength partially reflective surface on top. In particular, this partially reflective surface is based on a thin patterned metal plate constituted by a grid of square patches separated by small gaps. Thanks to this design for the partially reflective surface, the geometry presents translational invariance allowing this conical beam to be the element pattern of the phased array. The thickness of the cavity h mainly affects the phase constant of the leaky-wave, i.e., it controls the direction of propagation and the beam shape. On the contrary, the leakage rate primarily depends on the width of the thin gaps between the patches in the partially reflective surface, i.e., for higher directivity thinner gaps would be required as this will reduce the beamwidth [150]. However, this separation is limited by the manufacturing tolerances as extremely thin gaps would required expensive and complex prototyping processes.

Unlike the "bull's-eye" antenna, where the radiation was based on the excitation of
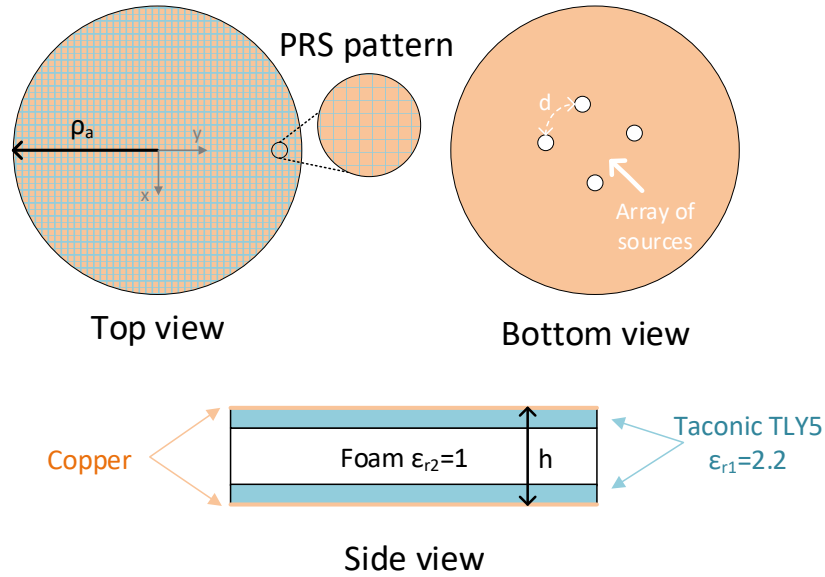
Figure 5.12: Schematic for the proposed Fabry-Perot cavity antenna.

the fast harmonic $n = -1$ of the TM_0 grounded dielectric slab surface-wave mode, the working principle for the Fabry-Perot cavity antenna is the radiation of the fundamental harmonic $n = 0$ of the propagating TM_1 leaky-wave while avoiding at the same time the radiation of the transverse electromagnetic (TEM) mode from the quasi-parallel-plate. For such purpose, the cavity should be filled with foam layers to make the mode a non radiating slow-wave [164]. The excitation of this TM_1 cylindrical leaky-wave with a vertical electric dipole as a simple source results in a highly directive conical beam radiation pattern in the far-field with frequency scanning in the elevation plane [3, 45, 150]. The dispersive analysis for the Fabry-Perot cavity antenna with the is depicted in Fig. 5.13, where it is shown that the TEM mode is a slow-wave (i.e., $\beta_{TEM}/k_0 > 1$) that is not contributing to the far-field radiated pattern while the TM mode is a fast-wave that leaks power mainly defining the radiation pattern.

On the other hand, due to the nature of cylindrical leaky-wave antennas and the vertical electrical dipole source, broadside radiation is not possible in the present configuration. Nevertheless, as explained in Chapter 2, it is possible to radiate at broadside with cylindrical leaky-wave antennas at expense of polarization purity if a magnetic horizontal dipole (e.g., etching slots on the ground plane [89]) is used as a source exciting also the transverse electric (TE_1) mode [107]. When using vertical electric dipoles, the closest the beam is going to scan to broadside is defined by the
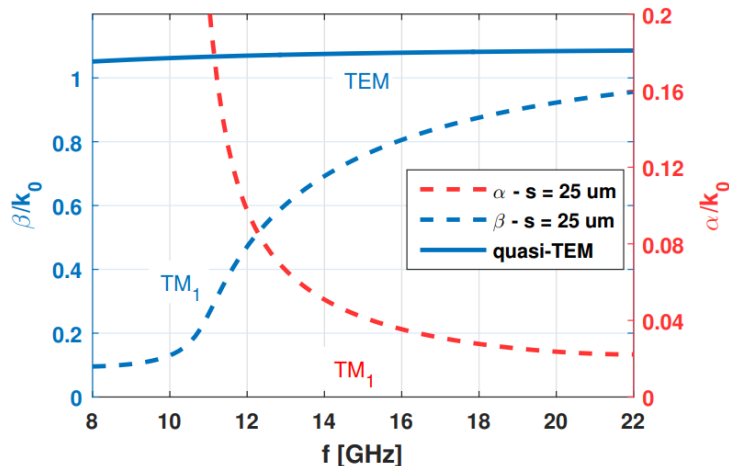
Figure 5.13: Plot of calculated dispersive analysis for the Fabry-Perot cavity antenna. Normalised attenuation constant is described on the left axis while the phase constant is on the right axis. [From [150] © 2018 IEEE].

cutoff frequency ($\beta = \alpha$) of the TM_1 mode. On the contrary, when scanning towards end-fire the highest angle that is possible to realise is limited by the cutoff frequency of the higher order mode TM_2 [150].

Once the conical beam radiation is obtained with the elemental Fabry-Perot cavity antenna configuration, the NxN array of vertical electric dipoles can then be introduced. This array is designed following conventional array theory [145] while also taking into account that each element should be placed at a distance below half-wavelength to minimise grating lobes [150]. Then, the array of sources radiates a pencil beam that points towards a certain direction in the elevation and azimuth planes (θ, ϕ), interfering with the omnidirectional conical beam and transforming it in a directive pencil beam pointing towards the same direction (θ, ϕ) [150]. Thereby, this pointing direction can be controlled in the azimuth plane by simply phasing the array elements, while the elevation plane is steered with frequency.

This design presents very attractive features comparable to those of conventional phased-arrays while reducing the number of sources needed to efficiently feed the system [150] and keeping high directive patterns.
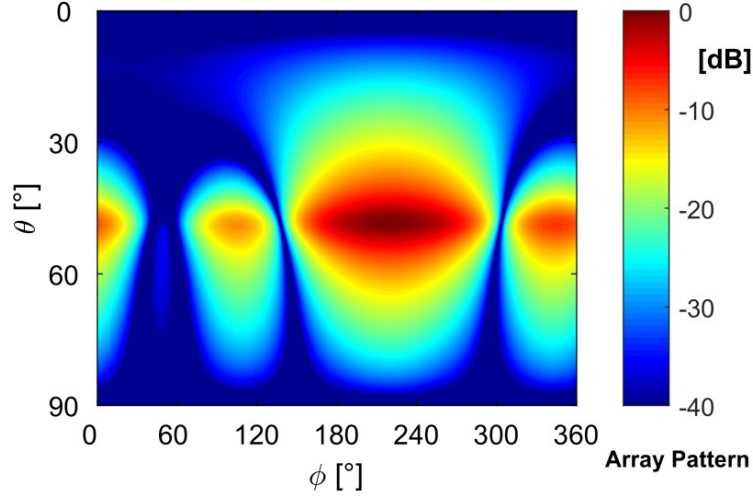
Figure 5.14: Plot of calculated and normalised radiation pattern using 2x2 source elements as a proof of concept, i.e., array feeding, at 15.00 GHz [From [45] © 2018 IEEE].

5.3.1 Antenna Design Considering Single Source Feeding

The proposed configuration is designed for K_u and K bands operation and with a central frequency of 20.00 GHz. Materials used for the cavity are the Taconic TLY5 with a relative permittivity $\varepsilon_r = 2.2$ and foam with $\varepsilon_r = 1$. The parameters are initially set as follows for theoretical and simulated analysis: $h = 14.10$ mm, $\rho_a = 110.00$ mm and $d = 8.00$ mm to avoid the appearance of grating lobes in the array. The homogenised partially reflective surface selected is a grid of square patches whose periodicity is 3.00 mm while the slots between patches are set to 25.00 μm. This gap controls the directivity as it mainly defines the attenuation constant of the fundamental TM_0 cylindrical leaky-wave, which indirectly determines the total radius of the antenna as it is related to the efficiency of the aperture.

The expected radiated electric field component E_θ^{LW} (there is no variation in the azimuthal plane) is calculated following cylindrical leaky-wave theory [107], whereas the array factor $AF(\theta, \Phi)$ is found by classic array theory [95]. Once these two parameters are known, the radiated pencil beam can be easily obtained by [45, 150]

$$F^{array}(\theta, \Phi) = AF(\theta, \Phi)E_\theta^{LW} \quad . \tag{5.3.1}$$

Calculated theoretical results for a normalised radiation pattern phasing 2x2 sources for simplicity to achieve a pencil beam pointing at $\Phi = 220.00°$ and $\theta = 48.50°$ are presented in Fig. 5.14.

5.3.2 Measurement Results

A first design was manufactured and measured as a proof-of-concept. This configuration was based on the use of a single source to confirm the conical beam radiation, which can be used as an element pattern when fed by an array of multiple sources to allow for 2D scanning.

Due to manufacturing tolerances, some parameters were modified, such as the gap between patches, which was increased to $50.00\,\mu$m, and the total radius to $\rho_a = 252.00\,$mm in order to reduce side-lobes in the single source scenario [107]. Furthermore, the probe feed will experience some mismatching when attached to the antenna that needs to be compensated with reactive loading elements in the surroundings. For such purpose, printed metallic elements like a ring of square patches or plated vias are a good candidate. Nevertheless, continuous metallised rings should be avoided as this would introduce resonant microstrip ring modes which could reduce the antenna efficiency. Thus, a ring of vias is the option selected and two extra concentric rings are included to minimise the reflection levels which increases the bandwidth. The manufactured Fabry-Perot cavity antenna is illustrated in Fig. 5.15.

S-parameters for the proposed structure are shown in Fig. 5.16, where reflection coefficient power levels are below -10.00 dB from 18.00 to 23.00 GHz being a 24.39% of impedance bandwidth. Despite the small discrepancies with full-wave simulations
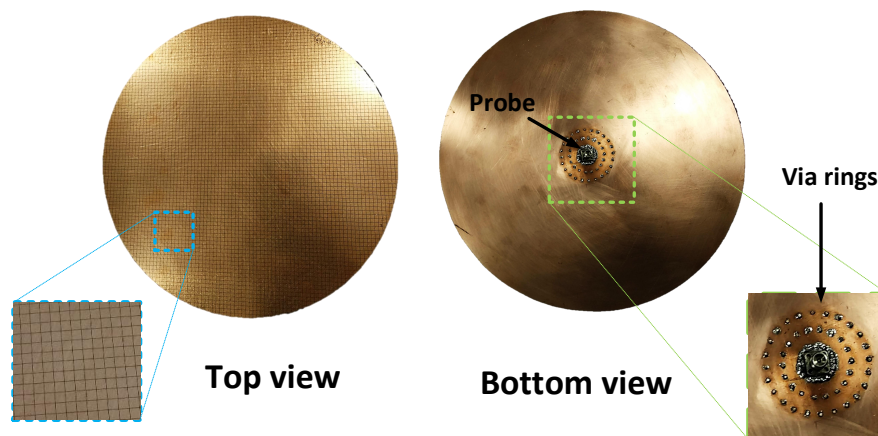
Figure 5.15: Photographs of the manufactured Fabry-Perot cavity antenna illustrating the top and bottom layer considering a single feeding point defining a vertical electric dipole. The partially reflective surface grid is zoomed in the left inset while the feeding configuration is in the right inset.
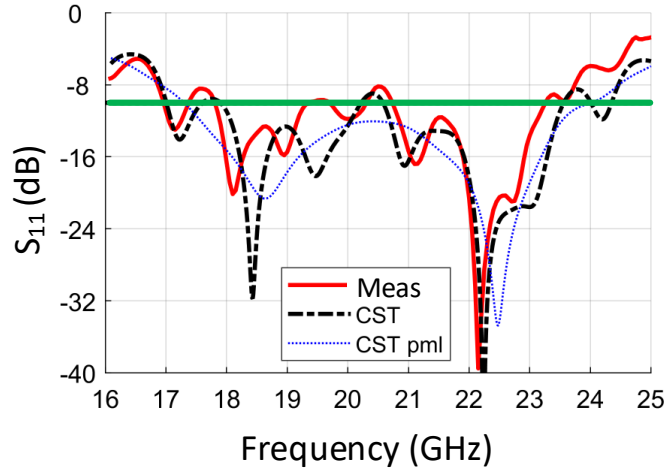
Figure 5.16: Plot of S-parameters obtained for the frequency range of operation. Measured results are depicted in the solid red line, simulations in dashed black line and simulations of the structure using a perfect match layer are shown by the dotted blue line.

due to the via manufacturing process, measured S-parameters are in good agreement with simulated results.

Radiation pattern measurements were obtained in a calibrated anechoic chamber with a far-field equipment. In particular, using a 20240 Flan Standard Horn antenna and the Diamond software to process the data using a rotating positioner for azimuth and elevation sampling. Measured radiated electric fields are depicted in Fig. 5.17 for different frequencies inside the matched range. As expected, a conical shape is obtained in the $x - y$ plane (parallel to the antenna aperture), while frequency scanning is also confirmed. A small offset in the azimuth plane can be observed due to a small misalignment between the prototype and the standard horn causing the beam pattern to not be centred exactly at $\Phi = 0.00°$. However, measured results are still consistent with simulated results.

A cut of the 1D conical beam shape in the far-field for $\Phi = 0.00°$ is also compared to the full-wave simulations at different frequencies. As shown in Fig. 5.18, the truncation of the structure causes the appearance of side-lobes in measured results that are not in the simulations, however they are kept below -10.00 dB and can be further reduced if the radius of the antenna ρ_a is increased.
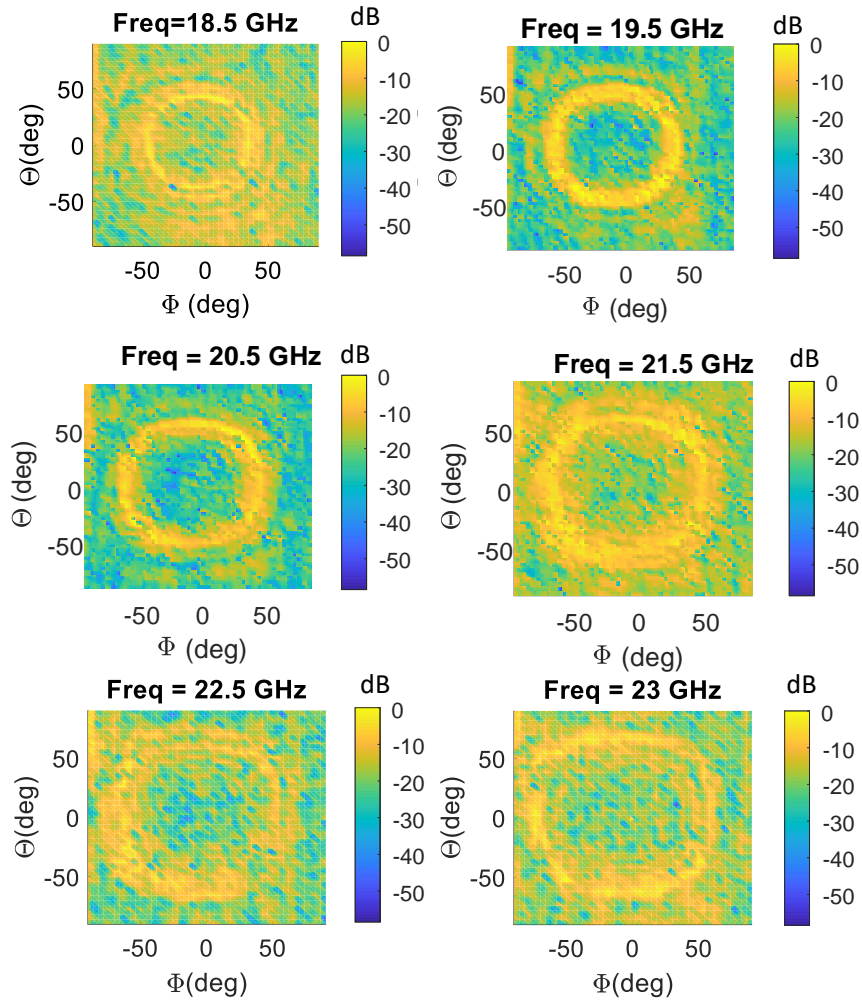
Figure 5.17: Plot of measured $|E_\theta|$ for different frequencies where results are normalised to the observed maximum for each frequency point.

5.4   Summary

Two different configurations exploiting conical beam radiation through cylindrical leaky-waves and their benefits have been presented and experimentally validated in this chapter. Both antenna designs are low-cost and fully planar showing excellent performance suitable for wireless transfer, tracking or advance radar and localization systems for example. A summary of the characteristics for both antennas is reported in Table 5.1.

The "Bull's-eye" antenna results have shown wide angular scanning (from 2.00° to 70.00°), high directivity and an omnidirectional conical beam. Also, its non-diffracting properties in the near-field makes this antenna attractive for such applications and even for next-generation wireless power systems that require power and data transmission, medical imaging, secured communications or advance radars
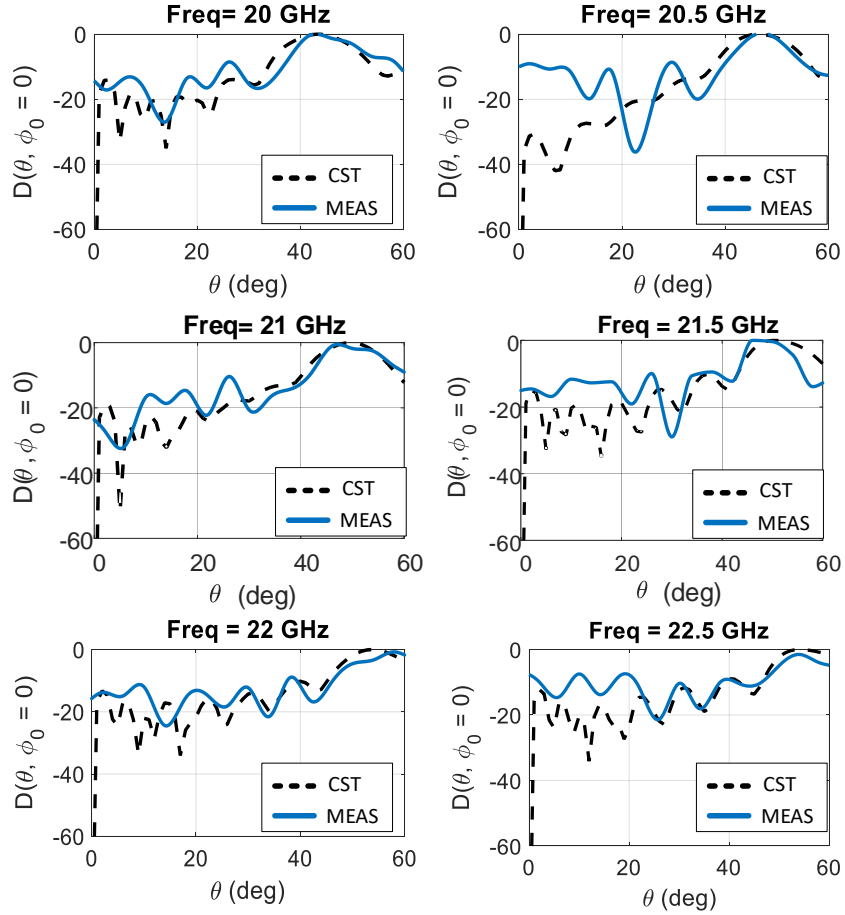
Figure 5.18: Plot of measured and normalised 1D profile for the conical beam at $\Phi = 0.00$ in the far-field for different frequencies compared to simulated results in CST [12].

with near-field data connectivity. It has been demonstrated that high gain values of 20.00 dBi can be obtained using this configuration which implies an improvement of 25.00% with respect to [44] where horizontal magnetic dipoles are used. Moreover, gain values from 10.00 dBi up to 20.00 dBi are kept for a bandwidth of 52.65% demonstrating its wideband behaviour. Simple probe feeding allows to excite the fundamental radial TM_0 mode that is perturbed through the microstrip ring grating becoming a radiative leaky-wave. Side-lobes are also present in the radiation pattern due to the finite aperture of the antenna, nevertheless their influence in the system performance is not critical as values are below -12.00 dB.

On the other hand, for the case of the Fabry-Perot cavity antenna it has been demonstrated that can be used as an element pattern for an array, which in turn can provide enhanced radiation features (in terms of beam steering and enhanced gain) by means of a reduced number of active sources with respect to more conventional array designs. To achieve wideband operational behaviour and to suppress the

Table 5.1: Summary of the Characteristics of the Two Proposed cylindrical leaky-wave antennas

	"Bull's-eye"	Fabry-Perot Cavity Antenna
Scanning plane	Elevation	Elevation-azimuth
Radiation pattern	Conical beam	Pencil beam
Cylindrical leaky-wave mode	TM_0	TM_1
Harmonic	$n = -1$	$n = 0$
Source	Vertical electric dipole	Array of vertical electric dipoles

spurious radiation connected to the excitation of the quasi-TEM mode supported by a partially open parallel-plate waveguide, a multilayer design along with a complete characterisation of its modal features has been introduced. The dispersion of the leaky mode supported by the structure has been designed to provide wideband behaviour together with the feeder that launches the relevant leaky-wave mode within the band of interest. An experimental validation of the wideband operation has been provided. To the best of the Author's knowledge, no similar leaky-wave antennas have been completely studied, designed and experimentally characterised.

Furthermore, the addition of a phased-array of elementary sources suggests a possible 2D scanning in azimuthal and elevations planes with a highly-directive pencil beam from a simple and planar configuration. A conical beam is produced by the excitation of the fundamental harmonic of the TM_1 leaky-wave mode allowing the beam steering in frequency. However, adding the array of elementary sources will introduce scanning capabilities also in the azimuth plane achieving a high directive pencil beam with a reduced number of necessary feed points when compared to conventional phased-array configurations [95]. This structure can also be excited by appropriate arrays of horizontal electric and magnetic dipoles (see for example [89]), in order to achieve dual-polarised conical beam scanning [150].

Chapter 6

Advancements in Leaky Feeder Antennas

6.1 Introduction

Given the limitations provided by leaky feeder antennas in terms of weight, bend radius, poor reception levels for higher frequency systems and the lack of means to distributively control the beam scanning, a more efficient alternative is required for underground and indoor scenarios where wireless communication is necessary. Therefore, in this chapter it is proposed a simple alternative using low-cost planar circuits, radio frequency (RF) switches, patch antennas and standard coaxial cables for WiFi and radio frequency identification (RFID) frequencies that will show better transmitted levels than leaky feeder antennas.

Current distributed antenna systems and leaky feeder antennas do not offer any adaptive and simple switching mechanism to selectively distribute RF power within the coverage area, i.e. the antenna radiation is not directly controlled or programmable along the length of the cable. Moreover, a leaky feeder antenna can present weight and cost restrictions since they are typically heavy and with high maintenance cost [9]. Given this stage of distributed antenna system and leaky feeder antenna technology development, additional research should be encouraged to achieve more adaptive and smart systems for wireless communications and sensor-based data collection. To meet this need, a new type of cable system composed of radiating nodes is proposed, which can provide an alternative to conventional dis-
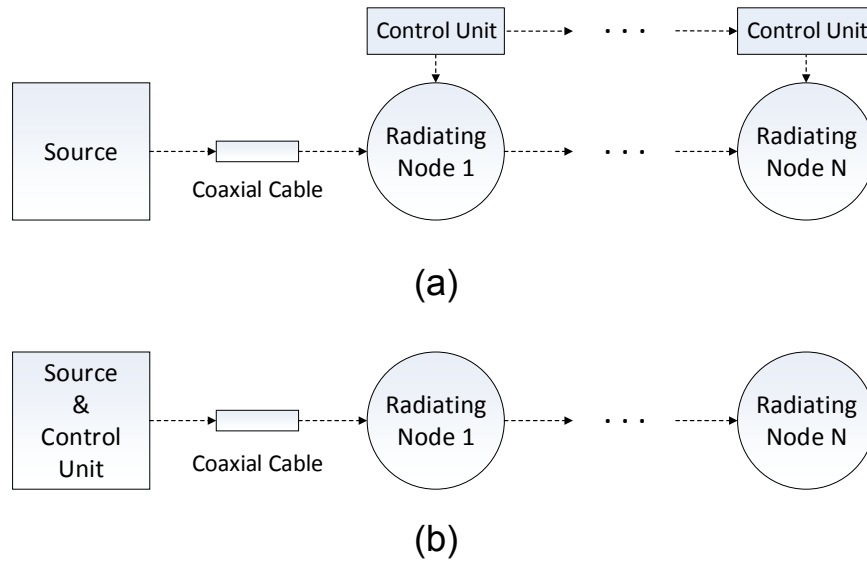
Figure 6.1: Proposed schematic of the smart cable and its radiating nodes defining the controllable distributed antenna system: (a) parallel and (b) series configurations are possible [From [165] © 2018 IEEE].

tributed antenna systems and leaky feeders when designing wireless communication systems within airplanes, tunnels, and subways offering selective communication links, while also allowing for more efficient system performance achieving higher transmitted power levels.

It may be possible for these conventional cable systems, when hybridized with low-cost sensors, printed circuit boards (PCBs), and other wireless technologies [70], to decrease the complexity and the amount of mechanical cable harnessing within an airplane [69, 70]. The proposed cable in this chapter can be a good representation of these hybrid systems, as it is composed of controllable wireless sensors, antennas and planar circuitry, and positioned at specific nodes (see Fig. 6.1). Therefore, the smart cable acts like a distributed antenna system while offering selective antenna radiation and controlled RF coverage. It could replace the more standard, leaky feeder antenna systems or cable-based distribution network with many subcables connected to different wired sensor systems for data collection within airplanes. Other applications of the smart cable include new wireless systems within corridors, tunnels, and subways achieving targeted and selective data communication links, thereby reducing the input power requirements when compared to the leaky feeder antennas.

In the following sections, theoretical approaches for impedance matching and power

distribution will be discussed. Detailed explanations on the design process, full-wave simulations using the frequency domain of CST [12] and measurements will be shown to support the concepts. Moreover, a link budget analysis will be performed for two test case scenarios were the worst situations in terms of power propagation will be examined and a comparison with a commercial leaky coaxial cable will be reported.

6.2 Smart Cable Concept

In general, this smart cable system can be composed of N radiating nodes or hotspots periodically spaced at distances beyond a few wavelengths and connected by standard coaxial transmission lines as illustrated in Fig. 6.1. This cable system allows for the local replacement of any damaged radiating node or coaxial cable section avoiding the manufacturing of a completely new cable as in the case for leaky feeder antennas. Furthermore, our proposed architecture can be implemented with linear or circularly polarized antennas and can be redesigned as needed for the required operating frequency. In addition, our proposed cable system may have each radiating node connected in a parallel configuration or independently (series) as illustrated in Fig. 6.1(a) and (b), respectively. Other topologies are possible, where several smart cables are connected to a power source with independent control units, which is the general term to describe the different elements that could command the radiating nodes (power suppliers, sensors, antennas or circuits elements). Such a programmable network can decide what radiating nodes are to be switched "ON" or "OFF" along the line as required for controlled radiation, enhanced data communications, and reduced transmit powers. To the best of our knowledge such a controllable cable system and its specific components has not been investigated previously.

The cable design has been considered for RFID standards, having a total length of 14.40 m, to be located at the top of a typical corridor, 16.00 m long, at a height of 2.50 m. To ensure uniform coverage at the floor, considering a typical RFID sensor technology receiver sensitivity around -45.00 dBm [166], an available power of 30.00 dBm is required at the cable input. To comply with this received power level requirements, up to five radiating nodes are possible. Moreover, each radiating
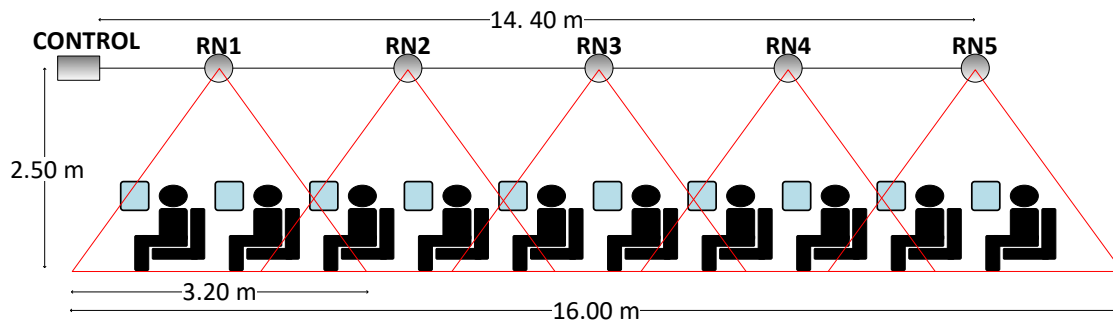
Figure 6.2: Diagram showing radiating node locations in a passenger airplane with system dimensions for the investigated coverage within a corridor. [From [165] © 2018 IEEE].

node is designed to provide a transverse coverage range of 3.20 m for a 2.45 GHz operating frequency. This implies that the antenna at each radiating node should have a half-power beamwidth of 65.00°. The system coverage zone is further depicted in Fig. 6.2.

In order to provide mechanical stability in aeronautical applications, where vibrations and environmental variations can be critical, there are different connectors up to 10.00 GHz that are expected to confront these adverse conditions. Specifically, Threaded Neill-Concelman (TNC) type connectors may be preferred due to their robustness. However, for simplicity, subminiature version A (SMA) connectors have been employed for the presented prototype as proof of concept. These connectors are commonly used with typical American wire gauge (AWG) 7 type cables. Consequently, comparable losses from these cables have been taken into consideration for the system design.

6.2.1 Power Distribution Mechanism

To ensure uniform RF power coverage, the first radiating nodes must radiate a smaller fraction of input power when compared to the subsequent ones. In particular, in our smart cable composed of five radiating nodes, we need the first antenna to receive 20.00% of the power entering the first radiating node, the second one 25.00% of the remaining power and so on. To achieve this unequal power split, non-conventional hybrid branch-line couplers were designed whose layout schematic is shown in Fig. 6.3. The basic operation of this four-port network is that the power entering the input port, 1, is divided between the two output ports, 2 and 4, whereas
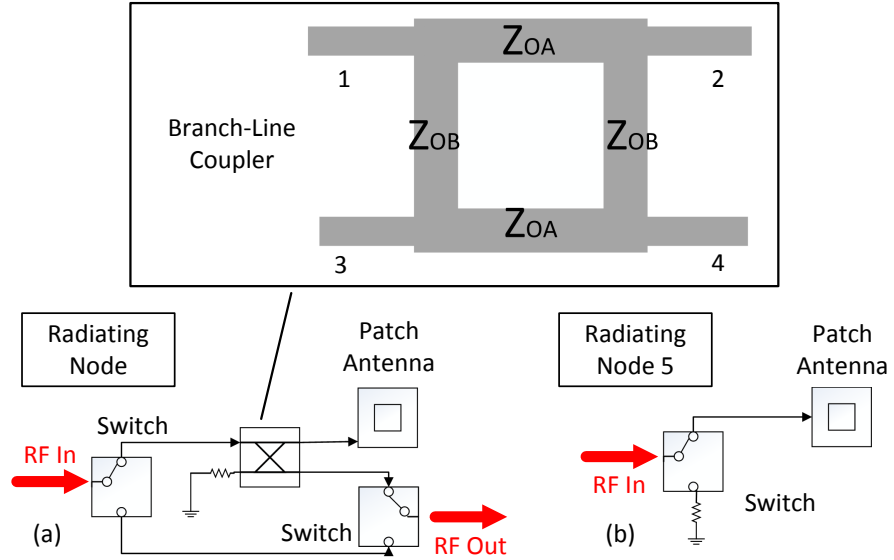
Figure 6.3: (a) Schematic of the first four active radiating nodes with the switches positioned to obtain the "ON" state and the unequal-split branch-line coupler; (b) schematic of the last radiating node in the "ON" state [From [165] © 2018 IEEE].

minimal power is coupled to the isolated port, 3 [102]. By varying the impedance of each pair of the hybrid arms; i.e. by changing the width of the microstrip lines for the fixed quarter wavelength lines, different power split ratios can be obtained. Moreover, if the power ratio between ports 2 and 4 is $K = (P_2/P_4)^{\frac{1}{2}}$ the following equations can be derived.

$$Z_{OA} = Z_O \left(\frac{K^2}{1 + K^2} \right)^{0.5} \quad \text{and} \quad Z_{OB} = Z_O K \,, \qquad (6.2.1)$$

where Z_{OA} and Z_{OB} are the characteristic impedances in Ohms of each pair of branches of the hybrid coupler. Note that to obtain this unequal-power splitting the impedances Z_{OA} and Z_{OB} (see Fig. 6.3) should be different from the characteristic impedance (Z_O) of the microstrip lines connected to the input and output ports of the branch-line coupler. This is due to the fact that, as observed in Eq. (6.2.1), the impedance of the arms of the coupler are only dependent on the desired power split ratio and on the characteristic impedance of the lines connected to the coupler. There is no relation between Z_{OA} and Z_{OB}, therefore having one of these impedances equal to the value of Z_O would result in the typical branch-line coupler with a 3.00 dB power split (equal power split) and not the unequal one required for this system. Making some straightforward calculations, the expressions for equal power split can be obtained with one impedance equal to Z_O.

Being $K = \sqrt{(P_2/P_4)}$, as mentioned above, and setting $Z_{OB} = Z_O$ in Eq. (6.2.1):

$$K = \frac{Z_{OB}}{Z_O} = 1 \tag{6.2.2}$$

This implies that P_2 and P_4 must be equal to satisfy this condition (equal split), therefore replacing K in Eq. (6.2.1) for Z_{OA}:

$$Z_{OA} = Z_O\sqrt{\left(\frac{1^2}{1+1^2}\right)} = Z_O\sqrt{\frac{1}{2}} = \frac{Z_O}{\sqrt{2}} \tag{6.2.3}$$

As demonstrated above, when substituting $K = 1$ or $Z_{OB} = Z_O$, the more conventional equal power split ratio can be obtained for the hybrid coupler, requiring $Z_{OA} = Z_O / \sqrt{2}$.

6.2.2 Radiating Nodes Design

As shown in Figs. 6.3 and 6.4(a), the first four nodes are composed by:

- Two Active RF Switches. They are located one at the input and the other at the output of each unconventional hybrid branch-line coupler. The switches control the power flow depending if the radiating node is turned "ON" or "OFF". For the "ON" case, the power will be diverted to the antenna for radiation through the input switch. In the "OFF" case, the power will continue through a microstrip transmission line to the output switch. At this switch, different amounts of power are received depending on the node state ("ON" or "OFF"), and are delivered to the next radiating node through the connecting cable. The switches used for this implementation are the SKYA21001 model by
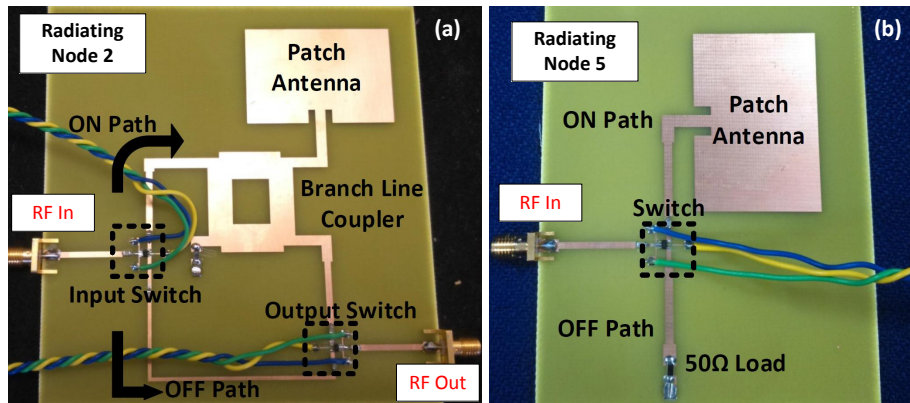
Figure 6.4: Photograph of the manufactured and measured structures: (a) Second radiating node specifically shown here and (b) the last radiating node [From [165] © 2018 IEEE].
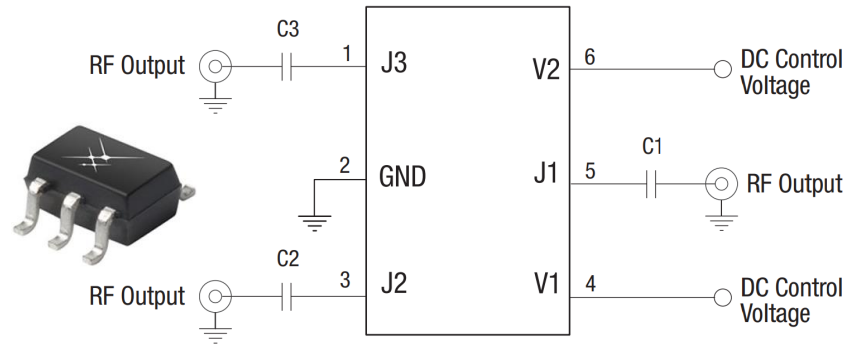
Figure 6.5: Photograph of the SKYA21001 model by Skyworks and its port connection diagram [167]

Skyworks (see Fig. 6.5). To operate these switches, DC power delivered by the control unit is required. This control unit can be different elements, e.g., the same power source, as the DC or low frequency signals can be superimposed to the RF wave to command the switches by means of a DC/DC converter.

As an alternative, the output switch could be replaced by two microstrip lines connected to two separated output ports (one for the "ON" case and other one for the "OFF" case). Nevertheless, the use of these two ports could lead to a complex cable connection and additional unwanted losses for the smart cable system. Also, a preliminary configuration was reported in [168] where the radiating node was designed using a three-port combiner instead of an RF switch at the radiating node output and a series fed patch was proposed (see Fig. 6.6), but higher losses were observed due to the required transmission line lengths in the FR4 PCB material and the patch design.

- The Branch-Line Couplers. As described above by Eq. (6.2.1), the nonconventional hybrids control the fraction of RF power diverted to the antennas. In each coupler, the isolated port is connected to a $50.00\,\Omega$ resistor (port 3), and the output ports are connected to the antenna (port 2) and to the output switch (port 4). The impedance of the transmission line sections of the hybrid couplers is designed depending on the desired power to be delivered to the antenna. Theoretical values obtained with Matlab [10] are then optimized using CST Microwave Studio [12]. The different absorbed power ratios are detailed in Table 6.1 where the calculated and simulated normalized power levels entering the antenna of each radiating node are reported. These power
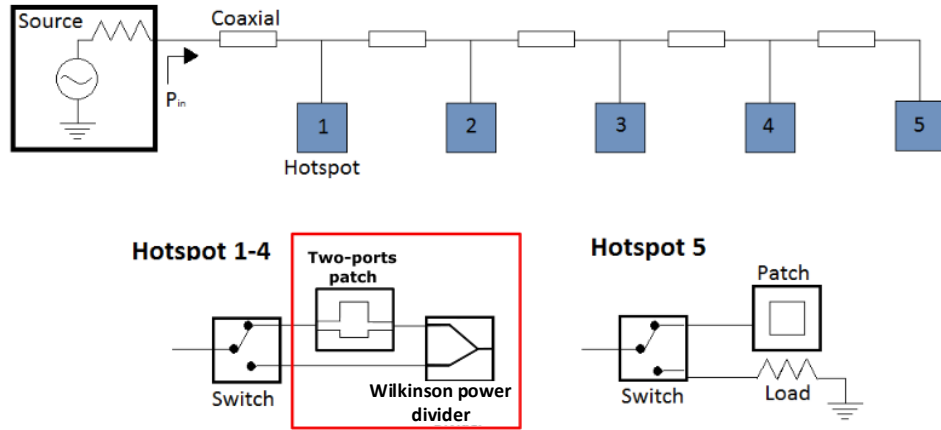
Figure 6.6: Diagram of the initial system design for the smart cable where a series fed patch an a three port combiner were used instead of an RF switch and branch-line couplers [168].

levels will then be radiated with the gain provided by the patch antenna. It should also be mentioned that these original power absorbed values do not take into consideration the insertion losses in each radiating node.

- 50.00 Ω Inset-Fed Patch Antennas. For demonstrative purposes, microstrip antennas are chosen and optimized for 2.45 GHz operation for all the radiating nodes. In addition, linearly polarized (LP) patch antenna configurations are selected for simplicity. Designed patches demonstrated a beamwidth of 94.00° and a gain of 3.00 dBi at the frequency of operation, as shown in Fig. 6.7.

The fifth and last radiating node (see Fig. 6.4(b)), is designed to receive the remaining power of the smart cable. This power will be either radiated by the node antenna or delivered to a 50.00 Ω load if the node is requested to operate in the "OFF" state.

Table 6.1: Relative Power Levels Absorbed by Each Radiating Node (for the Five Radiating Nodes Configuration as in Fig. 6.2)

Radiating Node	Percentage Power Absorbed	Power Absorbed Calculated/Simulated (dB)
1	20.00%	-6.99/-7.01
2	25.00%	-6.02/-6.11
3	33.00%	-4.78/-4.95
4	50.00%	-3.01/-3.44
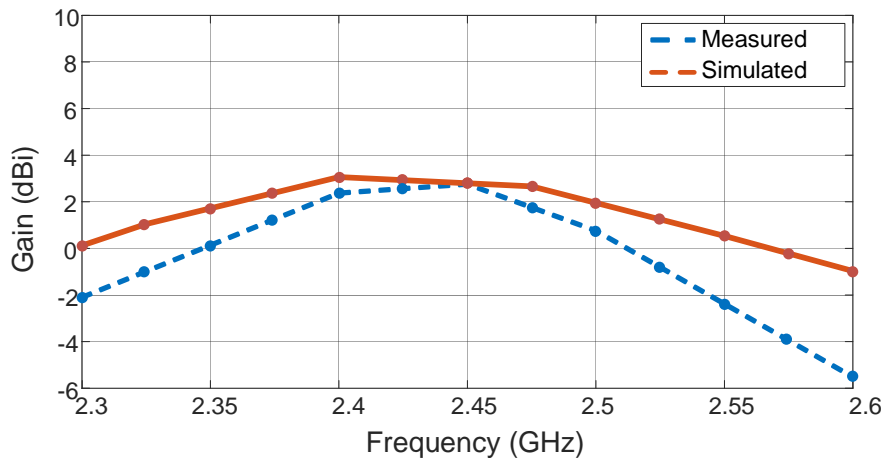
Figure 6.7: Simulated gain levels in CST [12] compared to measurements of the patch antenna.

6.2.3 Implementation of the Branch-line Couplers

The PCBs for the radiating nodes were etched using an FR4 substrate with a relative permittivity of 4.4, $\tan \delta$ of 0.019, and a substrate height of 1.60 mm. These radiating nodes were simulated with the full-wave solver CST [12]. The different branch-line couplers control the power split in each radiating node, therefore their size will be different (wider for the few first radiating nodes) and depend on the required split ratio. For the first radiating node, the desired percentage of power transferred to the antenna is 20.00% of the input power, hence the level of power diverted to the antenna will be about -7.00 dB whereas the level of power diverted to the output of the radiating node will be about -1.00 dB. The impedances required to achieve these split rates are described in Table 6.2. The amount of relative power diverted to the patch and the power diverted for propagation on the transmission line can be observed in Fig. 6.8. The isolation levels are also below -20.00 dB at the design frequency. The stand-alone radiating nodes without the pair of switches were first manufactured and measured. The simulated and measured responses are reported in

Table 6.2: Branch-line Coupler Impedances

Radiating Node	K	Z_{OA} (Ω)	Z_{OB} (Ω)
1	0.50	26.16	27.07
2	0.58	26.20	29.17
3	0.70	28.03	33.70
4	1.00	53.00	38.00
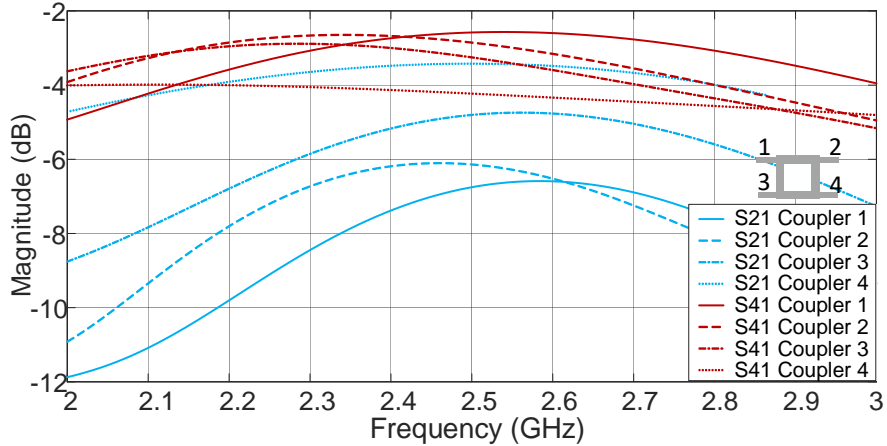
Figure 6.8: Plot of the simulated power diverted to the patch antenna |S21| in CST [12] compared to the power routed for continued propagation on the smart cable |S41| [From [165] © 2018 IEEE].

Fig. 6.9, while theoretical calculations and measurements are compared in Table 6.3 for the first four radiating nodes. The picture of each radiating node PCB, composed of the branch-line coupler and the patch antenna, is shown in the inset of each sub-figure. A good agreement with the simulations is obtained, however a systematic small frequency shift can be observed in the isolation and reflection coefficients; i.e., measured values are about 0.03 GHz higher in frequency when compared to the simulations. This may be attributed to fabrication tolerances and to the fact that the SMA connectors were not included in the simulations. Regardless, expected performance of these passive boards was confirmed by these RF measurements.

6.2.4 Switch Evaluation Board

Once passive radiating node performance was confirmed, active switches were included in the PCBs for final testing. Nevertheless, before assembling these active

Table 6.3: Relative Powers Routed to the Next Node

Radiating Node	Percentage Power Routed	Power Routed Calculated/Measured (dB)
1	80.00%	-1.00/-2.47
2	75.00%	-1.24/-2.65
3	67.67%	-1.76/-3.32
4	50.00%	-3.01/-4.49
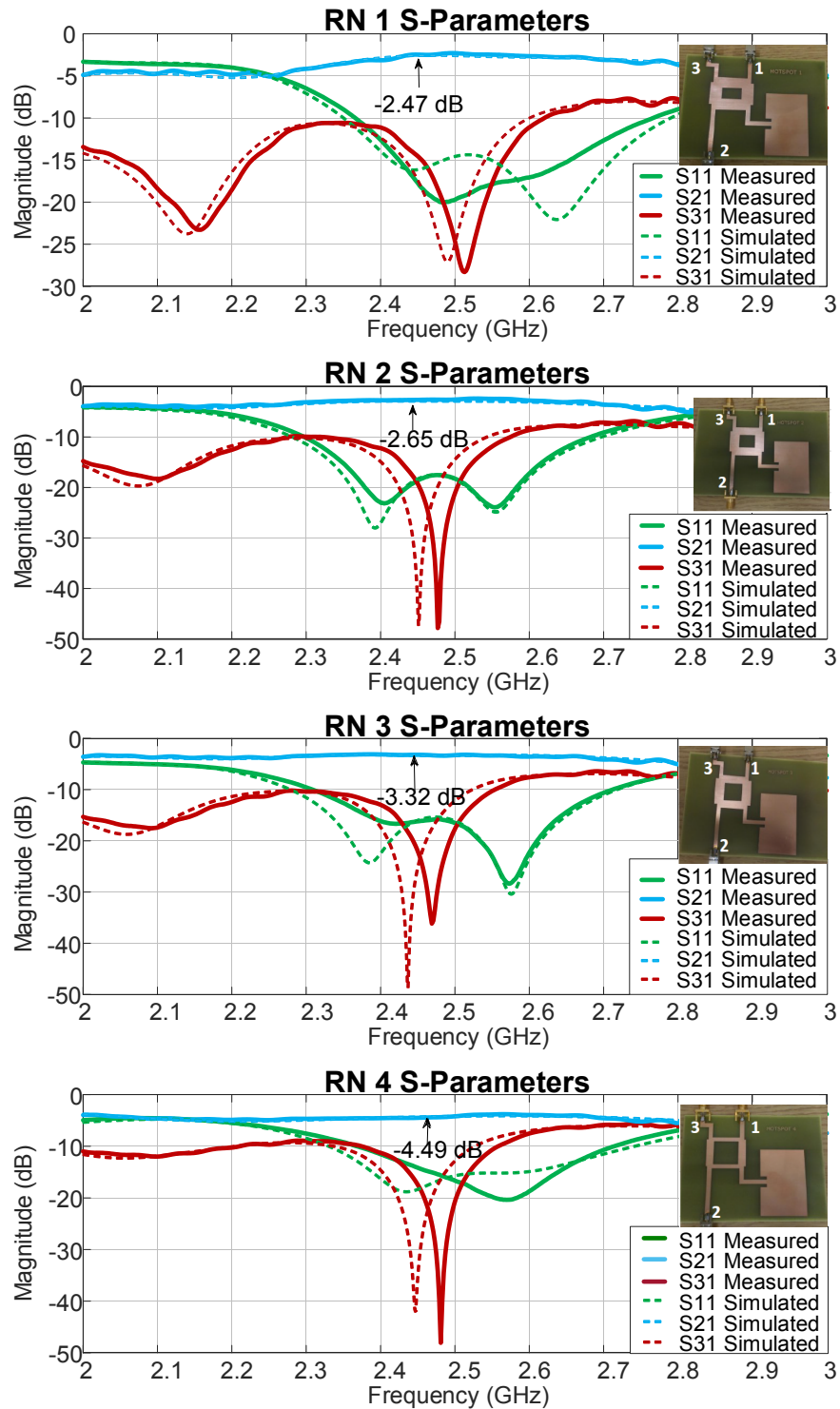
Figure 6.9: Plot of the simulated (dashed line) results in CST [12] and measured (solid line) response for each radiating node. The power directed or routed to the next node is in blue |S21|, whereas the reflection coefficient |S11| and the isolation |S31| are in green and red, respectively [From [165] © 2018 IEEE].

devices, matching sections for microstrip lines needed to be designed to minimize losses on the system due to mismatching with the IC switch and capacitors required to block DC signals entering the switch ports [167].
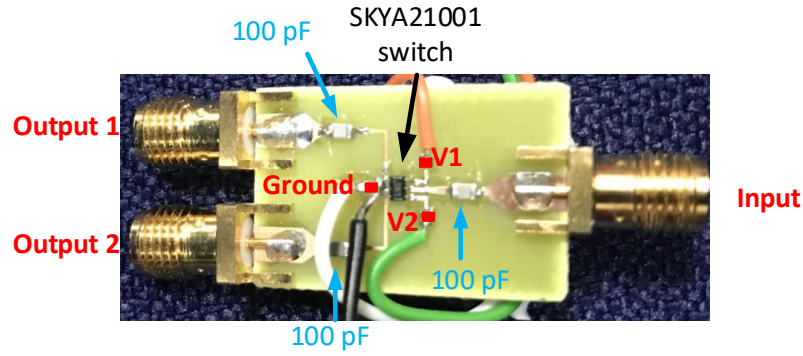
Figure 6.10: Photograph of the first evaluation board prototype for the SKYA21001 switch based on tapered microstrip lines connected to the DC blocking 100 pF capacitors.
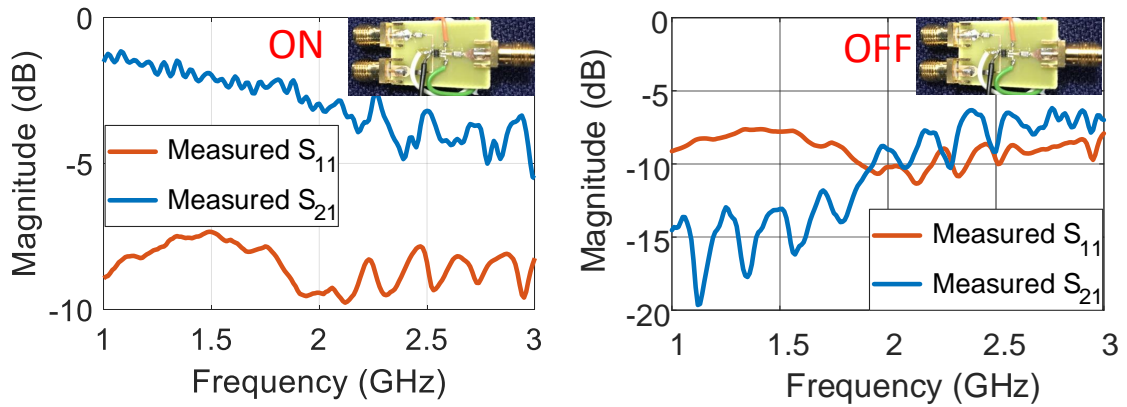
Figure 6.11: Plot of the measured S-parameters for the first switch evaluation board configuration where red lines represent the S_{11} and blue lines the S_{21}; "ON" case (left) and "OFF" case (right).

As depicted in Fig. 6.10, the first approach was to use tapered microstrip lines as a smooth transition from the $50.00\,\Omega$ transmission lines width to the required capacitors size. However, as shown in Fig. 6.11, this configuration seriously compromised the performance of the switches providing a transmission coefficient below -4.00 dB for the "ON" case and -7.00 dB for the "OFF" case.

The main problem observed was that the size of the input and output microstrip lines was much higher than the expected for the ones connected to the capacitors, therefore tapered microstrip lines were not the best solution for this system. Instead, quarter wavelength transformers were designed, as depicted in Fig. 6.12, and its performance provided better transmission power levels for the radiating nodes taking into account the 0.40 dB insertion losses due to the switches themselves.
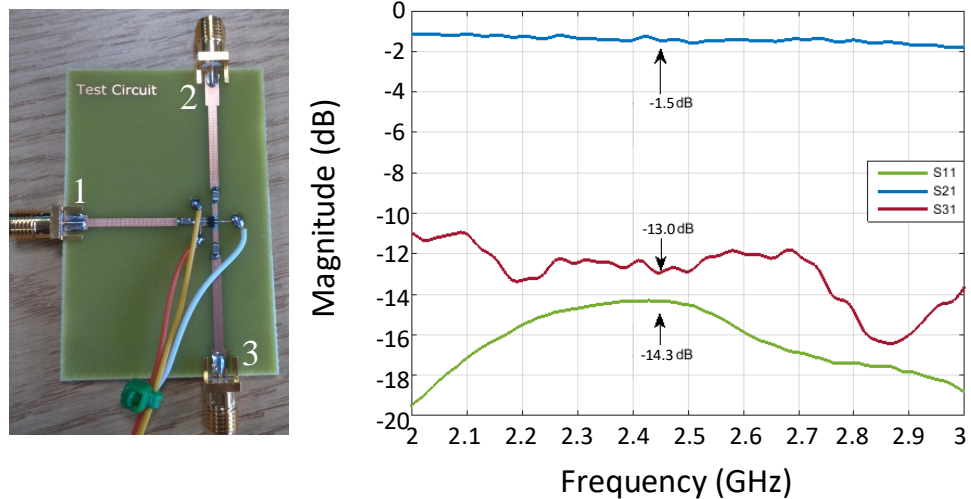
Figure 6.12: Photograph of the manufactured prototype (left) and plot of measured S-parameters for the second switch evaluation board configuration based on the designed quarter wavelength transformers when output 2 is activated. The $|S_{11}|$ is represented in green while the active output $|S_{21}|$ is in blue, in addition red line, $|S_{31}|$, shows the residual power levels going through the inactive output 3.

6.2.5 Active Radiating Nodes Prototype and Measurements

Measurements of the active radiating nodes show a good agreement with the expected results, as observed in Fig. 6.13. This is also true for the antenna gain and radiation performances of the active radiating nodes, which were measured with the three antenna test method in the far-field [155]. In this gain comparison method, two pre-calibrated standard gain antennas, in our case the Standard Horn 08240 from Flann, are used to determine the absolute gain of the desired antenna by means of different gain measurements to formulate a set of three equations with three unknowns by simple calculations using Friis free-space formulation [155].

As shown in Fig. 6.13, the power is routed to the next radiating node with a relative power level of -4.90 dB and of -2.80 dB, in the "ON" and "OFF" switch states, respectively. Conversely, if the input and output switch definitions differ from the "ON" and "OFF" radiating node states (for example, if the input switch is set for the "ON" state while output switch set for the "OFF" state), negligible power is delivered to the next radiating node. More specifically, less than -17.00 dB for the unconnected "OFF" path and about -35.00 dB for the unconnected "ON" path.
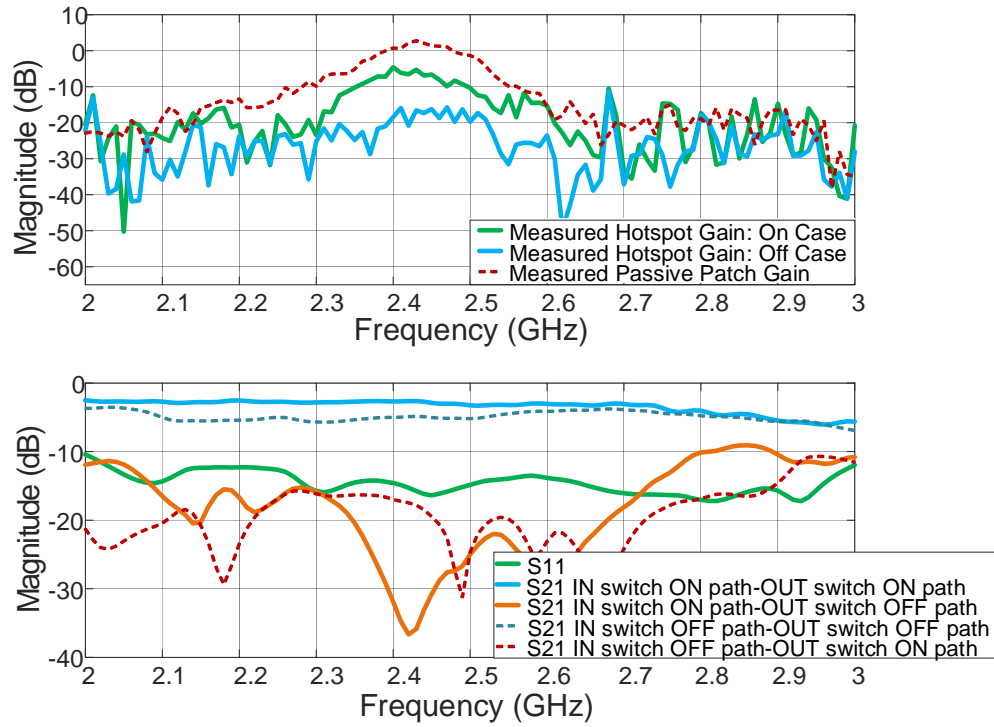
Figure 6.13: Plot of (a) measured active radiating node 2 gain for the "OFF" and "ON" states and for the stand-alone patch antenna; (b) measured S-parameters for radiating node 2 (the active radiating node circuit is shown in Fig. 4(a)) [From [165] © 2018 IEEE].

Regarding the far-field gain, it can be observed that the passive patch antenna has a typical gain of about 2.00 dBi using FR4. Moreover, if the "ON" case is activated the power is being radiated by the node with a gain greater than -5.00 dBi due to substrate losses, but for the "OFF" case the gain is about -17.00 dBi since the majority of the power is transferred to the next radiating node. The gain value in the "ON" case can be improved simply by modifying the antenna design for each radiating node or selecting a higher quality PCB substrate with less dielectric loss, rather than FR4, for each radiating node.

6.3   Radio frequency Identification Application

Considering the possible RFID application and data collection between a radiating node and a tag; once the signal is received by the tag, the backscattered signal would be sent back to the radiating node patch antenna. In this case, the most important part is the design of the control unit, as it will command the smart cable to be in the sending or in the receiving configuration or in both.
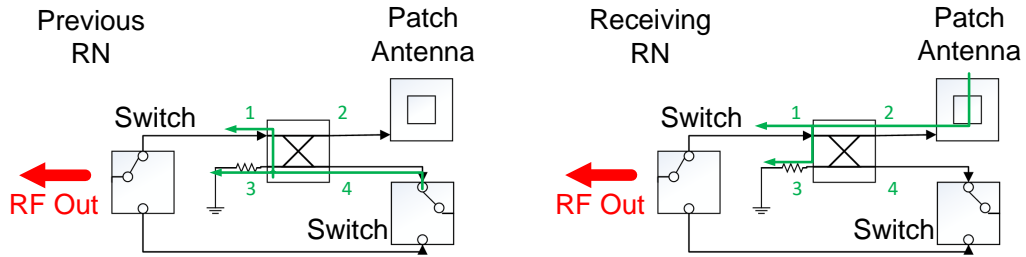
Figure 6.14: Diagram of the receiving node (right) and the paths that the signal will follow are lined in green; diagram of the previous radiating node (left), showing where the signal would come from and what path it would take.

The control unit design and behaviour is not relevant to the smart cable design, as it depends on the topologies selected and on the different possible applications. Although, as a general description, the following could be stated:

- As the most restricting sensitivity is the one of the tag, it is assumed that the radiating nodes would be able to receive the backscattered signals. Nevertheless, as the power received will be low, low noise amplifiers would be required in the control unit in order to process the information received.

- In the simplest case of the smart cable configuration, switches would be all in the "ON" state during the receiving mode to allow all the radiating nodes to receive and pass along the signal received from the tags. Additionally, sensors could also be included on the radiating nodes, but the proposed design in this thesis is just a simple proof of concept.

In terms of radiating node performance, branch-line couplers are reciprocal structures [102], therefore the signal would be carried in the inverse direction; i.e., port 1 and port 3 being the new outputs, and port 2 and port 4 being the new inputs (see Fig. 6.14). Then port 4 of the coupler would be the input for the previous radiating nodes placed between the receiving radiating node and the control unit, while port 2 would be the input when the signal is being received at that radiating node. In the simplest case of the smart cable configuration, all the switches would be in the "ON" state to allow power flow. Therefore, depending on the total power levels received at the control unit, the receiving radiating node could be detected due to the different levels expected from each radiating node. If we take for example a received power level of 0.00 dBm at the last radiating node and apply the split ratios and coaxial cable losses in each radiating node, the power received in the

control unit would be around -10.27 dBm while if the receiving node is the second radiating node the power would be -3.18 dBm (see Table 6.4). Nevertheless in more specific systems, the control unit could be chosen so the switches could be activated or deactivated on demand.

Table 6.4: Estimated Power Levels on Different Radiating Nodes in Reception Mode

Receiving Radiating Node (% Diverted to Coupler Output)	Power at Node 5 (dBm)	Power at Node 4 (dBm)	Power at Node 3 (dBm)	Power at Node 2 (dBm)	Power at Node 1 (dBm)	Power at Control Unit (dBm)
5 (100.00%)	0.00	-4.05	-6.45	-8.34	-9.94	-10.27
4 (50.00%)	-	-3.01	-5.41	-7.30	-8.90	-9.23
3 (33.00%)	-	-	-1.76	-3.65	-5.26	-5.58
2 (25.00%)	-	-	-	-1.25	-2.86	-3.18
1 (20.00%)	-	-	-	-	-0.96	-1.29

6.4 Estimated System Performance

Given the reported measurements of the radiating nodes in the previous section, an estimation can be made for the smart cable system indoor performance with five series nodes operating at 2.45 GHz and considering an available input power of 30.00 dBm at the smart cable input. Two test cases are considered for general indoor RFID sensor applications in Table 6.5 with a cable length as in Fig. 6.2. Comparisons are then made with a commercial leaky feeder antenna [169] and are shown in Table 6.6.

6.4.1 Two Scenarios for System Performance Assessments

Test Case Scenario 1 - Only the Last RN Radiates

The losses that have to be taken into consideration are due to the AWG 7 type coaxial cable (0.20 dB/m), the last radiating node switch (0.40 dB), and the losses due to each radiating node in the "OFF" state (2.80 dB). Therefore, the power transferred to the last antenna in this case is about 15.00 dBm of which 10.00 dBm is radiated. Thus, considering a passive RFID tag with 0.00 dBi gain and accounting for free-space path losses, the power received at the RFID tag location (illuminated by the last radiating node) would be about -39.00 dBm 2.90 m away from the cable, which, as mentioned previously, satisfies tag sensitivity requirements [166].

Table 6.5: Power Levels on the System for 30.00 dBm Input Power

Radiating Node	Test Case 1 (dBm)	Test Case 2 (dBm)
1	29.68	29.68
2	26.24	24.27
3	22.80	18.58
4	19.36	12.38
5	15.92	4.93

Test Case Scenario 2 - All Nodes Radiate

In this case, a fraction of power is radiated by each radiating node, thus the power remaining at the end of the smart cable is much lower than in Scenario 1. Losses considered here are the same as above, except for the losses due to the "OFF" path, which are replaced by the ones incurred in the "ON" path for each radiating node (1.90 dB). The power getting to the last radiating node is about 4.90 dBm of which 3.00 dBm is transferred to the antenna. Now considering a gain of 0.00 dBi for the passive RFID receiver tag, the power level at the furthest distance from the ceiling (2.90 m) is about -46.00 dBm, which is still compliant with RFID technologies sensitivities [166].

Obtained power levels in these cases are presented in Table 6.5. The two scenarios achieved suitable power levels for RFID applications and thus the smart cable would be able to ensure coverage along the specified corridor example (see Fig. 6.2). For low sensitivity requirements at the tag side, some design enhancements could be considered for the radiating nodes such as an active switch with improved isolation (>25.00 dB) when compared to the SKYA21001 RF switch model.

6.4.2   Leaky Feeder Antenna Comparison

A study of the received power is provided in Table 6.6, which compares the proposed smart cable system to the performance of a commercial leaky feeder antenna [169] operating at 2.40 GHz. These calculations have been done for the Test Case Scenario 2, when all the radiating node are activated, as this would be the case with the highest amount of losses.

The receiver is set to be 2.00 m below the cable where leaky feeder antenna coupling

Table 6.6: Estimated Power Received for an Input Power of 30.00 dBm

Distance (m)	Smart Cable (dBm)	Leaky Feeder 50.00% (dBm)	Leaky Feeder 95.00% (dBm)
1.60	-25.45	-66.26	-76.26
4.80	-29.89	-66.75	-76.75
8.00	-34.33	-67.49	-77.49
11.20	-38.77	-68.98	-78.98
14.40	-43.21	-71.96	-81.96

losses are typically measured, as described in [170]. Two coupling loss values are provided for the 50.00% and 95.00% of reception probability. Therefore, two different calculations are shown for the leaky feeder antenna comparison in Table 6.6, which represents the performance of the leaky feeder antenna in both cases. In this study the receiver moves a distance along the cable at a fixed height of 2.00 m. Calculations start at the distance where the first radiating node is placed and at the last radiating node position. Commercial leaky feeder antenna longitudinal losses are 0.14 dB/m while coupling losses, which are a consequence of the two possible modes for an leaky feeder antenna (radiating and coupling), are 66.00 dB and 76.00 dB for 50.00% and 95.00% of reception probability, respectively. It can be observed that an improvement of at least 30.00 dB of received power while using the same amount of input power is possible by using the proposed smart cable configuration.

6.5   Summary

Due to the limitations presented by leaky feeder antennas in modern wireless communication systems, a simple and efficient alternative has been presented in this chapter. This new smart cable composed of radiating nodes, which uses active RF switches, was proposed for wireless sensor and communication applications. It offers simple and controlled radiation and RF power distribution, and good integration with active elements for "ON"/"OFF" switching to enable selective data communication links. Appropriate design of the non-conventional branch-line couplers for each radiating node is essential for efficient system performance. The minimum amount of power radiated in each radiating node ensures an adequate coverage

along the floor satisfying RFID sensitivity requirements.

It has been demonstrated that by means of selecting the amount of power leaked in each radiating node, an average improvement of 34.33 dB in transmitted power levels when compared to those at the leaky feeder antenna case can be achieved for communications inside corridors, tunnels or subways. Particularly, a transmitted loss reduction of 49.72% and 56.15% can be observed for 50.00% and 95.00% of reception probability respectively. Given the radiating node characteristics, the smart cable is also simpler to design, manufacture and maintain. More importantly, the proposed cable design and active radiating nodes represents a new innovation for wireless data connectivity within underground and indoor scenarios, while also enabling new cable systems which are smart, low-cost, programmable and more flexible than other existing technologies such as distributed antenna systems and leaky feeder antennas typically used in these scenarios.

Chapter 7

Conclusions

7.1 Thesis summary

This thesis has covered the design of configurations that can mitigate some of the issues that leaky-wave systems encounter nowadays. The focus has been on feeding networks and selective distributed indoor communications. Three feeders based on surface-wave, leaky-wave and vertical electric dipole concepts have been introduced. Moreover, it has also been proposed an alternative consisting of broad-beam distributed antennas to ease weight constraints on airplanes where leaky-wave antennas fail to be an efficient and low-profile solution for selective beam scanning at microwave frequencies. It has been demonstrated throughout the chapters that low-cost and fully planar implementations can be achieved for modern communications systems.

As a summary, a list of contributions is presented in Fig. 7.1, where the different proposed designs features are presented. The structures are introduced in order of appearance, starting from the surface-wave launcher from Chapter 3 [117], then the leaky-wave launcher from Chapter 4 [85, 128], followed by the bull-eye and Fabry-Perot cavity from Chapter 5 [43,45] and finishing with the smart cable from Chapter 6 [165, 168].
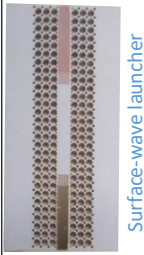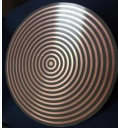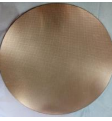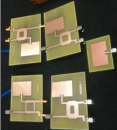
	Layer	Frequency band	Improvements	Impedance bandwidth	Launching efficiency / Gain	Size (WxLxH)	ε_r
CH. 2 Surface-wave launcher	Single	K and K_a	Compactness, wideband, full integration	74.29%	60.00%	$1.4\lambda_0 \times 1.7\lambda_0 \times 0.5\lambda_0$	10.2
CH. 3 Leaky-wave launcher	Single	K_u	Compactness, efficiency, wavefront stability	0.30%	88.00%	$3.9\lambda_0 \times 2.2\lambda_0 \times 0.04\lambda_0$	2.2
CH. 4.1 Bull's eye antenna	Single	K_u-K_a	Gain, wideband, compactness	42.10%	30.00 dBi	$9.3\lambda_0 \times 9.3\lambda_0 \times 0.2\lambda_0$	2.2
CH. 4.2 Fabry-Perot Cavity antenna	Multi-Layer	K	Compact feeding, wideband, allows for 2D scanning	26.82%	10.00 dBi	$7.5\lambda_0 \times 7.5\lambda_0 \times 0.9\lambda_0$	2.2
CH. 5 Smart cable	Single	S	Selective transmission, low-profile, high transmission power	16.32%	2.30 dBi	$0.5\lambda_0 \times 0.6\lambda_0 \times 0.01\lambda_0$	4.6

Figure 7.1: Summary of the structures proposed in this thesis.

Firstly, in Chapter 2 the literature review and theory background have been discussed. It can be concluded that leaky-wave antennas have been significantly investigated in the literature during the last few decades, being extremely useful for planar and low-cost electrical beam steering applications. Moreover, leaky-wave antennas features include flexibility for implementation in different technologies such as dielectric image guides, SIIGs or Fabry-Perot cavities, being a reliable solution for higher frequency bands where other common technologies, such as microstrip, fail to provide good performance. Leaky-wave antennas not only show competitive features for modern applications but offer unique scanning capabilities that would require otherwise an involved design process using other kind of antennas.

Issues that motivated this research and that can be found when using modern leaky-wave antennas have been introduced. The focus is established on feeding networks, planar configurations for conical beam radiation and alternatives to bulky leaky feeders for indoor communications. When analysing the current feeding networks based on surface and leaky-wave launchers, complex, lossy or expensive configurations are found. Similar occurs to 2D leaky-wave antennas that become bulky multilayer structures for conical beam radiation. In the case of indoor communications for WiFi or RFID configurations, leaky feeders are employed which do not allow for selective distributed transmission. This can lead to unnecessary losses that are critical given the restrictive sensitivities for these applications. The theory necessary to understand the designs that have been presented was also explained.

In Chapter 3 a review of the conventional guided-wave theory needed for surface-wave excitation by parallel-plate waveguide truncation on grounded dielectric slabs and rectangular grounded dielectric slabs to implement feeding systems for leaky-wave antenna applications has been presented and analysed. By the inclusion of an additional partially reflective surface after this truncation acting as a matching network, a high efficiency surface-wave launcher has been created. The launcher has been designed using a common grounded dielectric slab and surface-wave theory, where design parameters can easily be tuned for the desired system performance. As a proof of concept, the proposed launcher has been implemented to excite a leaky-wave antenna on a rectangular grounded dielectric slab for K and K_a bands. It has then been designed for the technologies of interest such as dielectric image guides or substrate integrated image guides (SIIG), where bulkier or complex feed-

ers are commonly used. Simulated results obtained using a commercial full-wave simulator CST [12] with the frequency domain solver have also shown its wideband and efficient behaviour. However, special attention should be given to the feeding network as for thick and high permittivity dielectrics the performance of the system is affected by the attachment of RF connectors to the microstrip line, instead probe feeding is preferred although frequency bandwidth will be sacrificed. The new and simple presented approaches have been demonstrated to be low-cost and a compact way to excite leaky-wave antennas by uniform surface-wave excitation. This work has demonstrated an increased bandwidth of up to 90.50% when compared to the literature and a reduced volume of more than 98.66%.

Following the studies on efficient antenna excitation, Chapter 4 introduces the application of leaky-wave concepts to create a simple launcher for slot array antennas. Specifically, in this chapter a novel launcher has been proposed using these concepts to excite the fundamental parallel-plate waveguide transverse electromagnetic (TEM) mode by means of a leaky T-junction implemented in SIW technology for uniform feeding in slot antenna array systems. This design procedure allows for uniform and bound propagation at broadside (with respect to the leaky SIW side wall) within the parallel-plate waveguide region. Moreover, a transverse resonance equation analysis has been carried out to determinate the parameters needed for such a configuration, while full-wave simulations have also been employed to assess the expected performance. These theoretical, simulated and measured results have been presented and then compared showing good agreement and performance for the introduced structure. When compared to previous configurations found in the literature, this launcher provides a size reduction of up to 61.56% and a more uniform wavefront showing up to a 85.00% more stable phase and amplitude. Moreover, the launching efficiency achieved by this launcher is a 44.44% higher than previous topologies. Furthermore, it has also been demonstrated that by the addition of the matching section used in the Chapter 3, this structure could also be implemented as a surface-wave launcher or an end-fire antenna itself as well. This compact SIW-to-parallel-plate waveguide transition maintains a low profile for simple fabrication and offers 50-Ω microstrip feeding.

On the other hand, in Chapter 5 the use of two-dimensional (2D) periodic leaky-wave antennas to excite cylindrical leaky-wave applied to new configurations for efficient

conical beam propagation and beam steering. This work has been carried out in collaboration with La Sapienza University (where the author had a 4-months research exchange) where the joint effort aimed to provide competitive alternatives to improve the state-of-the-art for advanced radar systems, medical imaging or wireless communication applications. As a result, two novel prototypes showing conical radiation have been theoretically analysed and simulated by the team in La Sapienza, those results have also been introduced for clarity and completeness, whereas the prototyping and measurement process have been carried out at Heriot-Watt University where measurements and simulations were compared to the theoretical findings. Practical experiments and manufacturing processes developed by the author have been reported in detail throughout the chapter. Additionally, a comparison between the two proposed antennas has also been provided assessing the key differences that made them suitable for different applications. More specifically, the "bull-eye" configuration was able to achieve non-diffracting radiation in the near-field and omnidirectional conical beam steering in the far-field with higher gain values up to 25% when compared to previous studies. On the other hand, for the case of the Fabry-Perot cavity antenna it has been demonstrated that can be used as an element pattern for an array, which in turn can provide enhanced radiation features (in terms of beam steering and enhanced gain) by means of a reduced number of active sources with respect to more conventional array designs. To achieve wideband operational behaviour and to suppress the spurious radiation connected to the excitation of the quasi-TEM mode supported by a partially open parallel-plate waveguide, a multilayer design along with a complete characterisation of its modal features has been introduced. The dispersion of the leaky mode supported by the structure has been designed to provide wideband behaviour together with the feeder that launches the relevant leaky-wave mode within the band of interest. An experimental validation of the wideband operation has been provided.

In Chapter 6, an alternative to the commonly used leaky feeder antenna for RF propagation in indoor scenarios has been presented and validated. The proposed smart cable is intended to improve the performance for power distribution systems and data communications in the aforementioned scenarios using different passive and active elements. Detailed explanations on the design process has been provided, as well as simulations and measurements to support the idea and show proof of concept.

Moreover, a budget link analysis for two test case scenarios have been examined proving that even in the most lossy conditions the smart cable will still comply with reception sensitivities for radio frequency identification (RFID) applications, being applicable to WiFi and other wireless communication standards. This new smart cable has been designed using radiating nodes, which uses active RF switches to offer simple and controlled radiation, power distribution, and good integration with other active elements. It has been demonstrated that by means of selecting the amount of power leaked in each radiating node, an average improvement of 34.33 dB in transmitted power levels when compared to those at the leaky feeder antenna case can be achieved for communications inside corridors, tunnels or subways. Particularly, a transmitted loss reduction of 49.72% and 56.15% can be observed for 50.00% and 95.00% of reception probability respectively. Given the radiating node characteristics, the smart cable is also simpler to design, manufacture and maintain. More importantly, the proposed cable design and active radiating nodes represents a new innovation for wireless data connectivity within underground and indoor scenarios, while also enabling new cable systems which are smart, low-cost, programmable and more flexible than other existing technologies such as distributed antenna systems and leaky feeder antennas typically used in these scenarios.

7.2 Future Work

The proposed implementations offer many advantages but also many possibilities for future improvements or new structures. Next, a list of future work for each system is reported:

- Surface-wave launcher for leaky-wave antennas

  The following step for this launcher would be to fill the air gap with dielectric glue in order to improve the impedance matching response. Furthermore, the use of better connectors to improve the response in microstrip input configuration can lead to a wideband launcher useful for many applications. Moreover, this launcher can also be the base for more complex surface-wave-routing structures, such as new passive circuits or curved dielectric image guides and SIIGs.

- Leaky T-junction

This parallel-plate waveguide TEM planar launcher can be re-designed using different permittivity substrates and when considering operation at higher millimetre-wave frequencies. Also, to overcome the narrowband behaviour of the structure a double layer of PRSs could be employed as discussed in [128]. This can create two cavities where the modes can couple as studied in [?] increasing the possible frequency range of the structure. Depending on the desired feed system requirements, it is also possible to obtain a similar uniform field distribution but for a wider aperture by means of introducing some asymmetry in the feed. This can allow for the leakage rate to be tailored as desired without affecting the pointing angle. Such a tapered leaky-wave distribution could allow for uniform feeding in larger arrays while maintaining the desired parallel-plate propagation at broadside which is perpendicular to the leaky via wall. Future work can include the use of this tapered leakage when considering slot array feeding.

The proposed parallel-plate waveguide launcher could lead to other kinds of SIW launchers, such as the surface-wave launcher when considering transverse magnetic (TM_0) surface-wave propagation on grounded dielectric slabs and for end-fire radiation, new planar antennas, or to other wave guiding structures and other new transition circuits. Moreover, when used as an end-fire antenna, it could increase size of the aperture, and with proper design, can possibly reduce the back-lobe radiation and improve the directivity of the forward pattern.

- Fabry-Perot cavity

The following step is the implementation of this leaky-wave antenna with the array of 2x2 sources to validate the 2D scanning in the azimuth and elevation planes. Once, this performance is demonstrated, this could be the base for many future 2D scanning leaky-wave antennas based on PRS or Fabry-Perot cavity for advance radar or medical imaging applications.

Alternatively, the "bull's-eye" antenna aperture can also be redesigned to optimize the directivity and gain towards end-fire by means of increased control of the attenuation constant for the dominantly excited leaky-wave mode.

- Smart Cable

The main improvement that could be obtained for the smart cable would be the validation of the estimated power levels in a corridor of similar dimensions, which are based on the individual radiating node performances. Also, improved antenna design for optimum radiation and better printed circuit board (PCB) materials; i.e., lower loss, could significantly increase the received power levels. Also, the smart cable can lead to more advanced power distribution systems that can also be applied in other scenarios rather than airplanes or subways.

Future design work could also include a more compact radiating node circuit and a higher quality substrate for the antenna, in order to improve antenna gain. Furthermore, the radiating nodes proposed in this thesis are based on LP antennas, and thus some modifications to the patches or the feeding network are required if circular polarization (CP) is needed by a final costumer. Moreover, the coupler and the patch layouts can be substituted by a coupled-gap feed configuration or by a proximity coupled fed patch. However, this would entail a more intricate design for the patch and coupling feed system, versus, a simpler and planar power-controlled coupler and radiating node implementation, as chosen in this work.

References

[1] M. Skolnik, *Radar Handbook, Third Edition.* McGraw-Hill Education, 2008.

[2] G. Stimson, *Introduction to Airborne Radar*, ser. Aerospace & Radar Systems. SciTech Pub., 1998.

[3] D. R. Jackson and A. Oliner, "Leaky-wave antennas," in *Modern Antenna Handbook*, C. Balanis, Ed. Wiley, 2011, ch. 7, pp. 328–332.

[4] J. Hirokawa, M. Ando, and N. Goto, "Waveguide-fed parallel plate slot array antenna," *IEEE Trans. Antennas Propag.*, vol. 40, no. 2, pp. 218–223, Feb. 1992.

[5] J. Hirokawa and M. Ando, "Single-layer feed waveguide consisting of posts for plane TEM wave excitation in parallel plates," *IEEE Trans. Antennas Propag.*, vol. 46, no. 5, pp. 625–630, May 1998.

[6] M. Ettorre, A. Neto, G. Gerini, and S. Maci, "Leaky-wave slot array antenna fed by a dual reflector system," *IEEE Transactions on Antennas and Propagation*, vol. 56, no. 10, pp. 3143–3149, Oct 2008.

[7] J. Hirokawa and M. Ando, "Efficiency of 76-GHz post-wall waveguide-fed parallel-plate slot arrays," *IEEE Trans. Antennas Propag.*, vol. 48, no. 11, pp. 1742–1745, Nov. 2000.

[8] J. H. Wang and K. K. Mei, "Theory and analysis of leaky coaxial cables with periodic slots," *IEEE Transactions on Antennas and Propagation*, vol. 49, no. 12, pp. 1723–1732, 2001.

[9] *Data Sheet: GORE Leaky Feeder Antennas*, GORE, 01 2013, rev. A.

[10] MATLAB, The MathWorks Inc., Natick, Massachusetts.

[11] Mathematica, Wolfram Research, Inc., champaign, IL, 2017.

[12] CST Microwave Studio [Online]. Available: https://www.cst.com.

[13] W. W. Hansen, "Radiating electromagnetic wave guide," Jun. 25 1946, US Patent 2,402,622.

[14] J. Hines and J. Upson, "A wide aperture tapered-depth scanning antenna," *Ohio State Univ. Res. Found*, pp. 667–7, 1957.

[15] C. Caloz, T. Itoh, and A. Rennings, "CRLH metamaterial leaky-wave and resonant antennas," *IEEE Antennas and Propagation Magazine*, vol. 50, no. 5, pp. 25–39, Oct 2008.

[16] H. Yang and N. Alexopoulos, "Gain enhancement methods for printed circuit antennas through multiple superstrates," *IEEE Transactions on Antennas and Propagation*, vol. 35, no. 7, pp. 860–863, July 1987.

[17] D. R. Jackson, P. Burghignoli, G. Lovat, and F. Capolino, "The role of leaky waves in fabry-perot resonant cavity antennas," in *2014 IEEE-APS Topical Conference on Antennas and Propagation in Wireless Communications (APWC)*, Aug 2014, pp. 786–789.

[18] W. Rotman and N. Karas, "The sandwich wire antenna: A new type of microwave line source radiator," in *1958 IRE International Convention Record*, vol. 5. IEEE, 1966, pp. 166–172.

[19] S. F. Mahmoud, S. K. Podilchak, Y. M. M. Antar, and A. P. Freundorfer, "Perturbation analysis of a planar periodic leaky-wave antenna fed by surface waves," *IEEE Antennas and Wireless Propagation Letters*, vol. 10, pp. 174–178, 2011.

[20] A. Hessel, "Generalized characteristics of traveling-wave antennas," *Antenna theory*, vol. 2, 1969.

[21] G. Floquet, "Sur les équations différentielles linéaires à coefficients périodiques," in *Annales scientifiques de l'École normale supérieure*, vol. 12, 1883, pp. 47–88.

[22] G. V. Trentini, "Partially reflecting sheet arrays," *IRE Transactions on Antennas and Propagation*, vol. 4, no. 4, pp. 666–671, 1956.

[23] N. Alexopoulos and D. Jackson, "Fundamental superstrate (cover) effects on printed circuit antennas," *IEEE Transactions on Antennas and Propagation*, vol. 32, no. 8, pp. 807–816, August 1984.

[24] S. Sengupta, D. R. Jackson, A. T. Almutawa, H. Kazemi, F. Capolino, and S. A. Long, "Radiation properties of a 2D periodic leaky-wave antenna," *IEEE Transactions on Antennas and Propagation*, pp. 1–1, 2019.

[25] T. Zhao, D. R. Jackson, J. T. Williams, H. Y. D. Yang, and A. A. Oliner, "2D periodic leaky-wave antennas part I: metal patch design," *IEEE Transactions on Antennas and Propagation*, vol. 53, no. 11, pp. 3505–3514, Nov 2005.

[26] C. Mateo-Segura, A. P. Feresidis, and G. Goussetis, "Bandwidth enhancement of 2D leaky-wave antennas with double-layer periodic surfaces," *IEEE Transactions on Antennas and Propagation*, vol. 62, no. 2, pp. 586–593, Feb 2014.

[27] P. Delogne, *Leaky feeders and subsurface radio communication*, ser. IEE electromagnetic waves series. Institution of Electrical Engineers, 1982.

[28] D. Cree and L. Giles, "Practical performance of radiating cables," *Radio and Electronic Engineer*, vol. 45, no. 5, pp. 215–223, 1975.

[29] P. Delogne and L. Deryck, "Underground use of a coaxial cable with leaky sections," *IEEE Transactions on Antennas and Propagation*, vol. 28, no. 6, pp. 875–883, 1980.

[30] H. Haag and K. Lehan, "Leaky coaxial cable systems for high speed trains in tunnels and other environmental conditions-theory and experience," in *Proc. 39th Int. Wire and Cable Symp*, 1990, pp. 71–79.

[31] H. Wang, F. R. Yu, and H. Jiang, "Modeling of radio channels with leaky coaxial cable for LTE-M based CBTC systems," *IEEE Communications Letters*, vol. 20, no. 5, pp. 1038–1041, May 2016.

[32] H. Wang, F. R. Yu, L. Zhu, T. Tang, and B. Ning, "Modeling of communication-based train control (CBTC) radio channel with leaky waveguide," *IEEE Antennas and Wireless Propagation Letters*, vol. 12, pp. 1061–1064, 2013.

[33] W. L. Gore, "Leaky feeder antennas for airborne Wi-Fi," *Microwave Journal*, vol. 56, no. 10, pp. 158–158,160, Oct 2013.

[34] Y. P. Zhang, "Indoor radiated-mode leaky feeder propagation at 2.0 GHz," *IEEE Transactions on Vehicular Technology*, vol. 50, no. 2, pp. 536–545, Mar 2001.

[35] V. P. A. Santos, F. J. B. da Fonseca, L. J. de Matos, W. D. T. Meza, G. L. Siqueira, and L. A. R. Ramirez, "Indoor signal coverage of a leaky feeder cable," in *2013 SBMO/IEEE MTT-S International Microwave Optoelectronics Conference (IMOC)*, Aug 2013, pp. 1–5.

[36] R. Harman and J. E. Siedlarz, "Advancements in leaky cable technology for intrusion detection," in *Proceedings of the 1982 Carnahan Conference on Security Technology*, 1982, pp. 115–121.

[37] P. Chen and G. Young, "Ported coax intrusion detection sensor," *IEEE Transactions on Antennas and Propagation*, vol. 32, no. 12, pp. 1313–1317, December 1984.

[38] K. Inomata, T. Hirai, K. Sumi, and K. Tanaka, "Wide-area surveillance sensor with leaky coaxial cables," in *2006 SICE-ICASE International Joint Conference*, Oct 2006, pp. 959–963.

[39] T. Zhao, D. R. Jackson, and J. T. Williams, "Radiation characteristics of a 2D periodic slot leaky-wave antenna," in *IEEE Antennas and Propagation Society International Symposium*, vol. 1, June 2002, pp. 482–485 vol.1.

[40] ——, "2-D periodic leaky-wave antennas-part II: slot design," *IEEE Transactions on Antennas and Propagation*, vol. 53, no. 11, pp. 3515–3524, Nov 2005.

[41] C. Mateo-Segura, M. Garcia-Vigueras, G. Goussetis, A. P. Feresidis, and J. L. Gomez-Tornero, "A simple technique for the dispersion analysis of fabry-perot cavity leaky-wave antennas," *IEEE Transactions on Antennas and Propagation*, vol. 60, no. 2, pp. 803–810, Feb 2012.

[42] G. Lovat, P. Burghignoli, F. Capolino, D. R. Jackson, and D. R. Wilton, "High-gain omnidirectional radiation patterns from a metal strip grating

leaky-wave antenna," in *2007 IEEE Antennas and Propagation Society International Symposium*, June 2007, pp. 5797–5800.

[43] D. Comite, V. Gómez-Guillamón Buendía, S. K. Podilchak, D. D. Ruscio, P. Baccarelli, P. Burghignoli, and A. Galli, "Planar antenna design for omnidirectional conical radiation through cylindrical leaky waves," *IEEE Antennas and Wireless Propagation Letters*, vol. 17, no. 10, pp. 1837–1841, Oct 2018.

[44] S. K. Podilchak, P. Baccarelli, P. Burghignoli, A. P. Freundorfer, and Y. M. M. Antar, "Analysis and design of annular microstrip-based planar periodic leaky-wave antennas," *IEEE Transactions on Antennas and Propagation*, vol. 62, no. 6, pp. 2978–2991, June 2014.

[45] D. Comite, V. Gómez-Guillamón Buendía, P. Burghignoli, P. Baccarelli, S. K. Podilchak, and A. Galli, "Array-fed Fabry-Perot cavity antenna for two-dimensional beam steering," in *2018 IEEE International Symposium on Antennas and Propagation USNC/URSI National Radio Science Meeting*, July 2018, pp. 1873–1874.

[46] T. Zhao, D. R. Jackson, J. T. Williams, H. D. Yang, and A. A. Oliner, "2-D periodic leaky-wave antennas-part I: metal patch design," *IEEE Transactions on Antennas and Propagation*, vol. 53, no. 11, pp. 3505–3514, Nov 2005.

[47] M. Wollitzer, J. Buechler, J. . Luy, U. Siart, E. Schmidhammer, J. Detlefsen, and M. Esslinger, "Multifunctional radar sensor for automotive application," *IEEE Transactions on Microwave Theory and Techniques*, vol. 46, no. 5, pp. 701–708, May 1998.

[48] M. Geiger and C. Waldschmidt, "160-ghz radar proximity sensor with distributed and flexible antennas for collaborative robots," *IEEE Access*, vol. 7, pp. 14 977–14 984, 2019.

[49] F. K. Schwering and S. Peng, "Design of dielectric grating antennas for millimeter-wave applications," *IEEE Transactions on Microwave Theory and Techniques*, vol. 31, no. 2, pp. 199–209, Feb 1983.

[50] M. Guglielmi and A. A. Oliner, "A practical theory for dielectric image guide leaky-wave antennas loaded by periodic metal strips," in *1987 17th European Microwave Conference*, Sep. 1987, pp. 549–554.

[51] C. Kim, M. Li, and K. Chang, "Image-guide leaky-wave antenna with wide beam-scan angle," in *2009 IEEE Antennas and Propagation Society International Symposium*, June 2009, pp. 1–4.

[52] J. L. Gomez-Tornero, J. Pascual-Garcia, and A. Alvarez-Melcon, "A novel leaky-wave antenna combining an image NRD guide and a strip circuit," *IEEE Antennas and Wireless Propagation Letters*, vol. 4, pp. 289–292, 2005.

[53] M. T. Lee, K. M. Luk, S. J. Xu, and E. K. N. Yung, "A double-slab leaky-wave NRD antenna," *IEEE Transactions on Antennas and Propagation*, vol. 52, no. 9, pp. 2488–2491, Sep. 2004.

[54] F. Xu and K. Wu, "Guided-wave and leakage characteristics of substrate integrated waveguide," *IEEE Trans. Microw. Theory Techn.*, vol. 53, no. 1, pp. 66–73, Jan. 2005.

[55] D. Deslandes, "Design equations for tapered microstrip-to-substrate integrated waveguide transitions," in *2010 IEEE MTT-S International Microwave Symposium*, May 2010, pp. 1–1.

[56] D. Deslandes and H. Wu, "Substrate integrated waveguide leaky-wave antenna: Concept and design considerations," in *Proc. Asia-Pacific Microwave Conf.*, vol. 1, Dec. 2005.

[57] A. J. Martínez-Ros, J. L. Gómez-Tornero, and G. Goussetis, "Planar leaky-wave antenna with flexible control of the complex propagation constant," *IEEE Trans. Antennas Propag.*, vol. 60, no. 3, pp. 1625–1630, Mar. 2012.

[58] J. L. Gomez-Tornero, G. Goussetis, A. P. Feresidis, and A. A. Melcon, "Control of leaky-mode propagation and radiation properties in hybrid dielectric-waveguide printed-circuit technology: Experimental results," *IEEE Transactions on Antennas and Propagation*, vol. 54, no. 11, pp. 3383–3390, Nov 2006.

[59] P. Baccarelli, S. Paulotto, D. R. Jackson, and A. A. Oliner, "A new brillouin dispersion diagram for 1D periodic printed structures," *IEEE Transactions on Microwave Theory and Techniques*, vol. 55, no. 7, pp. 1484–1495, July 2007.

[60] S. K. Podilchak, "Planar leaky-wave antennas and microwave circuits by practical surface wave launching," Ph.D. dissertation, 2013.

[61] R. Henry and M. Okoniewski, "A broadside-scanning half-mode substrate integrated waveguide periodic leaky-wave antenna," *IEEE Antennas and Wireless Propagation Letters*, vol. 13, pp. 1429–1432, 2014.

[62] A. J. Martínez-Ros, J. L. Gómez-Tornero, and F. Quesada-Pereira, "Efficient analysis and design of novel SIW leaky-wave antenna," *IEEE Antennas Wireless Propag. Lett.*, vol. 12, pp. 496–499, 2013.

[63] A. Patrovsky and K. Wu, "Substrate integrated image guide (SIIG)-a planar dielectric waveguide technology for millimeter-wave applications," *IEEE Transactions on Microwave Theory and Techniques*, vol. 54, no. 6, pp. 2872–2879, June 2006.

[64] M. T. Mu and Y. J. Cheng, "Low-sidelobe-level short leaky-wave antenna based on single-layer PCB-based substrate-integrated image guide," *IEEE Antennas and Wireless Propagation Letters*, vol. 17, no. 8, pp. 1519–1523, Aug 2018.

[65] Y. J. Cheng, Y. X. Guo, X. Y. Bao, and K. B. Ng, "Millimeter-wave low temperature co-fired ceramic leaky-wave antenna and array based on the substrate integrated image guide technology," *IEEE Transactions on Antennas and Propagation*, vol. 62, no. 2, pp. 669–676, Feb 2014.

[66] A. Patrovsky and K. Wu, "Substrate integrated image guide array antenna for the upper millimeter-wave spectrum," *IEEE Transactions on Antennas and Propagation*, vol. 55, no. 11, pp. 2994–3001, Nov 2007.

[67] M. Poveda-García, J. Oliva-Sánchez, R. Sanchez-Iborra, D. Cañete-Rebenaque, and J. L. Gomez-Tornero, "Dynamic wireless power transfer for cost-effective wireless sensor networks using frequency-scanned beaming," *IEEE Access*, vol. 7, pp. 8081–8094, 2019.

[68] S. A. Shah, N. Zhao, A. Ren, Z. Zhang, X. Yang, J. Yang, and W. Zhao, "Posture recognition to prevent bedsores for multiple patients using leaking coaxial cable," *IEEE Access*, vol. 4, pp. 8065–8072, 2016.

[69] P. Kopyt, T. Lavaud, B. Baldini, P. Wegrzyniak, and W. K. Gwarek, "Remotely powered wireless dual-band sensing system for aircraft EMC environment," *IEEE Tran. on EMC*, vol. 50, no. 3, pp. 491–498, Aug 2008.

[70] O. E. Gómez, "Fly-by-wireless: Benefits, risks and technical challenges," in *Fly by Wireless Workshop (FBW), 2010 Caneus*, Aug 2010, pp. 14–15.

[71] A. A. M. Saleh, A. Rustako, and R. Roman, "Distributed antennas for indoor radio communications," *IEEE Transactions on Communications*, vol. 35, no. 12, pp. 1245–1251, December 1987.

[72] H. Zhu, "Performance comparison between distributed antenna and microcellular systems," *IEEE Journal on Selected Areas in Communications*, vol. 29, no. 6, pp. 1151–1163, June 2011.

[73] V. Nikolopoulos, M. Fiacco, S. Stavrou, and S. R. Saunders, "Narrowband fading analysis of indoor distributed antenna systems," *IEEE Antennas and Wireless Propagation Letters*, vol. 2, no. 1, pp. 89–92, 2003.

[74] S. R. Lee, S. H. Moon, J. S. Kim, and I. Lee, "Capacity analysis of distributed antenna systems in a composite fading channel," *IEEE Transactions on Wireless Communications*, vol. 11, no. 3, pp. 1076–1086, March 2012.

[75] E. Park, S. R. Lee, and I. Lee, "Antenna placement optimization for distributed antenna systems," *IEEE Transactions on Wireless Communications*, vol. 11, no. 7, pp. 2468–2477, July 2012.

[76] X. Wang, P. Zhu, and M. Chen, "Antenna location design for generalized distributed antenna systems," *IEEE Communications Letters*, vol. 13, no. 5, pp. 315–317, May 2009.

[77] J. Wang, H. Zhu, and N. J. Gomes, "Distributed antenna systems for mobile communications in high speed trains," *IEEE Journal on Selected Areas in Communications*, vol. 30, no. 4, pp. 675–683, May 2012.

[78] B. Chow, M. L. Yee, M. Sauer, A. Ng'Oma, M. C. Tseng, and C. H. Yeh, "Radio-over-fiber distributed antenna system for WiMAX bullet train field trial," in *2009 IEEE Mobile WiMAX Symposium*, July 2009, pp. 98–101.

[79] R. J. Collier and G. X. Chang, "A broadband waveguide to image guide transition," in *1982 12th European Microwave Conference*, Sept 1982, pp. 526–533.

[80] H. Tehrani, M. Y. Li, and K. Chang, "Broadband microstrip to dielectric image line transitions," *IEEE Microwave and Guided Wave Letters*, vol. 10,

no. 10, pp. 409–411, Oct 2000.

[81] A. R. Perkons and T. Itoh, "Surface wave excitation of a dieletric slab by a Yagi-Uda slot array antenna," in *1996 26th European Microwave Conference*, vol. 2, Sept 1996, pp. 625–628.

[82] Y. Shih, J. Rivers, and T. Itoh, "Directive planar excitation of an image-guide," in *1981 IEEE MTT-S International Microwave Symposium Digest*, June 1981, pp. 5–7.

[83] Y. J. Cheng, X. Y. Bao, and Y. X. Guo, "LTCC-based substrate integrated image guide and its transition to conductor-backed coplanar waveguide," *IEEE Microwave and Wireless Components Letters*, vol. 23, no. 9, pp. 450–452, Sept 2013.

[84] S. K. Podilchak, A. P. Freundorfer, and Y. M. M. Antar, "Surface-wave launchers for beam steering and application to planar leaky-wave antennas," *IEEE Transactions on Antennas and Propagation*, vol. 57, no. 2, pp. 355–363, Feb 2009.

[85] V. Gómez-Guillamón Buendía, S. K. Podilchak, G. Goussetis, and J. Gómez-Tornero, "A TM$_0$ surface wave launcher by microstrip and substrate integrated waveguide technology," in *2017 11th European Conference on Antennas and Propagation (EUCAP)*, March 2017, pp. 3859–3862.

[86] M. Ettorre, S. Bruni, G. Gerini, A. Neto, N. Llombart, and S. Maci, "Sector PCS-EBG antenna for low-cost high-directivity applications," *IEEE Antennas and Wireless Propagation Letters*, vol. 6, pp. 537–539, 2007.

[87] D. Comite, S. K. Podilchak, P. Baccarelli, P. Burghignoli, A. Galli, A. P. Freundorfer, and Y. M. M. Antar, "A dual-layer planar leaky-wave antenna designed for linear scanning through broadside," *IEEE Antennas and Wireless Propagation Letters*, vol. 16, pp. 1106–1110, 2017.

[88] S. K. Podilchak, A. P. Freundorfer, and Y. M. M. Antar, "A new leaky-wave antenna design using simple surface-wave power routing techniques," in *2011 IEEE International Symposium on Antennas and Propagation (APSURSI)*, July 2011, pp. 3052–3054.

[89] ——, "Planar leaky-wave antenna designs offering conical-sector beam scanning and broadside radiation using surface-wave launchers," *IEEE Antennas and Wireless Propagation Letters*, vol. 7, pp. 155–158, 2008.

[90] A. Sutinjo, M. Okoniewski, and R. H. Johnston, "A holographic antenna approach for surface wave control in microstrip antenna applications," *IEEE Transactions on Antennas and Propagation*, vol. 58, no. 3, pp. 675–682, March 2010.

[91] C. Rusch, J. Schäfer, H. Gulan, P. Pahl, and T. Zwick, "Holographic mmW-antennas with TE_0 and TM_0 surface wave launchers for frequency-scanning FMCW-radars," *IEEE Transactions on Antennas and Propagation*, vol. 63, no. 4, pp. 1603–1613, April 2015.

[92] E. Gandini, M. Ettorre, R. Sauleau, and A. Neto, "Mutual coupling reduction of Fabry-Perot SIW feeds using a double partially reflecting pin-made grid configuration," *IEEE Antennas and Wireless Propagation Letters*, vol. 10, pp. 647–650, 2011.

[93] Sakakibara, Y. Kimura, A. Akiyama, J. Hirokawa, M. Ando, and N. Goto, "Alternating phase-fed waveguide slot arrays with a single-layer multiple-way power divider," *IEE Proc. Microwaves, Antennas Propag.*, vol. 144, no. 6, pp. 425–430, Dec. 1997.

[94] D. Parker and D. C. Zimmermann, "Phased arrays - part 1: theory and architectures," *IEEE Transactions on Microwave Theory and Techniques*, vol. 50, no. 3, pp. 678–687, March 2002.

[95] M. Iskander, W. Kim, J. Bell, N. Celik, and Z. Yun, "Antenna array technologies for advanced wireless systems," in *Modern Antenna Handbook*, C. Balanis, Ed. Wiley, 2011, ch. 25, pp. 1255–1325.

[96] S. Qi, W. Wu, D. Fang, and Z. Shen, "Circular aperture antenna with conical beam," *IEEE Antennas and Wireless Propagation Letters*, vol. 10, pp. 211–214, 2011.

[97] B. Q. Wu and K. Luk, "A wideband, low-profile, conical-beam antenna with horizontal polarization for indoor wireless communications," *IEEE Antennas and Wireless Propagation Letters*, vol. 8, pp. 634–636, 2009.

[98] W. Lin, H. Wong, and R. W. Ziolkowski, "Wideband pattern-reconfigurable antenna with switchable broadside and conical beams," *IEEE Antennas and Wireless Propagation Letters*, vol. 16, pp. 2638–2641, 2017.

[99] J. Row and T. Lin, "Frequency-reconfigurable coplanar patch antenna with conical radiation," *IEEE Antennas and Wireless Propagation Letters*, vol. 9, pp. 1088–1091, 2010.

[100] F. J. Zucker, "The guiding and radiation of surface waves," in *Proc. Symp. on Modern Advances in Microwave Techniques*, vol. 4, 1954, pp. 403–435.

[101] F. Zucker and R. Johnson, "Surface-wave antennas," in *Antenna Engineering Handbook*, J. Volakis, Ed. McGraw–Hill New York, 2007, ch. 10, pp. 1–32.

[102] D. Pozar, *Microwave Engineering, 4th Edition.* Wiley, 2011.

[103] C. M. Angulo, "Discontinuities in a rectangular waveguide partially filled with dielectric," *IRE Transactions on Microwave Theory and Techniques*, vol. 5, no. 1, pp. 68–74, January 1957.

[104] C. Angulo, "Diffraction of surface waves by a semi-infinite dielectric slab," *IRE Transactions on Antennas and Propagation*, vol. 5, no. 1, pp. 100–109, January 1957.

[105] C. Angulo and W. Chang, "The launching of surface waves by a parallel plate waveguide," *IRE Transactions on Antennas and Propagation*, vol. 7, no. 4, pp. 359–368, October 1959.

[106] A. Cullen, "The excitation of plane surface waves," *Proceedings of the IEE-Part IV: Institution Monographs*, vol. 101, no. 7, pp. 225–234, 1954.

[107] A. Ip and D. R. Jackson, "Radiation from cylindrical leaky waves," *IEEE Transactions on Antennas and Propagation*, vol. 38, no. 4, pp. 482–488, April 1990.

[108] D. R. Jackson and A. A. Oliner, "A leaky-wave analysis of the high-gain printed antenna configuration," *IEEE Transactions on Antennas and Propagation*, vol. 36, no. 7, pp. 905–910, July 1988.

[109] A. Oliner, "Leaky-wave antennas," in *Antenna Engineering Handbook*, R. Johnson, Ed. McGraw–Hill, 1993, ch. 10, pp. 1–54.

[110] F. Mesa and D. R. Jackson, *Leaky Modes and High-Frequency Effects in Microwave Integrated Circuits.* American Cancer Society, 2005.

[111] T. Tamir and A. A. Oliner, "Guided complex waves. Part 2: Relation to radiation patterns," *Proceedings of the Institution of Electrical Engineers*, vol. 110, no. 2, pp. 325–334, February 1963.

[112] ——, "Guided complex waves. Part 1: Fields at an interface," *Proceedings of the Institution of Electrical Engineers*, vol. 110, no. 2, pp. 310–324, February 1963.

[113] P. Burghignoli, G. Lovat, and D. R. Jackson, "Analysis and optimization of leaky-wave radiation at broadside from a class of 1D periodic structures," *IEEE Trans. Antennas Propag.*, vol. 54, no. 9, pp. 2593–2604, Sep. 2006.

[114] J. F. Kiang, "Radiation properties of circumferential slots on a coaxial cable," *IEEE transactions on microwave theory and techniques*, vol. 45, no. 1, pp. 102–107, 1997.

[115] D. Martin, "A general study of the leaky-feeder principle," *Radio and Electronic Engineer*, vol. 45, no. 5, pp. 205–214, 1975.

[116] P. P. Delogne and M. Safak, "Electromagnetic theory of the leaky coaxial cable," *Radio and Electronic Engineer*, vol. 45, no. 5, pp. 233–240, May 1975.

[117] V. Gómez-Guillamón Buendía and S. K. Podilchak, "Simple surface-wave launching by parallel-plate and microstrip feeding for leaky-wave antennas and other planar guided-wave applications," in *12th European Conference on Antennas and Propagation (EuCAP 2018)*, April 2018, pp. 1–4.

[118] O. Luukkonen, C. Simovski, G. Granet, G. Goussetis, D. Lioubtchenko, A. V. Raisanen, and S. A. Tretyakov, "Simple and accurate analytical model of planar grids and high-impedance surfaces comprising metal strips or patches," *IEEE Transactions on Antennas and Propagation*, vol. 56, no. 6, pp. 1624–1632, June 2008.

[119] S. Koul, *Millimeter Wave Optical Dielectric Integrated Guides and Circuits.* Wiley, 1997.

[120] S. K. Podilchak, G. Labate, and L. Matekovits, "Controlling surface waves by introducing anisotropy into the conductive backing of planar dielectric slabs," in *2015 International Conference on Electromagnetics in Advanced Applications (ICEAA)*, Sep. 2015, pp. 1427–1428.

[121] A. Hessel and A. Oliner, ""mode-coupling" regions in the dispersion curves of modulated slow wave antennas," in *1963 Antennas and Propagation Society International Symposium*, vol. 1, July 1963, pp. 104–108.

[122] A. Patrovsky and K. Wu, "94-GHz broadband transition from coplanar waveguide to substrate integrated image guide (SIIG)," in *2007 IEEE/MTT-S International Microwave Symposium*, June 2007, pp. 1551–1554.

[123] ——, "94-GHz planar dielectric rod antenna with substrate integrated image guide (SIIG) feeding," *IEEE Antennas and Wireless Propagation Letters*, vol. 5, pp. 435–437, 2006.

[124] J. C. Rautio, "A de-embedding algorithm for electromagnetics," *International Journal of Microwave and Millimeter-Wave Computer-Aided Engineering*, vol. 1, no. 3, pp. 282–287, 1991.

[125] C. S. Prasad and A. Biswas, "Planar excitation of dielectric waveguide antenna for broadband and high-gain application," *IEEE Antennas and Wireless Propagation Letters*, vol. 16, pp. 1209–1212, 2017.

[126] H. Wang, D. G. Fang, B. Zhang, and W. Q. Che, "Dielectric loaded substrate integrated waveguide (SIW) H-plane horn antennas," *IEEE Transactions on Antennas and Propagation*, vol. 58, no. 3, pp. 640–647, March 2010.

[127] H. Boutayeb, T. A. Denidni, K. Mahdjoubi, A. C. Tarot, A. R. Sebak, and L. Talbi, "Analysis and design of a cylindrical EBG-based directive antenna," *IEEE Transactions on Antennas and Propagation*, vol. 54, no. 1, pp. 211–219, Jan 2006.

[128] V. Gómez-Guillamón Buendía, S. K. Podilchak, D. Comite, P. Baccarelli, P. Burghignoli, J. L. Gómez Tornero, and G. Goussetis, "Compact leaky SIW feeder offering TEM parallel plate waveguide launching," *IEEE Access*, vol. 7, pp. 13 373–13 382, 2019.

[129] A. P. Feresidis and J. C. Vardaxoglou, "High gain planar antenna using optimised partially reflective surfaces," *IEE Proceedings - Microwaves, Antennas and Propagation*, vol. 148, no. 6, pp. 345–350, Dec 2001.

[130] D. Deslandes and K. Wu, "Design consideration and performance analysis of substrate integrated waveguide components," in *2002 32nd European Microwave Conference*, Sept 2002, pp. 1–4.

[131] J. L. Gómez-Tornero, A. Martínez Ros, M. A. Martínez, A. Martínez Sala, G. Goussetis, and S. K. Podilchak, "A simple parallel-plate wave launcher in substrate integrated waveguide technology," in *Proc. IEEE Symp. Antennas Propag. USNC/URSI Nat. Radio Sci. Meeting*, Jul. 2015, pp. 480–481.

[132] S. Germain, D. Deslandes, and K. Wu, "Development of substrate integrated waveguide power dividers," in *Proc. Can. Conf. Electrical Computer Eng.*, vol. 3, May 2003, pp. 1921–1924 vol.3.

[133] A. R. Akbarzadeh and Z. Shen, "Waveguide power dividers using multiple posts," *Microw. Opt. Tech. Lett.*, vol. 50, no. 4, pp. 981–984, 2008.

[134] J. Hirokawa, K. Sakurai, M. Ando, and N. Goto, "An analysis of a waveguide T junction with an inductive post," *IEEE Trans. Microw. Theory Tech.*, vol. 39, no. 3, pp. 563–566, Mar. 1991.

[135] J. Volakis, *Antenna Engineering Handbook, Fourth Edition*. McGraw-Hill Companies,Incorporated, 2007.

[136] N. Marcuvitz, *Waveguide Handbook*. New York, NY: McGraw-Hill, 1951.

[137] G. Valerio, S. Paulotto, P. Baccarelli, P. Burghignoli, and A. Galli, "Accurate bloch analysis of 1-D periodic lines through the simulation of truncated structures," *IEEE Transactions on Antennas and Propagation*, vol. 59, no. 6, pp. 2188–2195, June 2011.

[138] N. Apaydin, L. Zhang, K. Sertel, and J. L. Volakis, "Experimental validation of frozen modes guided on printed coupled transmission lines," *IEEE Transactions on Microwave Theory and Techniques*, vol. 60, no. 6, pp. 1513–1519, June 2012.

[139] D. Deslandes and K. Wu, "Integrated microstrip and rectangular waveguide in planar form," *IEEE Microw. Wireless Compon. Lett.*, vol. 11, no. 2, pp. 68–70, Feb. 2001.

[140] E. Miralles, H. Esteban, C. Bachiller, A. Belenguer, and V. E. Boria, "Improvement for the design equations for tapered microstrip-to-substrate integrated waveguide transitions," in *2011 International Conference on Electromagnetics in Advanced Applications*, Sept 2011, pp. 652–655.

[141] N. Ghassemi, I. Boudreau, D. Deslandes, and K. Wu, "Millimeter-wave broadband transition of substrate integrated waveguide on high-to-low dielectric constant substrates," *IEEE Transactions on Components, Packaging and Manufacturing Technology*, vol. 3, no. 10, pp. 1764–1770, Oct 2013.

[142] Z. Kordiboroujeni and J. Bornemann, "New wideband transition from microstrip line to substrate integrated waveguide," *IEEE Transactions on Microwave Theory and Techniques*, vol. 62, no. 12, pp. 2983–2989, Dec 2014.

[143] Y. Ding and K. Wu, "Substrate integrated waveguide-to-microstrip transition in multilayer substrate," *IEEE Transactions on Microwave Theory and Techniques*, vol. 55, no. 12, pp. 2839–2844, Dec 2007.

[144] E. D. Caballero, A. B. Martínez, H. E. Gonzalez, O. M. Belda, and V. B. Esbert, "A novel transition from microstrip to a substrate integrated waveguide with higher characteristic impedance," in *2013 IEEE MTT-S International Microwave Symposium Digest (MTT)*, June 2013, pp. 1–4.

[145] C. Balanis, *Antenna Theory: Analysis and Design.* Wiley, 2012.

[146] S. K. Podilchak, A. P. Freundrofer, and Y. M. M. Antar, "Planar antenna for directive beam steering at end-fire using an array of surface-wave launchers," *Electronics Letters*, vol. 45, no. 9, pp. 444–445, April 2009.

[147] S. K. Podilchak, A. P. Freundorfer, and Y. M. M. Antar, "Planar antennas for far-field beam steering at end-fire using directive surface-wave launchers," in *2009 13th International Symposium on Antenna Technology and Applied Electromagnetics and the Canadian Radio Science Meeting*, Feb 2009, pp. 1–4.

[148] C. H. Walter, *Traveling wave antennas.* Dover Publications, 1970.

[149] C. Mateo-Segura, A. P. Feresidis, and G. Goussetis, "Bandwidth enhancement of 2-D leaky-wave antennas with double-layer periodic surfaces," *IEEE Trans. Antennas Propag.*, vol. 62, no. 2, pp. 586–593, Feb 2014.

[150] D. Comite, P. Burghignoli, P. Baccarelli, and A. Galli, "Two-dimensional beam scanning with cylindrical-leaky-wave-enhanced phased arrays," *IEEE Transactions on Antennas and Propagation*, pp. 1–1, 2019.

[151] D. Comite, W. Fuscaldo, S. K. Podilchak, P. D. Hilario Re, V. Gómez-Guillamón Buendía, P. Burghignoli, P. Baccarelli, and A. Galli, "Radially periodic leaky-wave antenna for bessel beam generation over a wide-frequency range," *IEEE Transactions on Antennas and Propagation*, vol. 66, no. 6, pp. 2828–2843, June 2018.

[152] S. K. Podilchak, P. Baccarelli, P. Burghignoli, A. P. Freundorfer, and Y. M. M. Antar, "Optimization of a planar "bull-eye" leaky-wave antenna fed by a printed surface-wave source," *IEEE Antennas and Wireless Propagation Letters*, vol. 12, pp. 665–669, 2013.

[153] A. Galli, P. Baccarelli, and P. Burghignoli, *Leaky-Wave Antennas.* John Wiley and Sons, Inc., 1999.

[154] D. Di Ruscio, P. Burghignoli, P. Baccarelli, D. Comite, and A. Galli, "Spectral method of moments for planar structures with azimuthal symmetry," *IEEE Transactions on Antennas and Propagation*, vol. 62, no. 4, pp. 2317–2322, April 2014.

[155] "IEEE standard test procedures for antennas," *ANSI/IEEE Std 149-1979*, 1979.

[156] J. L. Gómez-Tornero, D. Blanco, E. Rajo-Iglesias, and N. Llombart, "Holographic surface leaky-wave lenses with circularly-polarized focused Near-Fields Part I: Concept, design and analysis theory," *IEEE Transactions on Antennas and Propagation*, vol. 61, no. 7, pp. 3475–3485, July 2013.

[157] J. Durnin, "Exact solutions for nondiffracting beams. I. The scalar theory," *J. Opt. Soc. Am. A*, vol. 4, no. 4, pp. 651–654, Apr 1987.

[158] E. Recami, M. Zamboni-Rached, and L. A. Ambrosio, *Non-Diffracting Waves: An Introduction.* John Wiley & Sons, Ltd, 2013, ch. 1, pp. 1–67.

[159] M. Ettorre, S. C. Pavone, M. Casaletti, and M. Albani, "Experimental validation of Bessel beam generation using an inward Hankel aperture distribution," *IEEE Transactions on Antennas and Propagation*, vol. 63, no. 6, pp. 2539–2544, June 2015.

[160] S. C. Pavone, M. Ettorre, and M. Albani, "Analysis and design of Bessel beam launchers: Longitudinal polarization," *IEEE Transactions on Antennas and Propagation*, vol. 64, no. 6, pp. 2311–2318, June 2016.

[161] M. Q. Qi, W. X. Tang, and T. J. Cui, "A broadband Bessel beam launcher using metamaterial lens," *Scientific reports*, vol. 5, p. 11732, 2015.

[162] Y. C. Zhong and Y. J. Cheng, "Wideband quasi-nondiffraction beam with accurately controllable propagating angle and depth-of-field," *IEEE Transactions on Antennas and Propagation*, vol. 65, no. 10, pp. 5035–5042, 2017.

[163] B. G. Cai, Y. B. Li, W. X. Jiang, Q. Cheng, and T. J. Cui, "Generation of spatial Bessel beams using holographic metasurface," *Optics express*, vol. 23, no. 6, pp. 7593–7601, 2015.

[164] D. Comite, P. Baccarelli, P. Burghignoli, and A. Galli, "Omnidirectional 2-D leaky-wave antennas with reconfigurable polarization," *IEEE Antennas and Wireless Propagation Letters*, vol. 16, pp. 2354–2357, 2017.

[165] V. Gómez-Guillamón Buendía, S. K. Podilchak, G. Goussetis, D. Masotti, A. Costanzo, and P. Nicole, "A smart cable offering selective and distributed antenna radiation using RF switches and non-conventional hybrid couplers," *IEEE Transactions on Antennas and Propagation*, vol. 66, no. 11, pp. 6346–6351, Nov 2018.

[166] R. Chakraborty, S. Roy, and V. Jandhyala, "Revisiting RFID link budgets for technology scaling: Range maximization of RFID tags," *IEEE Transactions on Microwave Theory and Techniques*, vol. 59, no. 2, pp. 496–503, Feb 2011.

[167] Skyworks, "SKYA21001: 20 MHz to 3.0 GHz SPDT switch."

[168] V. Gómez-Guillamón Buendía, S. Kenny, S. K. Podilchak, G. Goussetis, A. Costanzo, and P. Nicole, "Smart cable for radio frequency identification in aeronautical applications," in *2016 10th European Conference on Antennas and Propagation (EuCAP)*, April 2016, pp. 1–3.

[169] Solwise, "RMC50-12-24LS LCX Cable: 2.4 GHz radiating coaxial antenna cable, low smoke, zero halogen."

[170] *Coaxial communication cables - Part 4: Sectional specification for radiating cables*, Std. IEC 61 196-4:2015, 2004.

[171] M. Kuznetcov, V. Gómez-Guillamón Buendía, Z. Shafiq, L. Matekovits, D. E. Anagnostou, and S. K. Podilchak, "Printed leaky-wave antenna with aperture control using width-modulated microstrip lines and TM surface-wave feeding by SIW technology," *IEEE Antennas and Wireless Propagation Letters*, 2019.